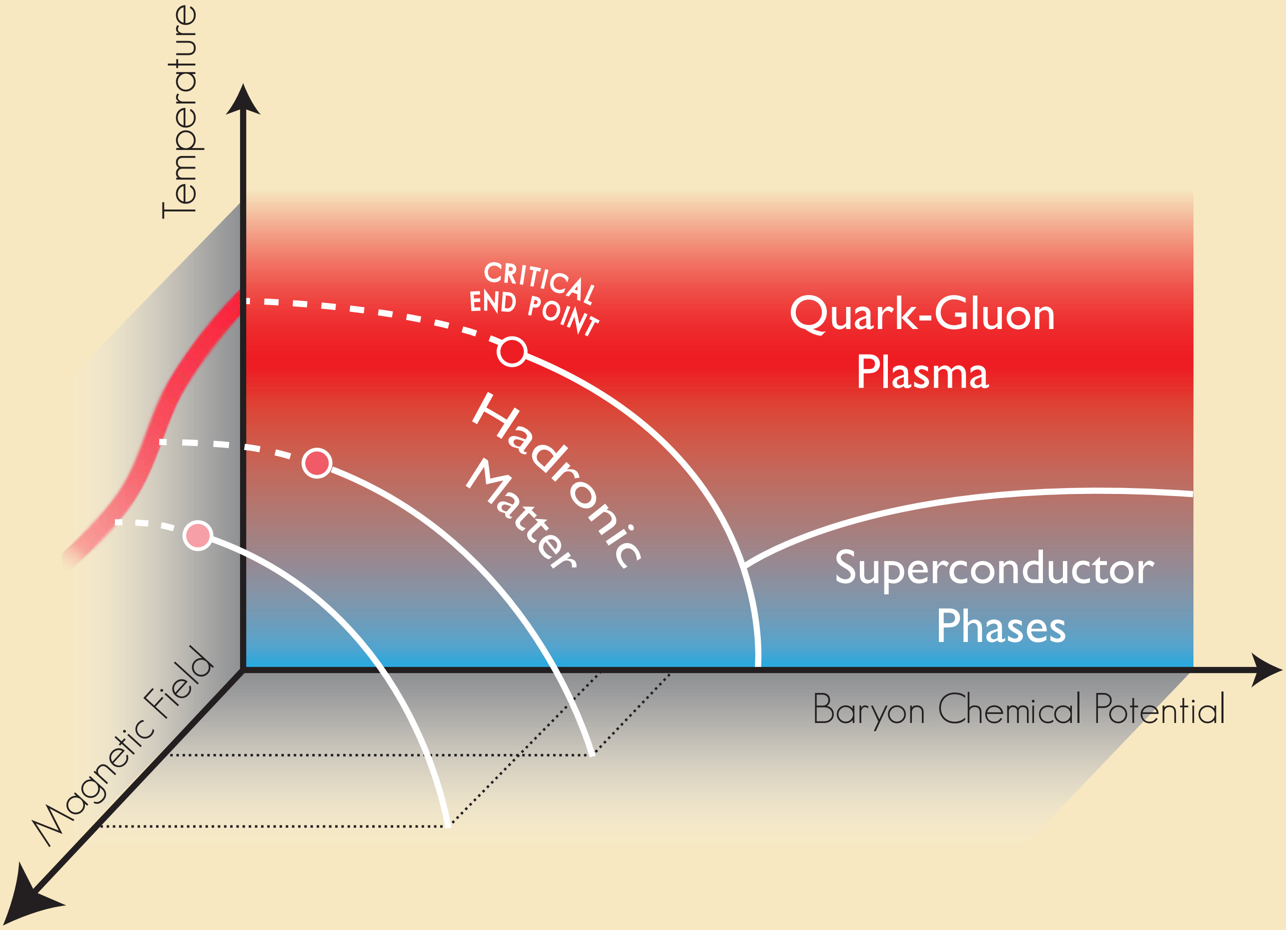

Márcio Rafael Baptista Ferreira

QCD PHASE DIAGRAM
UNDER AN EXTERNAL MAGNETIC FIELD

Tese de Doutoramento em Física, Ramo de Física Nuclear e das Partículas, orientada pela Prof. Dr^{a}. Constança Providência e pelo Dr. Pedro Costa e apresentada ao Departamento de Física da Faculdade de Ciências e Tecnologia da Universidade de Coimbra

Dezembro de 2015

· U C ·

Universidade de Coimbra

· U C ·

UNIVERSIDADE DE COIMBRA

QCD phase diagram under an external magnetic field

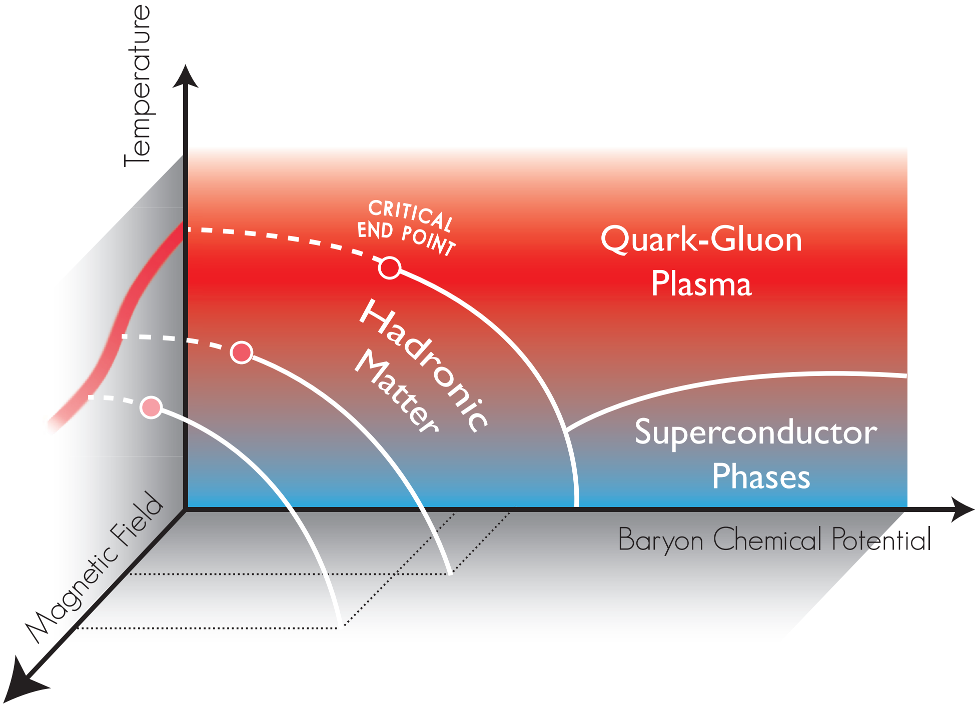

Supervisors: Prof. Dr. Constança Providência and Dr. Pedro Costa

Márcio Rafael Baptista Ferreira

Department of Physics
Faculty of Science and Technology
University of Coimbra

December 2015

This work was funded by the UE/FEDER, through Programa Operacional Factores de Competitividade - COMPETE and by National Funds through FCT - Fundação para a Ciência e Tecnologia, by Grant No. SFRH/BD/51717/2011.

Acknowledgements

First of all, I want to express my sincere gratitude to my advisors Prof. Dr. Constança Providência and Dr. Pedro Costa for their outstanding guidance and dedication. I am grateful for their support and encouragement throughout this thesis. I am truly indebted to Prof. Dr. Constança Providência for her support throughout my graduate studies.

I would like to thank Prof. Dr. Débora Menezes for the warm hospitality and guidance during my stay at the Federal University of Santa Catarina. I am also thankful for the opportunity to participate in several workshops and conferences in Brazil during my studies in Florianópolis.

I am grateful to Prof. Dr. Tobias Frederico and Prof. Dr. Manuel Malheiro for their hospitality and stimulating discussions during my stay in the Aeronautics Institute of Technology.

Last but not least, I wish to express my gratitude to my parents and friends for their affection and support.

Resumo

Neste trabalho é investigado o impacto de um campo magnético externo na estrutura do diagrama de fases da Cromodinâmica Quântica (QCD). O estudo é realizado utilizando o modelo efetivo de Nambu–Jona-Lasinio para três sabores acoplado ao *loop* de Polyakov (modelo de PNJL). A interação de *entanglement* (modelo de EPNJL) na presença de um campo magnético é também estudada. Ambas as transições quiral e de desconfinamento na presença de um campo magnético externo podem ser analisadas usando os modelos de PNJL e EPNJL. Para o modelo de EPNJL é verificado que a coincidência das temperaturas pseudocríticas de ambas as transições quiral e de deconfinamento dependem da parametrização da interação de *entanglement*.

É realizado um estudo sistemático do efeito de um campo magnético externo nas transições quiral e de desconfinamento a potencial químico bariónico nulo, e.g., calculando a dependência das temperaturas pseudocríticas com a intensidade do campo magnético. O impacto de um campo magnético externo no comportamento do quark estranho é analizado detalhadamente. É mostrado que a temperatura pseudocrítica associada à transição quiral do quark estranho é pouco sensível à presença de um campo magnético externo. Além disso, a sua grande massa corrente torna o quark estranho pouco sensível ao termo de 't Hooft, contrariamente à forte influência que tem nos quarks leves. Ambos os modelos de PNJL e EPNJL prevêem o efeito de Catálise Magnética a qualquer temperatura, mas não reproduzem o efeito de Catálise Magnética Inversa (CMI) em redor da temperatura pseudocrítica de transição, obtido em resultados recentes da LQCD.

Mostramos que é possível reproduzir a CMI se a intensidade da interação entre quarks diminuir com o campo magnético. Propomos dois mecanismos que reproduzem o efeito de CMI, que assumem o enfraquecimento da constante de acoplamento da interação escalar com o aumento da intensidade do campo magnético.

O diagrama de fases é calculado para vários cenários de isospin e estranhesa, com especial ênfase na localização do ponto crítico. Partindo do modelo que reproduz qualitativamente os resultados da LQCD a potencial químico bariónico nulo, introduzimos no modelo de PNJL um potencial químico bariónico μ_B finito e estudamos o impacto de um campo magnético externo na estrutura do diagrama de fases $T - \mu_B$ da QCD. Para uma intensidade de campo magnético superior a 0.3 GeV^2, é mostrado que, devido ao efeito da CMI, a temperatura do ponto crítico varia ligeiramente, enquanto o potencial químico bariónico se move para valores menores, tornando mais acessível a possível deteção experimental do ponto crítico.

Abstract

In this work the impact of an external magnetic field on the phase diagram structure of Quantum Chromodynamics (QCD) is investigated. The study is performed using the three-flavor Nambu–Jona-Lasinio (NJL) effective model coupled to the Polyakov loop (PNJL model). The entanglement interaction (EPNJL model) in a magnetic field presence is also studied. Both the chiral and deconfinement transitions under the presence of an external magnetic field can be analyzed within the PNJL and the EPNJL models. For the EPNJL model it is found that the coincidence of both chiral and deconfinement pseudocritical temperatures depends on the entanglement interaction parametrization.

We do a systematic study on the effect of an external magnetic field on the chiral and the deconfinement transitions at zero baryonic chemical potential, e.g., calculating the pseudocritical temperatures dependence on the magnetic field strength. The impact of the external magnetic field on the strange quark behavior is also deeply analyzed. It is shown that the strange pseudocritical transition temperature is less sensitive to the magnetic field than the light quarks, due to the larger strange quark current mass. Furthermore, its large current mass also makes the strange quark less sensitive to the 't Hooft term, as opposed to the strong influence it has on the light quarks. Both the PNJL and the EPNJL models predict the Magnetic Catalysis effect at any temperature, and thus do not reproduce the Inverse Magnetic Catalysis (IMC) effect near the pseudocritical transition temperature, as seen in recent LQCD results.

We show that the IMC is obtained if the interaction strength between quarks decreases with the magnetic field. We propose two mechanisms that reproduce the IMC effect, which assume a weakening of the scalar coupling with increasing magnetic field strength.

The phase diagram is calculated for several scenarios of isospin and strangeness, with special emphasis on the location of the Critical End Point (CEP). Starting from the model that reproduces qualitatively the LQCD results at zero baryonic chemical potential, we introduce in the PNJL model a finite baryonic chemical potential μ_B and study how the magnetic field affects the structure of the $T - \mu_B$ diagram of QCD. For a magnetic field strength above 0.3 GeV^2, it is shown that, due to the IMC effect, the CEP temperature almost does not change while the CEP baryonic chemical potential moves to smaller values, making a possible detection of the CEP in the laboratory more accessible.

Contents

Chapter 1

Introduction

1.1 Quantum Chromodynamics

Quantum ChromoDynamics (QCD) is presently the theory of strong interactions, a theoretical framework for understanding the dynamics of quarks and gluons. Two of the main striking features of QCD are the spontaneous breaking of chiral symmetry and confinement, both having a nonperturbative origin. The interaction among quarks gets weaker when their distance decreases, and this feature is known as asymptotic freedom [1]. Moreover, the interactions become stronger as the particle separation increases. A quantitative understanding of this mechanism, which is called confinement, is hard to obtain, even though we know the underlying theory. Due to the nonabelian nature of QCD, in addition to interaction between quarks and gluons, there are also gluon self-interaction terms and the QCD equations are hard to solve on a purely mathematical ground. Though we can use perturbation theory at short distances due to the asymptotic freedom property of QCD, the known way to solve QCD in the strong coupling regime, relevant to nuclear physics, is through numerical calculations of QCD on a discrete four-dimensional space-time Lattice (LQCD) (for a review of LQCD results see [2, 3]). Besides LQCD simulations, the Dyson-Schwinger formalism provides an alternative approach to study the QCD properties [4]. The QCD predictions in the strong coupling regime can be tested in high-energy scattering experiments [5, 6].

With the introduction of a finite baryon chemical potential in LQCD simulations, the quark determinant that appears in the QCD partition function is no longer real (*sign problem*), and standard Monte Carlo simulations are no longer possible. Although LQCD methods that probe low chemical potential exist (see [3], e.g.), other approaches such as effective models are a reliable way of getting an insight into the whole phase structure of QCD. When the phenomenon under study is characterized by a natural separation of energy scales, effective theories become a powerful framework. They are particularly important tools in QCD, where the relevant degrees of freedom are quarks and gluons at high energies and hadronic matter at low energies. Indeed, at energies below the nucleon mass, the most notable features of QCD are the confinement of quarks and the spontaneous breaking of chiral symmetry.

Critical behavior in QCD thermodynamics is generally related to the spontaneous breaking of a global symmetry [7]. The order parameter is the quantity that establishes the state of a symmetry: it vanishes when the system shares the symmetry of the Lagrangian, and it becomes non-zero when the symmetry is spontaneously broken.

The deconfinement in a gauge theory is related to the spontaneous breaking of the global center symmetry. The Polyakov loop constitutes an order parameter for the center symmetry: it is zero if the symmetry is realized (confined phase) and is non-zero when the symmetry is broken (deconfined phase). Deconfinement is basically the phase transition from colorless bound states to color unbound states, i.e., from hadrons to unbound quarks and gluons in QCD or from glueballs to unbound gluons in pure gauge theory. Therefore, due to the release of degrees of freedom, we expect a sharp transition from a confined hadronic phase to deconfined phase of non-interacting colored quarks and gluons. The presence of dynamical quarks in QCD explicitly breaks the center symmetry. Nevertheless, the Polyakov loop remains small up to a certain temperature and then increases rapidly in a very narrow temperature interval, which coincides with the rapid increase of the energy density, indicating a sudden change in the number of degrees of freedom from bound to unbound color matter. Thus, some of the critical behavior, present in the gauge theory, seems to persist even in the presence of dynamical quarks [7].

Chiral symmetry is a symmetry of the QCD Lagrangian for massless quarks. In the vacuum of QCD the chiral symmetry is spontaneously broken, which is related to the dynamical generation of massive constituent quarks. Thus, the chiral transition is the phase transition from a state in which the effective quark masses are spontaneously generated to one of massless quarks. The chiral condensate $\langle \bar{q}q \rangle$ is the order parameter for the chiral symmetry: it is non-zero when it is spontaneously broken, and zero when the symmetry is realized. Although the presence of the current quark masses in real QCD Lagrangian breaks explicitly the chiral symmetry, the chiral condensate $\langle \bar{q}q \rangle$ is still an useful quantity to study the partial restoration of the chiral symmetry.

1.2 The phase diagram of QCD

The phase diagram of QCD is a very timely subject of both theoretical and experimental studies. One of the main questions we seek to answer is ”what are the phases of strongly interacting matter?”. QCD predicts that when nuclear matter is compressed well beyond the density of atomic nuclei, a Quark-Gluon Plasma (QGP) made of asymptotically free quarks and gluons is created. The same phase transition is also predicted by QCD at extreme temperatures, as the ones found in the early universe. Therefore, under extreme conditions of density and/or temperature, the hadronic matter should undergo a phase transition into a QGP state.

If the baryonic chemical potential μ_B is asymptotically large, perturbative QCD methods can be applied. In this regime, the ground state of QCD at low temperatures should consist of Color SuperConducting (CSC) phases [8, 9], in which quark Cooper pairs are formed. Different Cooper pairing patterns should lead to distinct CSC phases [9]. In a range of small temperatures it is expected a first-order phase transition from hadronic matter to CSC phases. Based on several approaches that study the phase diagram at finite μ_B, it is expected that the analytic transition, seen in LQCD simulation at $\mu_B = 0$, turns into a discontinuous chiral transition at some critical point. This Critical-End-Point (CEP), at which the chiral phase transition changes its nature, is a fundamental landmark of the QCD phase diagram, remaining its location and even its existence an open issue. All these insights and expectations are reflected in Fig. 1.1, which is a structure map of the QCD phase diagram.

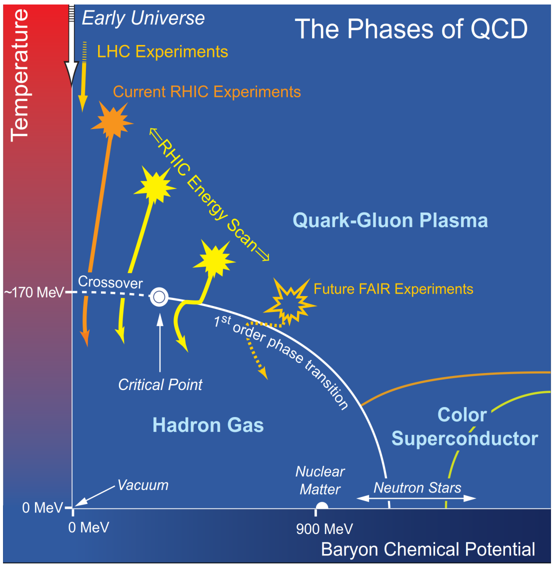

Figure 1.1: Schematic structure of the QCD matter. The phase boundaries are in solid lines and the different regions that can be probed by different HIC experiments are also shown. Figure adapted from [10].

A review of our current understanding of the phase structure of QCD can be found in [11]. A way of exploring the low temperature and high chemical potential region (few times the nuclear saturation density, $\rho_0 \sim 0.16$ fm^{-3}) is through astrophysical observations. In particular, the observation of neutron stars properties, such as their radius and mass, allows us to constraint the Equation of State (EOS) of dense QCD matter [10].

1.2.1 Heavy-Ion Collision experiments

The creation of the QGP has been one of the main goals of Heavy-Ion Collision (HIC) experiments. By the asymptotic freedom property of QCD, quasi-free states of quarks and gluons (QGP) predominates in matter created at sufficiently high temperature and density. Some signatures of the QGP were confirmed by the NA49 experiment at the CERN SPS: the evidence for the onset of deconfinement was found in central Pb+Pb collisions due to the rapid change of the energy dependence for the yields of pions and kaons as well as for the shape of the transverse mass spectra observed at 30A GeV [12]. QGP matter state was created, in the high temperature and low baryonic chemical potential region, in the Relativistic Heavy-Ion Collider (RHIC) at Brookhaven National Laboratory and, more recently, in the Large Hadron Collider at CERN. It was recognized already in RHIC that the QGP is a strongly coupled plasma, which behaves like an almost perfect liquid [13]. While RHIC is able to explore temperatures close to the phase transition, the LHC reaches temperatures well above those needed for the creation of QGP (see Fig. 1.1), allowing us to explore the expected transition from a strongly coupled liquid to a weakly coupled gaseous phase at higher temperatures [14].

The colder and denser region of the QCD phase diagram, i.e. lower temperature and high baryonic chemical potential, will be explored in the near future in HIC experiments such as in the Facility for Anti-proton and Ion Research (FAIR) at GSI Helmholtz Center for Heavy Ion Research or in the Nuclotron-based Ion Collider Facility (NICA) at Joint Institute for Nuclear Research (JINR) [15, 16].

There are several experimental programs, namely the Beam Energy Scan (BES-I) program at RHIC, which has been ongoing since 2010, looking for experimental signatures of a chiral first-order phase transition and the CEP, by colliding gold ions at several energies [17]. Recently, the results of the moments of net charge multiplicity distributions were presented by STAR Collaboration [18]. These measurements can provide relevant information on the freeze-out conditions and can help to clarify the existence of the CEP. However, future measurements with high statistics data will be needed for a precise determination of the freeze-out conditions and to make definitive conclusions regarding the CEP [18]. Also the dynamics associated with HIC, such as finite correlation length and freeze-out effects, should be considered in QCD calculations before definitive conclusions about the CEP can be made [19]. If the CEP exists and is located for baryonic chemical potential lower than 400 MeV, it is expected that the upcoming BES-II program can provide data on fluctuation and flow observables which should yield quantitative evidence for its presence. Also the NA61/SHINE program at the CERN SPS aims for the search of the CEP and to study the properties of the onset of deconfinement, through spectra fluctuations and correlations analysis in light and heavy ion collisions [20]. Otherwise, late in the decade, the FAIR facility at GSI and NICA at JINR will extend the search of the CEP to even higher baryonic chemical potential (for a review on the experimental search of the CEP see [21]). The experimental discovery of CEP would be a landmark and a huge step on our understanding of the different states of QCD matter.

1.2.2 Lattice QCD simulations

LQCD simulations with physical quark masses, at zero baryonic chemical potential, show an analytic transition, known as crossover, from ordinary hadronic matter to the QGP [22–24]. Real phase transitions are characterized by singular behavior at some temperature, allowing the definition of a critical temperature. In an analytic transition, due to the absence of singular behavior, we cannot define an unique critical temperature. Instead, only a pseudocritical temperature can be defined, using, for instance, the inflexion point or peak position of some thermodynamic observable. Thus, different pseudocritical temperatures can be obtained from different observables [22, 25, 26]. The analytic nature of the QCD transition with physical quark masses is related to the explicit breaking of the center and chiral symmetries. Therefore, the order parameters that signal the deconfinement and chiral phase transitions for real phase transitions, become only approximate in 2+1-flavors QCD with physical quark masses, showing an analytic behavior. Even though we keep using them as order parameters, they are merely observables, reflecting the analytic nature of both phase transitions. The order parameters used for chiral and deconfinement phase transitions are, normally, the renormalized chiral condensate and renormalized Polyakov loop, respectively. Both quantities are represented as a function of temperature in Fig. 1.2. The pseudocritical temperatures, calculated from the inflexion points, are 170 MeV for the deconfinement phase transition and 157 MeV for the chiral phase transition [25, 26]. A pseudocritical temperature range of $145 - 159$ MeV is obtained using other chiral and several thermodynamic observables [22, 26].

Although the temperature dependence of the Polyakov loop can be calculate in LQCD, it is difficult to define an inflection point and thus to define a pseudocritical temperature from the Polyakov loop [27]. Instead of the Polyakov loop, it is also possible to use the strange quark number susceptibility to define a deconfinement pseudocritical temperature. The strange quark number susceptibility c_2^s behaves in a similar way to the Polyakov loop and gives a pseudocritical temperature consistent with the one obtained from the Polyakov loop [25,26,28].

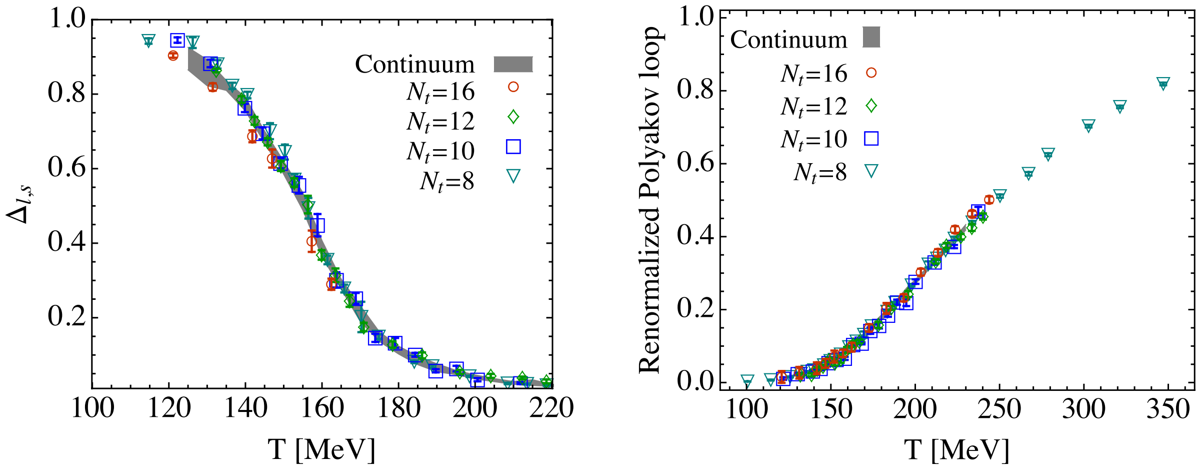

Figure 1.2: The subtracted chiral condensate $\Delta_{l,s}$ (left) and the renormalized Polyakov loop (right) as a function of temperature. The figures were taken from [26].

1.2.3 Strangeness and isospin asymmetry

There are several aspects that can influence the structure of the QCD phase diagram. Strangeness and isospin asymmetry are important degrees of freedom in the QCD phase diagram. While in HIC the proton fraction is currently not smaller than ~ 0.4, much smaller proton fractions are expected in the interior of neutron stars. The effect of isospin/charge asymmetry in the QCD phase diagram has recently been discussed in [29]. Due to its relevance, strangeness must be considered when discussing the QCD phase diagram.

As already mentioned, in nature the current masses of the quarks are not zero and their values control the explicit amount of chiral symmetry breaking. Because the strange quark is significantly heavier than both the up and down quarks ($m_s \approx 26 m_{ud}$), it induces a much higher amount of explicit symmetry breaking than its light partners. Considering the quark masses as external parameters and assuming isospin symmetry, i.e., $m_u = m_d$, the nature of the phase transition at $\mu_B = 0$ is given by the so-called Columbia plot of Fig. 1.3. In the limit of infinitely heavy quarks ($m_i \to \infty$) we recover the pure $SU(3)$ gauge theory, with a first-order deconfinement phase transition (top right region). In the opposite limit, for three massless quarks, a first-order chiral phase transition occurs (bottom left region). Between these two limits, for $0 < m_i < \infty$, the nature of both transitions depends on their exact values. We know from LQCD that in the physical point, i.e., using the real physical quark masses, both transitions are crossovers. When two massless quarks ($N_f = 2$) are considered, i.e., $m_u = m_d = 0$ and $m_s \to \infty$, the chiral phase transition is of second-order. Furthermore, for three massless quarks ($N_f = 3$) the chiral phase transition is of first-order. Therefore, when m_s is reduced from infinity to zero, there should exist a critical m_s value (tricritical point in Fig. 1.3) at which the nature of the phase transition changes from second to first-order [30–32].

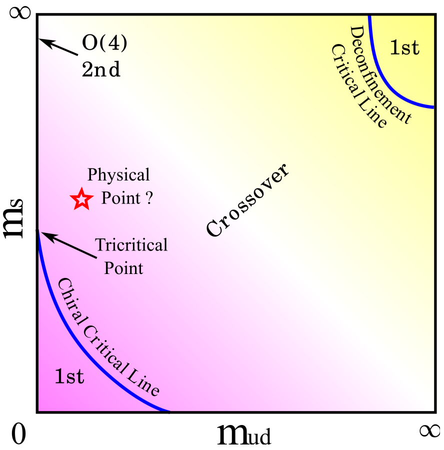

Figure 1.3: Schematic figure of the Columbia phase diagram for 3-flavor QCD at zero chemical potential as a function of the light and heavy quark masses. The right-top corner indicates the deconfinement phase transition in the pure gauge system. Figure taken from [11].

The relevance of strangeness is transversal to all regions across the phase diagram. In the interior of neutron stars (high density and low temperature region) it is expected that strangeness is present either in the form of hyperons, a kaon condensate or a core of deconfined quark matter [33]. The recent mass measurement of two solar masses millisecond pulsars PSR J1614−2230 [34] and PSR J1903+0327 [35] places quite strong constraints on the core composition of neutron stars. The compatibility of these large masses with the appearance of strangeness has been questioned on the basis of microscopic approaches to the hadronic equation of state [36–39]. Within a relativistic mean field approach it has been shown that it is still possible to accommodate these large masses even considering the presence of hyperons or kaons (see for instance [40–42]), since there is a large uncertainty on the coupling of hyperons to nucleons. Another possibility is that the interior of the neutron star contains a quark core [43].

In relativistic HIC the strange and multi-strange particle production is an important tool to investigate the properties of hot and dense matter created in the collision, since there is no net strangeness content in the initially colliding nuclei [44].

An enhanced production of strange particles in A$-$A compared to pp collisions was one of the first signatures proposed for the deconfined quark-gluon plasma [45, 46]. Very recently, the possibility of multiple chemical freeze-outs was suggested, in particular, the strange freeze-out that would indicate a clear separation of pion and kaon chemical freeze-outs [47]. Another alternative approach to treat the strange particle freeze-out separately, with the full chemical equilibrium, was presented in [48]: based on the conservation laws, the connection between the freeze-outs of strange and non-strange hadrons was achieved.

Strangeness freeze-out in HIC is also getting the attention of LQCD community. It was found that experimentally unobserved strange hadrons become thermodynamically relevant in the vicinity of the QCD crossover, modifying the yields the ground state of strange hadrons in HIC, which leads to significant reductions in the chemical freeze-out temperature of strange hadrons [49]. However, the question of whether hadrons of different quark composition freeze out simultaneously or exhibit a flavor hierarchy is yet to be answered [50].

1.2.4 The presence of an external magnetic field

The QCD phase diagram also depends on external parameters, such as the presence of a magnetic field, that are interesting to investigate from both experimental and theoretical points of view. Due to its far-reaching consequences in all regions of the phase diagram, understanding QCD matter under extremely intense magnetic fields is one of the most relevant topics in modern physics. Indeed, the compact astrophysical objects known as magnetars [51], which include soft gamma repeaters and anomalous x-ray pulsars, are expected to have very strong magnetic fields in their interior. In HIC it is also important to consider the presence of magnetic fields, although time dependent and short lived [52, 53], they can reach high intensities (of the order of $eB \sim 5 - 30\ m_\pi^2$) and temperatures varying from 120 to 200 MeV. The estimated value of the magnetic field strength for the LHC energy, for example, is of the order of $eB \sim 15\ m_\pi^2$ [54]. Furthermore, the magnetic field might have played an important role in the first phases of the universe [55, 56].

At finite temperature, several LQCD studies have been performed to address the influence of the magnetic field over the deconfinement and the chiral transitions [57–63]. For a review in recent advances in the understanding of the phase diagram in the presence of strong magnetic fields at zero quark chemical potentials see [64].

1.3 Quark matter under external magnetic fields

1.3.1 Theoretical frameworks

The effect of a constant external magnetic field in quark matter has been widely studied using several effective models, which includes: the Nambu–Jona-Lasinio (NJL) model [65–94], the Polyakov extended Nambu–Jona-Lasinio (PNJL) model [95–107], the Hadron Resonance Gas (HRG) model [108], the Polyakov extended Linear-Sigma model [109, 110], the MIT bag model [111–113], and the Quark-Meson model (QMM) [114–117]. The impact of B was also investigated within the Chiral Perturbation Theory (QPT) [118–122], the Function Renormalization Group (FRG) [64, 123, 124], and the Sakai-Sugimoto holographic model [125–133].

The properties of quark matter in a magnetic field were investigated within the NJL model for cold two-flavors [70], three-flavors [71, 77, 86], and three-flavors at finite temperature [72, 89]. In [89] the contribution of the magnetized gluons to the EOS of quark matter was estimated. The QCD phase diagram structure in the presence of a magnetic field was analyzed within the NJL model [75, 76, 78, 82, 84], PNJL model [106], and within the FRG approach [123]. The introduction of an axial chemical potential and its impact on phase transitions, and thus on QCD phase structure, is explored in the NJL model [67, 87], PNJL model [95, 96], and in the PNJL model with entanglement and vector interactions [100]. The dressed Polyakov loop in a magnetic field was studied in [97]. The formation and stability of quark droplets in a magnetized environment was evaluated in [68]. The effect of the anomalous magnetic moment of quarks on thermodynamical properties was analyzed in [66]. Conserved charged correlations [101] and the surface tension of quark matter [73] were also studied in a magnetic field presence.

The impact of an external magnetic field on mesons was explored in two-flavor NJL model [65, 79, 83], CPT [121, 122], FRG [83], and Sakai-Sugimoto model [128, 130, 133], being some of the main conclusions:

- the possible condensation of the charged vector meson in the vacuum [65, 130, 133];
- the explicit breaking of Lorentz invariance by the magnetic field induces anisotropies in the refraction index and screening mass of neutral mesons [79];
- the quark-pion coupling and neutral pion decay constants are different in longitudinal and transverse directions [83];
- the mass and decay constants of charged and neutral pions split, and the transverse velocity of mesons decreases with B at all temperatures [121, 122].

1.3.2 The Magnetic Catalysis effect

The magnetic field has an impact on the dynamics of many physical systems, and the relation of dimensional reduction with the symmetry breaking has been extensively studied (for a recent review see [134]). An external constant magnetic field enhances the generation of the fermion mass in 3+1 dimensions, and thus increases the strength of chiral symmetry breaking [135, 136]. The underlying physics of such mechanism, called Magnetic Catalysis (MC), was explored in [137–139]. It was found that the dimensional reduction $D \to D-2$ is the origin of the MC phenomenon: the charged fermions are restricted to quantized Landau levels in the transverse plane of the applied magnetic field. The fermion paring, responsible for the chiral condensate formation, is mainly provided by the fermions in the lowest Landau level, whose dynamics is $(D-2)-$dimensional. Even at the weakest attractive fermion-antifermion interaction, the magnetic field leads to a generation of a fermion mass, catalyzing the dynamical chiral symmetry breaking mechanism. MC has been extensively studied in the literature, and its model-independent nature suggests that it occurs for any fermion-antifermion attractive interaction [134].

1.3.3 Lattice QCD simulations

At finite temperature and zero baryonic chemical potential, the effect of a constant external magnetic field on the properties of QCD matter has been the subject of several studies using numerical simulations of LQCD [61–63, 140–145]. The earlier LQCD simulations [62, 142, 143] using larger-than-physical quark masses supported the existence of the MC mechanism at any temperature. In [62], the properties of chiral and deconfinement transitions in the presence of a constant external magnetic field were investigated for two-flavor QCD with pion masses in the range $200-480$ MeV. Both pseudocritical temperatures increase ($< 2\%$ for $eB \sim 0.75$ GeV^2) and the transitions become sharper with growing B.

More recent LQCD studies [57–61, 63], which we will review below, were able to bring down the quark masses to the respective physical values in their simulations. The effect of an external magnetic field on the QCD phase transition at finite temperature, for $N_f = 2+1$ flavors with physical quark masses, was performed in [57]. It was found that the dependence of the quark condensates on B is non-monotonic and varies strongly with temperature (left panel of Fig. 1.4), and, as a result, the chiral pseudocritical temperature T_c decreases with B (right panel of Fig. 1.4).

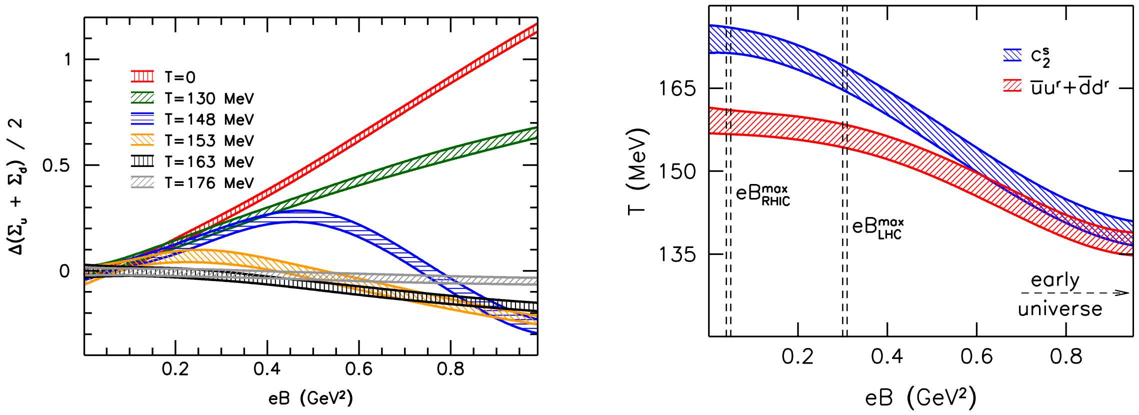

Figure 1.4: The average light quark condensate as a function of B for several temperatures (left), and the critical temperatures calculated from the inflexion points of the quark condensate and the strange quark number susceptibility (right). The figures were taken from [60] (left) and [57] (right).

The magnetic field suppresses the quark condensate near the transition temperature, an effect known as Inverse Magnetic Catalysis (IMC), resulting in its non-monotonic behavior as a function of B for certain temperatures (left panel of Fig. 1.4). This behavior of T_c is also supported by analyzing the chiral susceptibility (right panel of Fig. 1.4). The non-monotonic behavior of the condensate depends on the quark masses: for quarks having the physical strange quark mass value, a monotonic behavior with B is obtained at any temperature. This might explain the discrepancy with other LQCD results, where larger-than-physical quark masses were used. The chiral susceptibility shows that the phase transition remains a crossover, at least up to $eB = 1.05$ GeV^2, even though it gets stronger with increasing B. In [60], the chiral and strange quark condensates were calculated as a function of B for several temperatures. As in [57], the behavior of the chiral condensate with B strongly depends on the temperature. At low temperatures, the chiral condensate has a monotonic behavior with B, in accordance with the MC mechanism, but a non-monotonic behavior is obtained for temperatures near the transition temperature. On the other hand, the strange quark condensate has a simple monotonic dependence with B and with temperature: it increases with B at any temperature. This seems to indicate the existence of a certain mass threshold value between the physical light and strange quark masses, above which the IMC effect is not seen.

A decreasing critical temperature with B was also obtained analyzing the behavior of other thermodynamic observables of the QCD equation of state for $N_f = 2+1$ flavors with physical quark masses [59], in agreement with the previous results for the light quark condensate, strange quark number susceptibility, and the Polyakov loop observables.

In [58], the transition temperature of deconfinement, obtained from the renormalized Polyakov loop, decreases with the magnetic field strength. It agrees with the results for the strange quark number susceptibility of [57] (see right panel of Fig. 1.4).

The gluonic contribution to the interaction measure in a constant magnetic field was studied in [146]. As for quarks, also the gluonic contribution is enhanced at low temperatures and suppressed near the transition temperature. Therefore, gluons, like the light quarks, undergo MC and IMC, even though they do not interact directly with the magnetic field (gluons do not carry electric charge), but only indirectly via quark loops.

The IMC scenario was also supported by other recent LQCD studies: the deconfinement transition temperature decreases with B [63], and a non-monotonic behavior of the condensate for $eB < 0.8$ GeV^2 was obtained in [61].

The effect of strong B on chiral symmetry breaking in quenched and unquenched QCD is studied in [147]. It was found a weakening of the MC effect caused by the back-reaction of quarks on Yang-Mills sector. Aside from the MC effect on the quark sector, the unquenched effects in the gluonic sector contribute to the condensate suppression, in agreement with the LQCD result [58].

Recently, it was shown that the IMC prevails at the transition temperature region up to $eB = 3.25$ GeV^2 [148]. Evidence of a first-order phase transition was found in the asymptotically strong magnetic field limit of QCD, implying the existence of a CEP in the $T-B$ phase diagram [148].

1.3.4 The Inverse Magnetic Catalysis effect

A physical mechanism behind IMC was proposed in [58], which we summarize in the following. The effect of the magnetic field on chiral symmetry breaking was separated in two distinct and competing mechanisms: sea and valence effects. The former enhances the quark condensate while the later suppresses it in the transition region. Both effects rely on the interaction between the magnetic field and low quark modes. The magnetic field explicitly appears in the Dirac operator and directly influences its spectrum in any fixed gauge background. This is the valence effect and explains the MC mechanism: the magnetic field enhances the spectral density around zero, and thus, through the Banks-Casher relation [149], the quark condensate. The other mechanism, the sea effect, arises from the B dependence of the quark action, affecting the relative weight of different gauge configurations in the path integral. The relative strength of both effects determines whether MC or IMC occurs at a certain temperature. Around the transition temperature, they show opposite effects: the suppression sea effect overcomes the enhancement valence effect of the quark condensate, resulting in a net suppression of the condensate in that temperature region (IMC). Furthermore, it was shown that their relative strength strongly depends on the quark masses; thus, in order to describe IMC, the physical quark masses must be used. The sea effect, responsible for weakening of the quark condensate around the transition temperature, is a consequence of re-weight of gauge configurations in the path integral due to B. This re-weight disfavors small and favors large values of the Polyakov loop expectation value, being more intense near the transition temperature.

The physical mechanism behind the IMC phenomena is the subject of several recent studies. It is argued in [150, 151] that the disagreement between effective model predictions and the LQCD results can be explained if the mass gap is B-independent, and of the order of $\sim \Lambda_{QCD}$. If this is the case, the decreasing of the critical temperatures would be natural: the Boltzmann factor remains of similar magnitude as B increases ($\sim e^{-\Lambda_{QCD}/T}$). The authors argued that a B-independent mass gap of $O(\Lambda_{QCD})$ can be obtained if it is dominantly generated by the nonperturbative force mediated by the *IR* gluons. Both *IR* enhancement and *UV* suppression of gluon exchanges are crucial to obtain a B-independent mass gap.

The Magnetic Inhibition mechanism was proposed in [152]: neutral mesons also experience the dimensional reduction in strong magnetic fields, resulting in the quark condensate suppression. Using a chiral model, the propagator of π^0 was calculated in strong B and it favors the chiral-symmetric phase, i.e., it has the opposite effect of MC. The magnetic inhibition is enhanced by the temperature effects and can overcome the MC at finite temperature.

Another proposed mechanism for IMC is given by the sphaleron transitions [81] that occur near the transition temperature. The chiral imbalance generated by the sphaleron transitions near the transition temperature is enhanced by B, destroying the chiral paring and reducing the critical temperature of the chiral phase transition. The chemical potential, which describes the chiral imbalance, is induced dynamically by an axial-vector interaction within NJL models in [88, 153].

The IMC crucially depends on the interaction between the quark determinant and the Polyakov loop, which happens at the lowest part of the Dirac spectrum [58]. The increase of the Polyakov loop value with B suppresses low Dirac eigenvalues, and thus the quark condensate is reduced. In the PNJL model the Polyakov loop decreases with the magnetic field; therefore, the deconfinement pseudocritical transition temperature increases. In order to describe IMC within effective models, the increase of the Polyakov loop with B should be taken into account. In [107], we have proposed that the increase of the Polyakov loop value with B could be reproduced using a magnetic field dependence on T_0 that is the only free parameter of the Polyakov loop potential. Moreover, in order to reproduce IMC, the entanglement interaction was required, i.e., the IMC was only reproduced within the EPNJL model. Due to the explicit dependence of the quark interaction coupling on the Polyakov loop, the entanglement interaction is responsible, through the imposed magnetic field dependence on T_0, for the weakening of the four-quark scalar coupling with B.

Later in [104], we have proposed that the LQCD results on IMC could also be reproduced qualitatively within both NJL and PNJL models, if we assume that the magnetic field weakens the scalar four-quark coupling of the model. The scalar coupling dependence on B can be traced back to the impact that the magnetic field has on the QCD running coupling.

Finally, other approaches are in accordance with IMC. A decreasing critical temperature of deconfinement with increasing B was found in hard-wall AdS/QCD, and holographic duals of flavored and unflavored $\mathcal{N} = 4$ super-Yang Mills theories [154].

The gluon and quark gap equations in a magnetic field were calculated in [155]. The underlying mechanism of IMC was attributed to the combination of gluon screening and the weakening of the strong coupling with B. Several other studies point in the same direction [156–158]. The thermo-magnetic correction to the quark-gluon vertex in the presence of a weak magnetic field, within the hard thermal loop approximation, was computed in [156], showing that the effective thermo-magnetic quark-gluon coupling decreases with B. The thermo-magnetic effect was also explored in the linear sigma model at one-loop level, giving a decreasing critical temperature with B [157]. The one-loop thermo-magnetic correction to the self-coupling was calculated in a model where charge scalars interact with B, and it was shown to decrease with the magnetic field [158].

1.4 Work outline

This thesis is organized as follows. The local and global symmetries of QCD are briefly reviewed in Chapter 2. The model formalism is introduced in Chapter 3. Chapter 4 is based on our published results [103, 105, 107], where the effect of the magnetic field on the quark condensates, and particularly, on both chiral and deconfinement phase transitions is studied, within both PNJL and EPNJL models. The influence of the magnetic field on the strange quark is analyzed, and also the impact of both the ’t Hooft term and the current mass value of the strange quark on the pseudocritical phase transition temperatures. The comparison between the model predictions and the recent LQCD results, which was published in [107], is discussed in Chapter 5.

Two approaches that reproduce the IMC effect are presented in Chapter 6, which we have proposed in [104, 107]. Using the PNJL model that reproduces the IMC at zero baryon chemical potential, we analyze the QCD phase diagram at finite baryonic potential in Chapter 7. In particular, we focus on how the magnetic field affects the CEP location. The results were published in [106, 159].

Finally, the conclusions of this study are drawn in Chapter 8.

Chapter 2

Theory of the strong interactions

Quantum Chromodynamics (QCD) is presently the theory of strong interactions. Two of its important features are the chiral and center symmetries. These two symmetries are realized in opposite limits of QCD: the center symmetry is an exact symmetry in pure gauge theory (heavy-quark limit), and the chiral symmetry, on the other hand, is an exact symmetry in the massless QCD (massless quark limit). In nature, i.e., QCD with physical quark masses, both symmetries are only approximate but still useful to study chiral and deconfinement transitions.

2.1 Local gauge symmetry

The QCD is a non-abelian gauge theory with an $SU(3)$ gauge group. Its Lagrangian is written as

$$\mathcal{L}_{QCD} = \sum_f \bar{q}_f \left(i\gamma^\mu D_\mu - m_f\right) q_f - \frac{1}{4} G^a_{\mu\nu} G^{\mu\nu}_a \tag{2.1}$$

where q_f ($\bar{q}_f$) is the quark (anti-quark) field for the f-flavor ($f = u, d, s, c, t, b$) and m_f is the f-flavor current quark mass. The quark masses are given in Table 2.1. The local $SU(3)$ gauge invariance requires that the covariant derivative D_μ has the following form

$$D_\mu = \partial_\mu - igt^a A^a_\mu, \tag{2.2}$$

where g is the QCD coupling, and $t^a = \lambda^a/2$ are the generators of the Lie algebra of $SU(3)$ with λ^a representing the Gell-Mann matrices [1]. The gluon field strength tensor is

$$G^a_{\mu\nu} = \partial_\mu A^a_\nu - \partial_\nu A^a_\mu - gf^{abc} A^b_\mu A^c_\nu, \tag{2.3}$$

---

[1] We give a short review of the properties of the $SU(N)$ group in Appendix A.

where f^{abc} are the anti-symmetric structure constants of the $SU(3)$ group (see Appendix A).

Flavor	Electric Charge (e)	Mass [160]
u	$2/3$	$2.3^{+0.7}_{-0.5}$ MeV
d	$-1/3$	$4.8^{+0.5}_{-0.3}$ MeV
s	$-1/3$	95 ± 5 MeV
c	$2/3$	1.275 ± 0.025 GeV
b	$-1/3$	4.18 ± 0.03 GeV
t	$2/3$	160.5^{+5}_{-4} GeV

Table 2.1: The quark masses and electric charges (natural units are used, $c = 1$).

In fact, the QCD Lagrangian can be constructed starting from the free fermionic field Lagrangian

$$\mathcal{L} = \bar{q}\left(i\gamma^{\mu}\partial_{\mu} - m\right)q, \tag{2.4}$$

and demanding it to be invariant under a local gauge transformation of the quarks fields:

$$q(x) \rightarrow q^{'}(x) = U(x)q(x), \tag{2.5}$$

with

$$U(x) = \exp\left(-it^{a}\theta_{a}(x)\right), \tag{2.6}$$

where $\theta_a(x)$ are space-time dependent real parameters; the space-time dependence of the transformation parameters defines a local transformation.

The requirement of a local gauge invariance is only realized if the partial derivative ∂_μ is replaced by the covariant derivative

$$D_{\mu} = \partial_{\mu} - igA^{\mu}, \tag{2.7}$$

where a vector gauge field A^μ term appears, which consists of eight A^a_μ fields

$$A^{\mu}(x) = \frac{\lambda^{a}}{2}A^{a}_{\mu}(x) = \tau^{a}A^{a}_{\mu}(x) \quad (a = 1, ..., 8). \tag{2.8}$$

We see that the interaction between the gauge and the quark fields is a consequence of the local gauge invariance requirement of the theory. Under a local gauge transformation the gauge field $A^\mu(x)$ transforms as

$$A_{\mu}(x) \rightarrow A^{'}_{\mu}(x) = U\left(A_{\mu}(x) - \frac{i}{g}U^{\dagger}\partial_{\mu}U\right)U^{\dagger}. \tag{2.9}$$

The gauge invariance implies that the gauge field A^μ must be massless, i.e., a $A_\mu A^\mu$ term would break explicitly the gauge invariance.

The kinetic term of the gauge fields,

$$\mathcal{L}_{kin} = \frac{1}{4} G^a_{\mu\nu} G^{\mu\nu}_a, \tag{2.10}$$

must also be invariant under a local $SU(3)$ gauge transformation. For that the field strength tensor must be modified as $G^a_{\mu\nu} = \partial_\mu A^a_\nu - \partial_\nu A^a_\mu - g f^{abc} A^b_\mu A^c_\nu$. Therefore, starting with the free fermion Lagrangian [Eq. (2.4)] and requiring an invariance under local gauge transformations [Eqs. (2.5)-(2.6)] we have arrived at the QCD Lagrangian [Eq. (2.1)]. The requirement of a $SU(3)$ local gauge invariance has created not only quark-quark and quark-gluon interactions terms, but also three and four gluon auto-interaction terms. These auto-interaction terms of the gauge fields, which are absent in quantum electrodynamics, are responsible for the nonperturbative effects of QCD.

2.2 Global symmetries

Besides the local $SU(3)$ gauge symmetry of the QCD Lagrangian, there are also global symmetries. The global symmetries are defined through space-time independent transformation parameters. For global symmetries the space-time dependent parameters $\theta_a(x)$ of Eqs. (2.5) and (2.6) become constant parameters θ_a .

In the limit of vanishing quark masses (chiral limit) the QCD Lagrangian is invariant under the group of transformations

$$U(3)_L \otimes U(3)_R = SU(3)_L \otimes SU(3)_R \otimes U(1)_L \otimes U(1)_R,$$

which can be separated into axial and vector transformations,

$$U(3)_L \otimes U(3)_R = SU(3)_V \otimes SU(3)_A \otimes U(1)_V \otimes U(1)_A.$$

According to Noether's theorem, for each conserved symmetry there is a conserved current. In Table 2.2 we show the transformations under which the QCD Lagrangian is invariant, the conserved currents, and the manifestations of these symmetries in Nature. The $SU(3)_V$ and $U(1)_V$ symmetries ensure the conservation of isospin and baryon number, respectively, while the $SU(3)_A$ and $U(1)_A$ symmetries are transformations that involve the γ_5 matrix and thus change the parity.

To make clear the difference between spontaneously and explicitly symmetry breaking let us discuss each symmetry separately.

Symmetry	Transformation	Current	Name	Manifestation in Nature
$SU(3)_V$	$q \to \exp(-it^a\alpha_a)q$	$V^a_\mu = \bar{q}\gamma_\mu t^a q$	Isospin	Approximately conserved
$U(1)_V$	$q \to \exp(-i\alpha_V)q$	$V_\mu = \bar{q}\gamma_\mu q$	Baryonic	Conserved
$SU(3)_A$	$q \to \exp(-i\gamma_5 t^a\theta_a)q$	$A^a_\mu = \bar{q}\gamma_\mu\gamma_5 t^a q$	Chiral	Spontaneously broken
$U(1)_A$	$q \to \exp(-i\gamma_5\alpha_A)q$	$A_\mu = \bar{q}\gamma_\mu\gamma_5 q$	Axial	“ $U_A(1)$ problem”

Table 2.2: The QCD symmetries in the chiral limit.

2.2.1 Chiral symmetry

In the chiral limit, i.e., $m_u = m_d = m_s = 0$, the $\mathcal{L}_{QCD}$ in invariant under chiral symmetry $SU(3)_L \otimes SU(3)_R$ transformations. The quark spinors can be separated into right- and left-handed contributions

$$q_R = P_R q, \qquad q_L = P_L q, \tag{2.11}$$

where $P_{R,L}$ are the projection operators,

$$P_R = \frac{1}{2}(1+\gamma_5), \qquad P_L = \frac{1}{2}(1-\gamma_5). \tag{2.12}$$

The group of transformations $SU(3)_L \otimes SU(3)_R$ can be parametrized as

$$q_{R,L} = \exp\left(i\theta^a_{R,L}\lambda^a/2\right) q_{R,L}, \tag{2.13}$$

and the conserved current,

$$j^\mu_{R,L} = \bar{q}_{R,L}\gamma_\mu \frac{\lambda^a}{2} q_{R,L}, \tag{2.14}$$

can be written as a combination of vector and axial-vector currents:

$$V^a_\mu = j^a_{R,\mu} + j^a_{L,\mu} \tag{2.15}$$

$$A^a_\mu = j^a_{R,\mu} - j^a_{L,\mu}. \tag{2.16}$$

Therefore, the $SU(3)_L \otimes SU(3)_R$ group can be rewritten as

$$SU(3)_L \otimes SU(3)_R = SU(3)_V \otimes SU(3)_A.$$

The nontrivial QCD vacuum is responsible for the spontaneously breaking of chiral symmetry

$$SU(3)_L \otimes SU(3)_R \to SU(3)_V,$$

which is closely related to the existence of non-zero quark condensate $\langle\bar{q}q\rangle$,

$$\langle\bar{q}q\rangle = \langle 0|\bar{q}q|0\rangle = \langle 0|\bar{u}u|0\rangle + \langle 0|\bar{d}d|0\rangle + \langle 0|\bar{s}s|0\rangle. \tag{2.17}$$

A non-vanishing value of the quark condensate leads to the spontaneous breaking of the chiral symmetry, because the operator

$$\bar{q}q = \bar{q}_R q_L + \bar{q}_L q_R \tag{2.18}$$

mixes left- and right-handed quarks and is not invariant under chiral symmetry. Hence, the quark condensate can be used as an order parameter for the chiral symmetry,

$$\langle \bar{q}q \rangle \Rightarrow \begin{cases} \neq 0 & \rightarrow \quad \text{broken chiral symmetry} \\ = 0 & \rightarrow \quad \text{unbroken chiral symmetry.} \end{cases} \tag{2.19}$$

The order parameter is a quantity that defines the state of the system, i.e., it vanishes when the state of the system shares the symmetry and it becomes non-zero when the symmetry is broken.

From the experimental point of view the manifestation of chiral symmetry would be the existence of parity doublets, i.e., a multiplet of particles with the same mass and opposite parity for each multiplet of isospin (the chiral partners), in the hadronic spectrum, which is not seen in Nature.

Furthermore, the chiral symmetry is not only spontaneously broken by the QCD vacuum, but also explicitly by the Lagrangian mass term $m\bar{q}q$, when the quark masses are taken into account. In this case, the chiral symmetry is explicitly broken and the quark condensates will always have non-zero value.

Moreover, when the different quark masses are taken into account, also the $SU(3)_V$ is explicitly broken (flavor symmetry breaking). Thus, when physical quark masses are used, the chiral symmetry $SU(3)_L \otimes SU(3)_R$ is explicitly broken, and we have

$$SU(3)_L \otimes SU(3)_R \otimes U(1)_L \otimes U(1)_R \rightarrow U(1)_L \otimes U(1)_R = U(1)_A \otimes U(1)_V .$$

2.2.2 Axial symmetry

In the chiral limit, the $\mathcal{L}_{QCD}$ is also invariant under $U(1)_A$ transformation (axial symmetry). It is easy to show that the axial-vector current $j_5^\mu = \bar{q}\gamma^\mu\gamma_5 q$ is conserved ($\partial_\mu j_5^\mu = 0$) at classical level, but in quantum field theory an anomalous term appears in the divergence of axial-vector current,

$$\partial_\mu j_5^\mu = -\frac{3g^2}{32\pi^2}\epsilon^{\mu\nu\lambda\sigma}G^a_{\mu\nu}G^a_{\lambda\sigma}, \tag{2.20}$$

even in the chiral limit. Using the functional integral, the entire generating functional must be invariant under the $U(1)_A$ transformation and not only the action [161]. The anomalous term is precisely the nontrivial contribution coming from the measure of the generating functional under the transformation. In fact, a consistent quantum field theory requires modification of the short distance behavior and leads to the breaking of axial symmetry [162].

If the symmetry $U(1)_A$ was a true symmetry of QCD it would imply the existence of a partner with opposite parity to each hadron. This is not experimentally observed and therefore the symmetry must be broken.

In the end, only the $U(1)_V$ symmetry remains unbroken in the $\mathcal{L}_{QCD}$,

$$SU(3)_L \otimes SU(3)_R \otimes U(1)_L \otimes U(1)_R \to U(1)_V,$$

reflecting the conservation of baryon number.

2.2.3 Center symmetry

If we start from the QCD Lagrangian and impose the heavy-quark limit ($m_q \to \infty$), we end up with pure gauge theory. Center symmetry is present in pure gauge theory and is related, as we will see, to confinement.

The partition function in pure gauge theory is given by

$$\mathcal{Z} = \int \mathcal{D}A_\mu \exp(-S_{PG}) \tag{2.21}$$

where S_{PG} is the Euclidean pure gauge action

$$S_{PG} = -\frac{1}{2}\int_0^\beta d\tau \int d^3x \, \mathrm{Tr}(G_{\mu\nu}G_{\mu\nu}), \tag{2.22}$$

where the inverse temperature β plays the role of Euclidean time interval it. The measure $\mathcal{D}A_\mu$ must fulfill the bosonic periodic boundary condition

$$A_\mu(\mathbf{x}, \tau + \beta) = A_\mu(\mathbf{x}, \tau), \tag{2.23}$$

in Euclidean time direction. To satisfy the above periodic boundary condition, the local gauge invariance transformation,

$$U(\mathbf{x}, \tau) = \exp\left(-it^a\theta_a(\mathbf{x}, \tau)\right), \tag{2.24}$$

must be periodic in Euclidean time,

$$U(\mathbf{x}, \tau + \beta) = U(\mathbf{x}, \tau). \tag{2.25}$$

Nevertheless, Eq. (2.23) is also preserved under the so-called twist transformation

$$U(\mathbf{x},\tau+\beta)=zU(\mathbf{x},\tau), \tag{2.26}$$

where the matrix z is an element of center symmetry $\mathbb{Z}_3$ of the $SU(3)$ group:

$$z\in\mathbb{Z}_3=\mathbb{I}\left\{e^{2i\pi/3},e^{4i\pi/3},e^{2i\pi}\right\}\qquad\text{with}\qquad\mathbb{Z}_3\subset SU(3),$$

where $\mathbb{I}=\mathrm{diag}(1,1,1)$ is the identity matrix. It is straightforward to verify that the elements of $\mathbb{Z}_3$ commute with all elements of $SU(3)$ group. Therefore, pure gauge theory possesses center symmetry.

In the presence of fermionic fields, which obey the anti-periodic boundary conditions

$$q(\mathbf{x},\tau+\beta)=-q(\mathbf{x},\tau), \tag{2.27}$$

under local gauge transformations $q^{'}=Uq$ transform as

$$q'(\mathbf{x},\tau+\beta)=-zq'(\mathbf{x},\tau). \tag{2.28}$$

The only possible value for z is 1. Thus, the presence of fermionic fields explicitly breaks the center symmetry.

The connection of the center symmetry with confinement is the following: if the center symmetry is explicitly broken by the presence of fermionic fields, or spontaneously broken that happens at high temperature, then the quark potential cannot be linear asymptotically [163].

An order parameter for the center symmetry and thus confinement/deconfinement phase transition is the expectation value of the Polyakov loop

$$\langle\Phi(\mathbf{x})\rangle=\left\langle\frac{1}{3}\,\mathrm{Tr}\left[L(\mathbf{x})\right]\right\rangle. \tag{2.29}$$

The Polyakov loop operator $L(\mathbf{x})$ is defined through a closed Wilson loop around the periodic imaginary time direction

$$L(\mathbf{x})=\mathcal{P}\exp\left\{i\int_0^\beta d\tau A_4(\mathbf{x},\tau)\right\}, \tag{2.30}$$

where, $A_4=iA_0$ is the temporal component of the Euclidean gauge field (A,A_4), and $\mathcal{P}$ denotes path ordering. The expectation value of the Polyakov loop under the center symmetry transformation is given by

$$\langle\Phi(\mathbf{x})\rangle\to z\langle\Phi(\mathbf{x})\rangle. \tag{2.31}$$

Since the expectation value of the Polyakov loop is not invariant under a global center symmetry, its value can be used as order parameter for the spontaneous breaking of the center symmetry:

$$\langle \Phi(\mathbf{x}) \rangle \Rightarrow \begin{cases} = 0 & \text{unbroken center symmetry} \\ \neq 0 & \text{broken center symmetry} \end{cases} \tag{2.32}$$

We can write $\langle \Phi(\mathrm{x}) \rangle$ as

$$\langle \Phi(\mathbf{x}) \rangle = \exp\left(-\beta \Delta F_q(\mathbf{x})\right), \tag{2.33}$$

where ΔF_q is the difference between the free energy of a gauge field theory containing an isolated and static quark, and the free energy of a pure gauge system [7,164]. In a confined phase, an infinite amount of free energy is required to add an isolated quark to the system, thus $\langle \Phi(\mathrm{x}) \rangle = 0$, and then we are in an unbroken center symmetry phase (confined phase). On the other hand, when $\langle \Phi(\mathrm{x}) \rangle \neq 0$ means that $\Delta F_q(\mathrm{x}) \to$ finite that signals a deconfined phase.

The quark fields break explicitly the center symmetry in QCD and $\Phi(\mathrm{x})$ has no longer a zero expectation value. Anyway, the $\langle \Phi(\mathrm{x}) \rangle$ still is though an useful quantity to study the deconfinement transition.

Chapter 3

Model formalism

The Nambu–Jona-Lasinio (NJL) model was proposed by Y. Nambu and G. Jona-Lasinio in 1961 to explain the origin of the nucleon mass through the spontaneous breaking of chiral symmetry [165, 166]. It was introduced on the grounds of an analogy with the formation of an energy gap in the theory of superconductivity by Bardeen, Cooper and Schrieffer (the so-called BCS theory). At that time, the model was formulated in terms of nucleons, pions and scalar sigma mesons. Nowadays, the fermionic degrees of freedom are associated with quarks. One of the features of the model is the dynamical generation of a fermion mass through the breaking of chiral symmetry: the spontaneous formation of a quark-antiquark pairs (like the electron-electron paring in BSC theory) occurs if the attractive interaction between quarks and antiquarks is strong enough.

The NJL model has been successful in explaining the dynamics of spontaneous breaking of chiral symmetry, one of the important features of QCD, and its restoration at high temperatures and densities/chemical potentials [167–170].

3.1 Three-flavor NJL model Lagrangian

The Lagrangian of the three-flavor NJL model is given by [169, 170]:

$$\mathcal{L}_{NJL} = \mathcal{L}_0 + \mathcal{L}_4 + \mathcal{L}_6 \tag{3.1}$$

$$\mathcal{L}_0 = \bar{q}(i\gamma^\mu\partial_\mu - \hat{m})q = \bar{q}(i\gamma^\mu\partial_\mu)q - \bar{q}\hat{m}q = \mathcal{L}_{kin} + \mathcal{L}_{mass} \tag{3.2}$$

$$\mathcal{L}_4 = \frac{1}{2}G_s^0 \sum_{a=0}^{8} [\,(\,\bar{q}\,\lambda^a\,q\,)^2 \;+\; (\,\bar{q}\,i\,\gamma_5\,\lambda^a\,q\,)^2\,] \tag{3.3}$$

$$\mathcal{L}_6 = K\,\{\text{det}\,[\bar{q}\,(1+\gamma_5)\,q] + \text{det}\,[\bar{q}\,(1-\gamma_5)\,q]\}. \tag{3.4}$$

In the above, $q = (u, d, s)$ is the quark field with three flavors ($N_f = 3$) and three colors ($N_c = 3$), $\hat{m} = \text{diag}(m_u, m_d, m_s)$ is the current quark mass matrix, and λ^a are the flavor SU$_f$(3) Gell-Mann matrices ($a = 1, \ldots, 8$), with $\lambda^0 = \sqrt{\frac{2}{3}}\mathbf{I}$ (see Appendix A).

The $\mathcal{L}_4$ term is a chirally symmetric scalar-pseudoscalar local four-point interaction. In the chiral limit (i.e., with $\mathcal{L}_{mass} = -\bar{q}\hat{m}q = 0$), the combination $\mathcal{L}_0 + \mathcal{L}_4$ is invariant under

$$SU(3)_{\text{color}} \otimes U(3)_L \otimes U(3)_R = SU(3)_{\text{color}} \otimes SU(3)_L \otimes SU(3)_R \otimes U(1)_V \otimes U(1)_A,$$

where the $SU(3)_{\text{color}}$ is a global – and not local, as in QCD – color symmetry. The reduction to a global color symmetry prevents quark confinement in the model.

In the other hand, 't Hooft suggested that the breaking of the $U(1)_A$ symmetry can be described at the semi-classical level by instantons [171, 172]. The instantons can play a crucial role in breaking explicitly the $U(1)_A$ symmetry, explaining the different nature of the η' meson mass. The $U(1)_A$ anomaly is responsible for the flavor mixing effect that removes the degeneracy among several mesons. To mimic this interaction in a purely fermionic effective theory, 't Hooft proposed the six quarks interaction term $\mathcal{L}_6$ that breaks the $U(1)_A$ symmetry and reproduces the axial anomaly. Therefore, the $\mathcal{L}_6$ term breaks the $U(3)_L \otimes U(3)_R$ symmetry to $SU(3)_L \otimes SU(3)_R \otimes U(1)_V$.

The $SU(3)_L \otimes SU(3)_R$ symmetry is spontaneously broken to $SU(3)_V$ by the appearance of a non-vanishing quark condensate $\langle\bar{\psi}_i\psi_i\rangle$, and, to a small degree, explicitly broken by the mass term $\mathcal{L}_{mass}$. Furthermore, the $SU(3)_V$ symmetry is broken by non-degenerate quark masses ($m_s > m_{u,d}$).

3.2 Mean-field approximation

In this section, we calculate the thermodynamic potential of the NJL model in the Mean-Field Approximation (MFA). An operator in the MFA is assumed to have small deviations from its thermal average. The $\mathcal{L}_4$ term contains four-fermion interaction terms $(\bar{q}\Gamma q)^2$, where $\Gamma = 1, i\gamma_5$. The MFA consists in expanding the Lagrangian to first-order in $(\bar{q}\Gamma q)$, around the thermal average $\langle\bar{q}\Gamma q\rangle$,

$$\begin{aligned}
(\bar{q}\Gamma q)^2 &= (\bar{q}\Gamma q + \langle\bar{q}\Gamma q\rangle - \langle\bar{q}\Gamma q\rangle)^2 \\
&= (\langle\bar{q}\Gamma q\rangle + \delta\langle\bar{q}\Gamma q\rangle)^2 \\
&= \langle\bar{q}\Gamma q\rangle^2 + (\delta\langle\bar{q}\Gamma q\rangle)^2 + 2\langle\bar{q}\Gamma q\rangle\delta\langle\bar{q}\Gamma q\rangle \\
&\approx \langle\bar{q}\Gamma q\rangle^2 + 2\langle\bar{q}\Gamma q\rangle\delta\langle\bar{q}\Gamma q\rangle \\
&= \langle\bar{q}\Gamma q\rangle^2 + 2\langle\bar{q}\Gamma q\rangle(\bar{q}\Gamma q) - 2\langle\bar{q}\Gamma q\rangle^2 \\
&= 2\langle\bar{q}\Gamma q\rangle(\bar{q}\Gamma q) - \langle\bar{q}\Gamma q\rangle^2,
\end{aligned} \tag{3.5}$$

where the deviation from thermal average $\delta\langle\bar{q}\Gamma q\rangle = \bar{q}\Gamma q - \langle\bar{q}\Gamma q\rangle$ is assumed to be small, and as a first-order approximation we ignore higher-order fluctuations $(\delta\langle\bar{q}\Gamma q\rangle)^2$. We assume that the condensates $\langle\bar{q}i\gamma_5\lambda^a q\rangle$ are zero in the homogeneous ground state. Using the explicit form of the gamma matrices (see Appendix A) the flavor-mixing terms, i.e., $\langle\bar{q}_i q_j\rangle$ with $i \neq j$, that appear in

$$\sum_{a=0}^{8}(\bar{q}\lambda^a q),$$

for $a = 1, 2, 4, 5, 6, 7$, are also ignored since they violate flavor conservation. Thus, keeping only the flavor conservation terms we obtain

$$\sum_{a=0,3,8}(\bar{q}\lambda^a q) = (\bar{q}\lambda^0 q) + (\bar{q}\lambda^3 q) + (\bar{q}\lambda^8 q) = 2\left((\bar{q}_u q_u)^2 + (\bar{q}_d q_d)^2 + (\bar{q}_s q_s)^2\right). \tag{3.6}$$

Therefore, the $\mathcal{L}_4$ term in the MFA becomes

$$\mathcal{L}_4^{MFA} = -G_s^0\sum_i\langle\bar{q}_i q_i\rangle^2 + 2G_s^0(\bar{q}_u q_u)\langle\bar{q}_u q_u\rangle + 2G_s^0(\bar{q}_d q_d)\langle\bar{q}_d q_d\rangle + 2G_s^0(\bar{q}_s q_s)\langle\bar{q}_s q_s\rangle. \tag{3.7}$$

The MFA of a six-fermion interaction term is

$$\begin{aligned}\mathcal{O}_1\mathcal{O}_2\mathcal{O}_3 &\approx \langle\mathcal{O}_1\rangle\langle\mathcal{O}_2\rangle\langle\mathcal{O}_3\rangle + ((\mathcal{O}_1 - \langle\mathcal{O}_1\rangle)\langle\mathcal{O}_2\rangle\langle\mathcal{O}_3\rangle + \text{cyclic permutations})\\ &= \mathcal{O}_1\langle\mathcal{O}_2\rangle\langle\mathcal{O}_3\rangle + \langle\mathcal{O}_1\rangle\mathcal{O}_2\langle\mathcal{O}_3\rangle + \langle\mathcal{O}_1\rangle\langle\mathcal{O}_2\rangle\mathcal{O}_3 - 2\langle\mathcal{O}_1\rangle\langle\mathcal{O}_2\rangle\langle\mathcal{O}_3\rangle.\end{aligned} \tag{3.8}$$

Thus, the 't Hooft term $\mathcal{L}_6$ in the MFA is given by

$$\begin{aligned}\det{}_f(\bar{q}_f\mathcal{O}q_f) &= \sum_{i,j,k}\epsilon_{ijk}(\bar{q}_u\mathcal{O}q_i)(\bar{q}_d\mathcal{O}q_j)(\bar{q}_s\mathcal{O}q_k)\\ &\approx \sum_{i,j,k}[(\bar{q}_u\mathcal{O}q_i)\langle\bar{q}_d\mathcal{O}q_j\rangle\langle\bar{q}_s\mathcal{O}q_k\rangle + \langle\bar{q}_u\mathcal{O}q_i\rangle(\bar{q}_d\mathcal{O}q_j)\langle\bar{q}_s\mathcal{O}q_k\rangle\\ &\qquad + \langle\bar{q}_u\mathcal{O}q_i\rangle\langle\bar{q}_d\mathcal{O}q_j\rangle(\bar{q}_s\mathcal{O}q_k) - 2\langle\bar{q}_u\mathcal{O}q_i\rangle\langle\bar{q}_d\mathcal{O}q_j\rangle\langle\bar{q}_s\mathcal{O}q_k\rangle].\end{aligned} \tag{3.9}$$

Inserting the operator $\mathcal{O} = 1 \pm \gamma_5$ and using both the flavor conservation, $\langle\bar{q}_i q_j\rangle = 0$ for $i \neq j$, and $\langle\bar{q}_i\gamma_5 q_j\rangle = 0$, we get

$$\begin{aligned}\mathcal{L}_6^{MFA} &= 2K(\bar{q}_u q_u)\langle\bar{q}_d q_d\rangle\langle\bar{q}_s q_s\rangle + 2K(\bar{q}_d q_d)\langle\bar{q}_u q_u\rangle\langle\bar{q}_s q_s\rangle + 2K(\bar{q}_s q_s)\langle\bar{q}_u q_u\rangle\langle\bar{q}_d q_d\rangle\\ &\quad - 4K\langle\bar{q}_u q_u\rangle\langle\bar{q}_d q_d\rangle\langle\bar{q}_s q_s\rangle.\end{aligned} \tag{3.10}$$

Gathering all the contributions, we obtain the Lagrangian of the NJL model in the MFA

$$\mathcal{L}_{NJL}^{MFA} = \bar{q}(i\gamma^\mu\partial_\mu - \hat{M})q - G_s^0\sum_i\langle\bar{q}_i q_i\rangle^2 - 4K\langle\bar{q}_u q_u\rangle\langle\bar{q}_d q_d\rangle\langle\bar{q}_s q_s\rangle, \tag{3.11}$$

with $\hat{M} = \mathrm{diag}(M_u, M_d, M_s)$, where M_i are the constituent quark masses given by the gap equations

$$\begin{cases} M_u &= m_u - 2G_s^0\langle\bar{q}_u q_u\rangle - 2K\langle\bar{q}_d q_d\rangle\langle\bar{q}_s q_s\rangle \\ M_d &= m_d - 2G_s^0\langle\bar{q}_d q_d\rangle - 2K\langle\bar{q}_s q_s\rangle\langle\bar{q}_u q_u\rangle \\ M_s &= m_s - 2G_s^0\langle\bar{q}_s q_s\rangle - 2K\langle\bar{q}_u q_u\rangle\langle\bar{q}_d q_d\rangle. \end{cases} \tag{3.12}$$

We call M_i the constituent quark masses to distinguish them from the current quark masses m_i that appear in the Lagrangian. The constituent quark masses are effective masses generated by the spontaneous breaking of chiral symmetry. In this case, we speak of the spontaneous generation of an effective quark mass.

3.2.1 Thermodynamic potential

In thermal field theory the partition function of the grand-canonical ensemble is given by

$$\mathcal{Z}(\beta,\mu) \equiv \mathrm{Tr}\left(e^{-\beta(H-\mu\hat{N})}\right) = \sum_i \int d\Psi_i \langle\Psi_i|e^{-\beta(H-\mu\hat{N})}|\Psi_i\rangle, \tag{3.13}$$

where $\beta = 1/T$ is the inverse temperature, H is the system Hamiltonian, μ is the chemical potential, and $\hat{N}$ is the baryon number operator.

A possible approach to thermal field theory is the path integral formalism [173–175]. The path integral may be defined in imaginary time, being more convenient to study finite temperature systems. We need to perform an analytical continuation from real to imaginary time (called Wick rotation) $t \to -i\tau$ with $\tau \in \mathbb{R}$. The partition function in Euclidean time τ is given by

$$\mathcal{Z}(\beta,\mu) = \mathcal{N}\int \mathcal{D}q^\dagger \mathcal{D}q e^{S_E}, \tag{3.14}$$

where S_E is the Euclidean action,

$$S_E = \int_0^\beta d\tau \int d^3x(\mathcal{L}_E - \mu\hat{N}). \tag{3.15}$$

Once the partition function $\mathcal{Z}(\beta,\mu)$ is obtained, the thermodynamic potential can be calculated by

$$\Omega(\beta,\mu) = -\frac{1}{\beta V}\ln\mathcal{Z}(\beta,\mu). \tag{3.16}$$

Transforming the NJL Lagrangian in the MFA (Eq. (3.11)) into imaginary time, allows us to write the Euclidean action in the MFA as

$$S_{NJL} = \int_0^\beta d\tau \int d^3x \bar{q}S_0^{-1}q + \beta V U, \tag{3.17}$$

where

$$S_0^{-1} = -\gamma^0 \frac{\partial}{\partial \tau} + i\gamma.\nabla - M + \mu\gamma^0 \tag{3.18}$$

is the inverse fermionic propagator, and U is given by

$$U = -G_s^0 \sum_i \langle \bar{q}_i q_i \rangle^2 - 4K \langle \bar{q}_u q_u \rangle \langle \bar{q}_d q_d \rangle \langle \bar{q}_s q_s \rangle. \tag{3.19}$$

Then, the thermodynamic potential can be written as

$$\Omega(\beta, \mu) = -\frac{1}{\beta V} \ln \mathcal{Z}_0 - U, \tag{3.20}$$

where the partition function $\mathcal{Z}_0$ is

$$\mathcal{Z}_0 = \int \mathcal{D}q^\dagger \mathcal{D}q \exp\left(\int_0^\beta d\tau \int d^3x \bar{q} S_0^{-1} q \right). \tag{3.21}$$

Instead of working in the $(\mathbf{x}, \tau)$ space, we can move to the momentum-frequency space $(\mathbf{p}, i\omega_n)$ expanding the fermionic field $q(\mathbf{x}, \tau)$ in Fourier series,

$$q_\alpha(\mathbf{x}, \tau) = \frac{1}{\sqrt{V}} \sum_{\mathbf{p}, n} e^{i(\mathbf{p}.\mathbf{x} + \omega_n \tau)} q_{\alpha, n}(\mathbf{p}). \tag{3.22}$$

Due to the anti-periodic boundary conditions of the fermionic fields, $q(\mathbf{x}, 0) = -q(\mathbf{x}, \beta)$, only odd frequencies (called Matsubara frequencies) are allowed: $\omega_n = (2n+1)\pi T$.

The action S_0, in the partition function $\mathcal{Z}_0$ of Eq. (3.21), becomes

$$\begin{aligned} S_0 = \int_0^\beta d\tau \int d^3x \bar{q} S_0^{-1} q &= \beta \sum_{\mathbf{p}, n} \bar{q}_{\alpha n}(\mathbf{p}) \left[-i\gamma^0 \omega_n - \gamma.\mathbf{p} - M + \mu\gamma^0 \right] q_{\alpha' n}(\mathbf{p}) \\ &= \sum_{\mathbf{p}, n} q^\dagger_{\alpha n}(\mathbf{p}) D_{\alpha\alpha'}(\mathbf{p}) q_{\alpha' n}(\mathbf{p}), \end{aligned} \tag{3.23}$$

with

$$D_{\alpha\alpha'}(\mathbf{p}) = \beta\gamma^0 \left[-i\gamma^0 \omega_n - \gamma.\mathbf{p} - M + \mu\gamma^0 \right]. \tag{3.24}$$

The $\mathcal{Z}_0$ [Eq. (3.21)] is now a Gaussian integral over Grassman fields,

$$\int \prod_\alpha dq^\dagger_{\alpha n}(\mathbf{p}) dq_{\alpha n}(\mathbf{p}) \exp\left(\sum_{\mathbf{p}, n} q^\dagger_{\alpha n}(\mathbf{p}) D_{\alpha\alpha'}(\mathbf{p}) q_{\alpha' n}(\mathbf{p}) \right). \tag{3.25}$$

Using the identity

$$\int \prod_i^N dq_i^\dagger dq_i \exp\left(q^\dagger D q \right) = \det D, \tag{3.26}$$

and $\ln\det D = \mathrm{Tr}\ln D$, we get

$$\Omega(\beta,\mu) = -\frac{1}{\beta V}\,\mathrm{Tr}\ln\left[\beta S^{-1}(\mathbf{p},\omega_n)\right] - U, \tag{3.27}$$

where the trace is in flavor, color, Dirac, and also in momentum-frequency $(i\omega_n, \mathbf{p})$ spaces. The inverse quark propagator $S^{-1}(\mathbf{p},\omega_n)$ is given by

$$S^{-1}(\mathbf{p},\omega_n) = \left[-i\omega_n - \gamma^0\gamma.\mathbf{p} - \gamma^0 M + \mu\right]. \tag{3.28}$$

Calculating the trace

$$\begin{aligned}\mathrm{Tr}\ln\left[\beta S^{-1}(\mathbf{p},\omega_n)\right] &= \sum_n\sum_{\mathbf{p}}\mathrm{Tr}_{\text{color}}\,\mathrm{Tr}_{\text{flavor}}\,\mathrm{Tr}_{\text{Dirac}}\ln\left[\beta S^{-1}(\mathbf{p},\omega_n)\right]\\ &= V\,\mathrm{Tr}_{\text{color}}\,\mathrm{Tr}_{\text{flavor}}\,\mathrm{Tr}_{\text{Dirac}}\int\frac{d^3p}{(2\pi)^3}\sum_n\ln\left[\beta S^{-1}(\mathbf{p},\omega_n)\right].\end{aligned} \tag{3.29}$$

The sum over the Matsubara frequencies n can be calculated as follows (only the main steps are shown, for a detailed calculation see [173]):

$$\begin{aligned}\sum_n\mathrm{Tr}_{\text{Dirac}}\ln\left[\beta S^{-1}(\mathbf{p},\omega_n)\right] &= 2\sum_n\ln\left\{\beta^2\left[(\omega_n+i\mu)^2+\omega^2\right]\right\}\\ &= \sum_n\left\{\ln\left[\beta^2(\omega_n^2(\omega-\mu)^2)\right]+\ln\left[\beta^2(\omega_n^2(\omega+\mu)^2)\right]\right\}\\ &= 2\left[\beta\omega+\ln(1+e^{-\beta(\omega-\mu)})+\ln(1+e^{-\beta(\omega+\mu)})\right],\end{aligned} \tag{3.30}$$

with $\omega = \sqrt{\mathbf{p}^2+M^2}$. Therefore, we have

$$\mathrm{Tr}\ln\left[\beta S^{-1}(\mathbf{p},\omega_n)\right] = 2VN_c\sum_{i=u,d,s}\int\frac{d^3p}{(2\pi)^3}\left[\beta\omega_i+\ln(1+e^{-\beta(\omega_i-\mu)})+\ln(1+e^{-\beta(\omega_i+\mu)})\right]. \tag{3.31}$$

with $\omega_i = \sqrt{\mathbf{p}_i^2+M_i^2}$. Finally, we can write down the thermodynamic potential of the three-flavor NJL model in the MFA,

$$\begin{aligned}\Omega(T,\mu) = &-2N_c\sum_{i=u,d,s}\int\frac{d^3p}{(2\pi)^3}\left[\omega_i+T\ln(1+e^{-\beta(\omega_i-\mu)})+T\ln(1+e^{-\beta(\omega_i+\mu)})\right]\\ &+G_s^0\sum_i\langle\bar{q}_iq_i\rangle^2+4K\langle\bar{q}_uq_u\rangle\langle\bar{q}_dq_d\rangle\langle\bar{q}_sq_s\rangle,\end{aligned} \tag{3.32}$$

where the constituent masses M_i are given by the gap equations [Eq. (3.12)].

As a first step of the MFA, we have expanded the Lagrangian terms $(\bar{q}\Gamma q)^2$ around their thermal average $\langle\bar{q}\Gamma q\rangle^2$, where second-order fluctuations were ignored.

The thermal average fields $\langle \bar{q}_i q_i \rangle = \phi_i$ are called quark condensates ($\Gamma = 1$). The second step was to consider the quark condensates as constant fields in space-time, which has allowed us to make the following step

$$S_E = \int_0^\beta d\tau \int d^3x U(\phi_i) = \beta V U(\phi_i). \tag{3.33}$$

The last step of the MFA is to assume that the ϕ_i field takes the classical value $\bar{\phi}_i$, which is the value that minimizes the action, i.e., the $\bar{\phi}_i$ configuration that makes e^{-S_E} maximum, contributing considerably to the partition function $\mathcal{Z} \sim \int d\bar{\phi} e^{-S_E}$. Therefore, the condensate values $\langle \bar{q}_i q_i \rangle = \phi_i$ can be calculated from

$$\left.\frac{\delta S_E}{\delta \phi_i}\right|_{\phi_i = \bar{\phi}_i} = 0 \qquad \Longrightarrow \qquad \left.\frac{\delta \Omega}{\delta \phi_i}\right|_{\phi_i = \bar{\phi}_i} = 0. \tag{3.34}$$

The quark condensates $\bar{\phi}_i = \langle \bar{q}_i q_i \rangle$ are then given by

$$\langle \bar{q}_i q_i \rangle \; = \; - \, 2N_c \int \frac{\mathrm{d}^3 p}{(2\pi)^3} \frac{M_i}{\omega_i} [\theta(\Lambda^2 - \mathbf{p}_i^2) - f(\omega_i - \mu) - \bar{f}(\omega_i + \mu)], \tag{3.35}$$

where $f(\omega_i - \mu)$ $\left(\bar{f}(\omega_i + \mu)\right)$ is the Fermi distribution function for fermions (anti-fermions).

The gap equations of the NJL model can also be calculated using the bosonization formalism [167, 176]. Bosonization refers to the transformation in which the Lagrangian quark bilinear forms are replaced by auxiliary variables, used to integrate out the quark fields. The bosonization is performed using the Hubbard-Stratonovich transformations, where the fermionic degrees of freedom are replaced by effective bosonic degrees of freedom. A brief review of the bosonization procedure is given in Appendix B.

To fix the model, we need to calculate the pseudoscalar meson masses. There are several approaches to calculate them, one way is using the mesonic correlators. Correlation functions are thermal expectation values of time-ordered products of operators, and their poles correspond to on-shell masses of mesons and baryons. Correlation functions are calculated by expanding the effective action to second-order around the stationary points [176]. Therefore, the meson spectra are obtained as fluctuation corrections to the mean field approximation. The basic idea is to expand the thermodynamic potential around its mean field limit. There are several methods to examine these fluctuation corrections [167–169].

3.3 Model parametrization

Being the NJL model non-renormalizable, a regularization procedure must be applied in order to deal with divergent quantities. There is no unique way to regularize the model and several regularization schemes exist [168]. In this work we use the three-momentum non-covariant cutoff scheme, where a cutoff $p^2 < \Lambda^2$ is imposed on all divergent integrals only. Thus, we introduced a cutoff Λ in the UV divergence term $\int d^3p\sqrt{\mathbf{p_i}^2 + M_i^2}$ of the thermodynamic potential [Eq. (3.32)]. The cutoff is one characteristic length scale for the interaction assumed to be much larger than all relevant momenta.

The three-flavor NJL model has five free parameters: the current quark masses m_u, m_d, and m_s, the four-fermion coupling strength G_s^0, the six-fermion coupling strength K, and the cutoff Λ. These free parameters are fixed in vacuum ($T = \mu = 0$) in order to reproduce experimental data or LQCD results. There are several parametrization sets in the literature [169, 177, 178]. In this work we use the parametrization set of [178], shown in Table 3.1, in which the current light quark masses $m_u = m_d$ were set to 5.5 MeV, and the remaining four parameters were fitted to reproduce: the pion mass M_π, its decay constant f_π, the mass of the kaon meson M_K, and the mass of the η' meson $M_{\eta'}$.

Parameter set [178]	Physical quantities (MeV)	Predictions (MeV)
$m_u = m_d = 5.5$ MeV	$f_\pi = 92.4$	$M_\sigma = 728.8$
$m_s = 140.7$ MeV	$M_\pi = 135.0$	$M_\eta = 514.8$
$\Lambda = 602.3$ MeV	$M_K = 497.7$	$M_u = M_d = 367.7$
$G_s^0\Lambda^2 = 3.67$	$M_{\eta'} = 960.8$	$M_s = 549.5$
$K\Lambda^5 = -12.36$		$\lvert\langle\bar{\psi}_{u,d}\psi_{u,d}\rangle\rvert^{1/3} = -241.9$
		$\lvert\langle\bar{\psi}_s\psi_s\rangle\rvert^{1/3} = -257.7$

Table 3.1: The parameters values of the model, the respective physical quantities used on their fixing, and some predicted physical quantities.

3.4 Polyakov extended NJL model

Unlike the QCD, the NJL model is not invariant under a local $SU(3)$ transformation, but only under a global transformation. Therefore, the NJL model has no confinement mechanism as QCD. The deconfinement feature is taken into account in the NJL model by introducing an effective gluon potential in terms of the Polyakov loop in the Lagrangian [179–185]. The coupling of the quarks to the Polyakov loop leads to the reduction of the weight of the quark degrees of freedom at low temperature, as a consequence of the restoration of the center symmetry associated with the confinement.

3.4.1 Polyakov loop potential

In Section 2.2.3, we have introduced the expectation value of the Polyakov loop $\langle\Phi(\mathbf{x})\rangle$,

$$\Phi \equiv \langle\Phi(\mathbf{x})\rangle = \left\langle \frac{1}{3}\,\mathrm{Tr}_c\left[L(\mathbf{x})\right]\right\rangle \quad \text{with} \quad L(\mathbf{x}) = \mathcal{P}\exp\left\{ i\int_0^\beta d\tau A_4(\mathbf{x},\tau)\right\}, \tag{3.36}$$

as an order parameter for confinement/deconfinement phase transition in pure gauge theory. Hereafter, for simplicity, instead of calling expectation value of the Polyakov loop to Φ, we just call it Polyakov loop.

The order parameter Φ that probes the state of the $\mathbb{Z}_3$ symmetry is obtained by defining an effective Polyakov loop potential $\mathcal{U}(\Phi,\bar{\Phi})$ that respect all symmetries and reproduce lattice results from pure gauge theory. The values of Φ and $\bar{\Phi}$ are the ones which minimize the effective potential. The effective potential should be invariant under $U(1)$ symmetry, and include the center symmetry and its spontaneous breaking at high temperatures, in a deconfined phase. It must describe not only a first-order phase transition (for $N_c = 3$), but also reproduce thermodynamic lattice data of pure gauge theory.

There are several effective potentials available in the literature [186–189]. In this work we use the logarithm potential [187]:

$$\frac{\mathcal{U}\left(\Phi,\bar{\Phi};T\right)}{T^4} = -\frac{a\left(T\right)}{2}\bar{\Phi}\Phi + b(T)\ln\left[1-6\bar{\Phi}\Phi+4(\bar{\Phi}^3+\Phi^3)-3(\bar{\Phi}\Phi)^2\right], \tag{3.37}$$

where

$$a\left(T\right) = a_0 + a_1\left(\frac{T_0}{T}\right) + a_2\left(\frac{T_0}{T}\right)^2 \quad \text{and} \quad b(T) = b_3\left(\frac{T_0}{T}\right)^3$$

are temperature-dependent coefficients. The logarithmic dependence limits the Polyakov values to be always smaller than 1. The value $\Phi,\bar{\Phi} \to 1$ is only obtained in the asymptotically limit $T\to\infty$. The parameters were fitted to reproduce thermodynamical lattice results in pure gauge: $a_0 = 3.51$, $a_1 = -2.47$, $a_2 = 15.2$, and $b_3 = -1.75$. The parameter T_0 is the critical temperature for the deconfinement phase transition in pure gauge and is fixed to 270 MeV, according to lattice results.

We show in Fig. 3.1 the effective potential as a function of Φ (at zero baryonic chemical potential we have $\Phi = \bar{\Phi}$) for several temperatures (left), and the minimum of the effective potential as a function of temperature in MeV (right). For $T < T_0$, the effective potential has only one minimum at $\Phi = 0$, describing a confined phase. At $T = T_0$, the $\mathcal{U}$ shows two minimum at $\Phi = 0$ and $\Phi \approx 0.48$ with the same height, describing a first-order phase transition from a confined to a deconfined phase. For $T > T_0$, the effective potential has one minimum at a finite Φ value (deconfined phase).

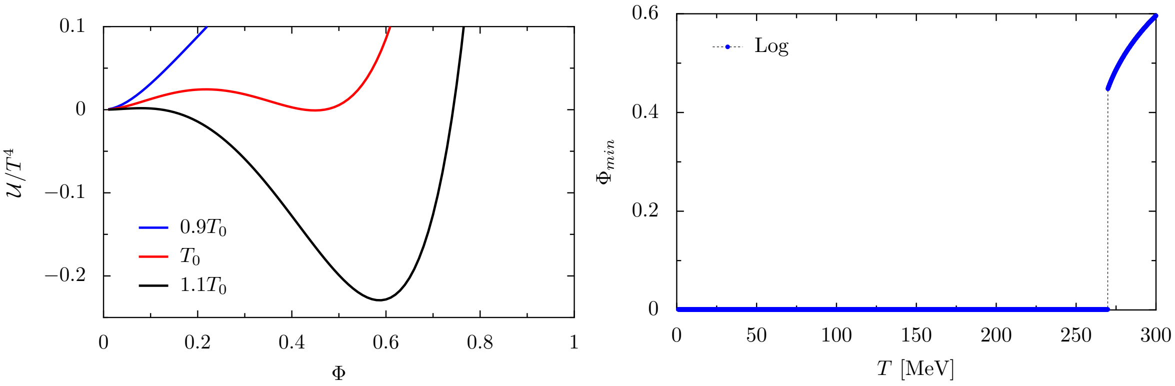

Figure 3.1: Effective potential $\mathcal{U}/T^4$ [Eq. (3.37)] as a function of Φ for several temperatures (left), and its minimum as a function of temperature in MeV (right).

The parameter T_0 is the only free parameter of the effective potential and its value reproduces the first-order phase transition of pure gauge system. When one introduces the effective potential in the NJL, we want that the pseudocritical temperature of the deconfined transition agrees with LQCD results, which for $2+1$-flavors with physical quark masses is $T_c^{\Phi} = 170(4)(3)$ MeV [25], where the first error comes from the statistical errors whereas the second error arises from the accuracy of the scale determination. Thus, a rescale of T_0 to $210\,\mathrm{MeV}$ is needed in order to reproduce this T_c^{Φ} LQCD result.

Let us stress that the Polyakov loop effective potential does not have any dynamical degrees of freedom. Instead, it only describes a constant gauge field background in which quarks propagate. Anyway, the potential was fitted in order to mimic the pressure term, $p_{glue}(T) = -\mathcal{U}(\Phi_{\text{min}}(T);T)$, of the gluonic degrees of freedom, reproducing the right Stefan-Boltzmann limit for $T \to \infty$.

Transverse gluons, which are thermodynamically relevant degrees of freedom at high temperatures ($T > 2.5T_c$), are not taken into account in the PNJL model. Thus, the range of applicability of the PNJL model is $T \leq (2-3)T_c$ [190].

3.4.2 Coupling between quarks and the Polyakov loop

The coupling between quarks and gluon fields is accomplished via the covariant derivative,

$$D_\mu = \partial_\mu - iA^\mu. \tag{3.38}$$

Once the spatial fluctuations of the Polyakov loop are ignored, only the time component of the gluon needs to be considered, $A^\mu = \delta^\mu_0 A_0$ (Polyakov gauge); in Euclidean notation $A_0 = -iA_4$. Being the time component A_4 a constant field, the Polyakov loop operator becomes trivial,

$$L(\mathbf{x}) = \mathcal{P}\exp\left\{i\int_0^\beta d\tau A_4\right\} = e^{i\beta A_4} \tag{3.39}$$

$$L^\dagger(\mathbf{x}) = \mathcal{P}\exp\left\{-i\int_0^\beta d\tau A_4\right\} = e^{-i\beta A_4}. \tag{3.40}$$

Furthermore, six of the eight components of A_μ do not contain any physical information. The Polyakov loop operator can be parametrized, in the Polyakov gauge, only using two parameters [182]

$$L = \begin{pmatrix} e^{i\phi} & 0 & 0 \\ 0 & e^{i\phi'} & 0 \\ 0 & 0 & e^{-i(\phi+\phi')} \end{pmatrix}. \tag{3.41}$$

With this *ansatz*, the Polyakov loop $\Phi = \frac{1}{3}\,\mathrm{Tr}_c\, L$ and its conjugate are given by

$$\Phi = \frac{1}{3}\left(e^{i\phi} + e^{i\phi'} + e^{-i(\phi+\phi')}\right) \tag{3.42}$$

$$\bar{\Phi} = \frac{1}{3}\left(e^{-i\phi} + e^{-i\phi'} + e^{i(\phi+\phi')}\right). \tag{3.43}$$

3.4.3 Gap equations

The quark propagator in a constant background field A_4 is now

$$S_i(p) = -(\not{p} - M_i + \gamma_0(\mu - iA_4))^{-1}, \tag{3.44}$$

where $p_0 = i\omega_n$, and $\omega_n = (2n+1)\pi T$ is the fermion Matsubara frequency.

The thermodynamic potential of the PNJL model can be obtained using the same techniques of Section 3.2, and is given by [185, 191]

$$\Omega(\Phi,\bar{\Phi},M_i;T,\mu) = \mathcal{U}\left(\Phi,\bar{\Phi},T\right) + g_S \sum_{i=u,d,s} \langle\bar{q}_i q_i\rangle^2 + 4K\langle\bar{q}_u q_u\rangle\langle\bar{q}_d q_d\rangle\langle\bar{q}_s q_s\rangle \tag{3.45}$$

$$- 2N_c \sum_{i=u,d,s}\int \frac{\mathrm{d}^3p}{(2\pi)^3}\left\{E_i + T\left(z^+_\Phi(E_i) + z^-_\Phi(E_i)\right)\right\}$$

where $E_i = \sqrt{\mathbf{p}^2 + M_i^2}$ is the quasi-particle energy for the quark i, and $z_\Phi^\pm$ are the partition function densities given by:

$$z_\Phi^+(E_i) \equiv \mathrm{Tr}_c \ln\left[1 + L^\dagger e^{-\beta E_p^-}\right] = \ln\left\{1 + 3\left(\bar{\Phi} + \Phi e^{-\beta E_p^-}\right) e^{-\beta E_p^-} + e^{-3\beta E_p^-}\right\} \tag{3.46}$$

$$z_\Phi^-(E_i) \equiv \mathrm{Tr}_c \ln\left[1 + L e^{-\beta E_p^+}\right] = \ln\left\{1 + 3\left(\Phi + \bar{\Phi} e^{-\beta E_p^+}\right) e^{-\beta E_p^+} + e^{-3\beta E_p^+}\right\}, \tag{3.47}$$

where $E_i^{(\pm)} = E_i \mp \mu$, the upper sign applying for fermions and the lower sign for anti-fermions. The explicit diagonal form of the Polyakov line Eq. (3.41) and its color traces, Eqs. (3.42) and (3.42), were used.

We obtain the gap equations by minimizing the thermodynamic potential [Eq. (3.45)] with respect to the order parameters $(M_u, M_d, M_s, \Phi, \bar{\Phi})$. The quark gap equations are the same as in the NJL [Eq. (3.12)]:

$$\begin{cases} M_u = m_u - 2G_s^0\langle\bar{q}_u q_u\rangle - 2K\langle\bar{q}_d q_d\rangle\langle\bar{q}_s q_s\rangle \\ M_d = m_d - 2G_s^0\langle\bar{q}_d q_d\rangle - 2K\langle\bar{q}_s q_s\rangle\langle\bar{q}_u q_u\rangle \\ M_s = m_s - 2G_s^0\langle\bar{q}_s q_s\rangle - 2K\langle\bar{q}_u q_u\rangle\langle\bar{q}_d q_d\rangle . \end{cases}$$

The quark condensates $\langle\bar{q}_i q_i\rangle$ are modified by the constant background field A_4, and are given by

$$\langle\bar{q}_i q_i\rangle \;=\; -\;2N_c \int \frac{\mathrm{d}^3p}{(2\pi)^3}\frac{M_i}{E_i}[\theta(\Lambda^2 - \mathbf{p}^2) - f_\Phi^{(+)}(E_i) - f_\Phi^{(-)}(E_i)], \tag{3.48}$$

where the modified distribution functions are

$$f_\Phi^{(+)}(E_i) = \frac{\bar{\Phi} e^{-\beta E_p^-} + 2\Phi e^{-2\beta E_p^-} + e^{-3\beta E_p^-}}{1 + 3\left(\bar{\Phi} + \Phi e^{-\beta E_p^-}\right) e^{-\beta E_p^-} + e^{-3\beta E_p^-}} \tag{3.49}$$

$$f_\Phi^{(-)}(E_i) = \frac{\Phi e^{-\beta E_p^+} + 2\bar{\Phi} e^{-2\beta E_p^+} + e^{-3\beta E_p^+}}{1 + 3\left(\Phi + \bar{\Phi} e^{-\beta E_p^+}\right) e^{-\beta E_p^+} + e^{-3\beta E_p^+}}. \tag{3.50}$$

Looking at the above modified distribution functions $f_\Phi^{(\pm)}(E_i)$ we see that as we approach $\phi, \bar{\phi} \to 0$ ("confined phase") the Boltzmann 3-particle contributions dominates. In the opposite limit, for $\phi, \bar{\phi} \to 1$ ("deconfined phase"), all 1-, 2- and 3-particle Boltzmann contributions are present. In the PNJL model the coupling of quarks to the Polyakov loop produces a statistical suppression of the one- and two-quark contributions to the thermodynamics and thus an improvement of the NJL model results at low temperatures [185].

The Polyakov loop values are the ones that minimize the thermodynamic potential,

$$\frac{\partial\mathcal{U}}{\partial\Phi} = 0 \qquad \text{and} \qquad \frac{\partial\mathcal{U}}{\partial\bar{\Phi}} = 0, \tag{3.51}$$

and we obtain the following gap equations,

$$\begin{aligned}0 = T^4 &\left\{ -\frac{a(T)}{2}\bar{\Phi} - 6\frac{b(T)\left[\bar{\Phi} - 2\Phi^2 + \bar{\Phi}^2\Phi\right]}{1 - 6\bar{\Phi}\Phi + 4(\bar{\Phi}^3 + \Phi^3) - 3(\bar{\Phi}\Phi)^2} \right\} \\ &- 6T\sum_{i=u,d,s}\int\frac{\mathrm{d}^3p}{(2\pi)^3}\left(\frac{e^{-2\beta\,E_p^-}}{\exp\{z_\Phi^+(E_i)\}} + \frac{e^{-\beta\,E_p^+}}{\exp\{z_\Phi^-(E_i)\}}\right)\end{aligned} \tag{3.52}$$

$$\begin{aligned}0 = T^4 &\left\{ -\frac{a(T)}{2}\Phi - 6\frac{b(T)\left[\Phi - 2\bar{\Phi}^2 + \bar{\Phi}\Phi^2\right]}{1 - 6\bar{\Phi}\Phi + 4(\bar{\Phi}^3 + \Phi^3) - 3(\bar{\Phi}\Phi)^2} \right\} \\ &- 6T\sum_{i=u,d,s}\int\frac{\mathrm{d}^3p}{(2\pi)^3}\left(\frac{e^{-\beta\,E_p^-}}{\exp\{z_\Phi^+(E_i)\}} + \frac{e^{-2\beta\,E_p^+}}{\exp\{z_\Phi^-(E_i)\}}\right).\end{aligned} \tag{3.53}$$

In fact, the NJL model can be generalized to the PNJL model by introducing the modified Fermi-Dirac distribution functions [185]:

$$f(E_i - \mu) \to f_\Phi^{(+)}(E_i) = \frac{\bar{\Phi}e^{-\beta\,E_p^-} + 2\Phi e^{-2\beta\,E_p^-} + e^{-3\beta\,E_p^-}}{\exp\{z_\Phi^+(E_i)\}} \tag{3.54}$$

$$f(E_i - \mu) \to f_\Phi^{(-)}(E_i) = \frac{\Phi e^{-\beta\,E_p^+} + 2\bar{\Phi}e^{-2\beta\,E_p^+} + e^{-3\beta\,E_p^+}}{\exp\{z_\Phi^-(E_i)\}}. \tag{3.55}$$

3.5 Introduction of an external magnetic field

Let us now introduce a static and constant external magnetic field in the z direction

$$A^\mu_{EM} = \delta^{\mu 2}x_1 B. \tag{3.56}$$

In the PNJL model the coupling between the magnetic field B and quarks is implemented *via* the covariant derivative

$$D^\mu = \partial^\mu - iq_f A^\mu_{EM} - iA^\mu, \tag{3.57}$$

where q_f represents the f-quark electric charge ($q_d = q_s = -q_u/2 = -e/3$), and A^μ are the gluon fields [see Eq. (3.38)].

We obtain the modified fermion spectrum by solving the Dirac equation in a constant magnetic background B,

$$E_n(p_z) = \pm\sqrt{m^2 + p_z^2 + 2|q_f B|n}, \tag{3.58}$$

where $n = 0, 1, 2, ...$ is the Landau Level index. The Landau level index contains both orbital, $k = 0, 1, 2, ...$, and spin, $s = \pm\frac{1}{2}$, contributions: $n = k - s\frac{q_f}{|q_f|} + \frac{1}{2}$. Therefore, we have

$$n = k + s + \frac{1}{2}, \qquad \text{for the down and strange quarks} \tag{3.59}$$

$$n = k - s + \frac{1}{2}, \qquad \text{for the up quark} \tag{3.60}$$

The Lowest Landau Level (LLL), $n = 0$, can only accommodate quarks with a zero orbital quantum number ($k = 0$) and with a spin quantum number of $s = -\frac{1}{2}$ for the strange and down quarks, and $s = \frac{1}{2}$ for the up quark. The LLL is a spin polarized state. The Higher Landau Levels (HLL), $n > 0$, have a two-fold degeneracy. Moreover, there is a infinite degeneracy for each Landau Level and for a fixed value of p_z, which is related to the p_y momentum value. The density of states is $\frac{|eB|}{2\pi}$ for $n = 0$, and $\frac{|eB|}{\pi}$ for $n > 0$ [192]. The integrals, in the magnetic field presence, are then modified as

$$\int \frac{d^3p}{(2\pi)^3} f(E) \rightarrow \frac{|qB|}{2\pi} \sum_n \alpha_n \int_0^{+\infty} \frac{dp_z}{2\pi} f(E_n),$$

where $\alpha_n = 2 - \delta_{n0}$, being 1 for the $n = 0$ (LLL) and 2 otherwise (HLL).

The thermodynamical potential Ω in the presence of a magnetic field can be separated into three terms: one B independent Ω_{vac} (vacuum contribution), one B dependent Ω_{mag} (magnetic contribution), and a term Ω_{med} (medium contribution) that depends on B, chemical potential, and temperature [70–72]. They are given by

$$\Omega^i_{\text{vac}} = -6 \int_\Lambda \frac{d^3p_i}{(2\pi)^3} E_i \tag{3.61}$$

$$\Omega^i_{\text{med}} = -T \frac{|q_i B|}{2\pi} \sum_{n=0}^{\infty} \alpha_n \int_{-\infty}^{+\infty} \frac{dp^i_z}{2\pi} \left(z^+_\Phi(E^n_i) + z^-_\Phi(E^n_i) \right) \tag{3.62}$$

$$\Omega^i_{\text{mag}} = -\frac{3(|q_i|B)^2}{2\pi^2} \left[\zeta'(-1, x_i) - \frac{1}{2}(x_i^2 - x_i) \ln x_i + \frac{x_i^2}{4} \right] \tag{3.63}$$

where $x_i = M_i^2/(2|q_i|B)$, $E_i = \sqrt{M_i^2 + p_i^2}$, $E^n_i = \sqrt{M_i^2 + (p^z_i)^2 + 2|q_f B|n}$, and $\zeta'(-1, x_i) = d\zeta(z, x_i)/dz|_{z=-1}$, being $\zeta(z, x_i)$ the Riemann-Hurwitz zeta function. The terms Ω^i_{vac} are regularized by the three-momentum UV cutoff Λ of the NJL model. The details of the regularization used are in [70], and a comparison with other model regularizations in [193]. The thermodynamic potential can be written as [70–72]

$$\begin{aligned} \Omega(T, \mu; B) = &\sum_{i=u,d,s} \left(\Omega^i_{\text{vac}} + \Omega^i_{\text{med}} + \Omega^i_{\text{mag}} \right) + G^0_s(\Phi, \bar{\Phi}) \sum_{i=u,d,s} \langle \bar{q}_i q_i \rangle^2 \\ &+ 4K \langle \bar{q}_u q_u \rangle \langle \bar{q}_d q_d \rangle \langle \bar{q}_s q_s \rangle + \mathcal{U}(\Phi, \bar{\Phi}, T). \end{aligned} \tag{3.64}$$

The quark condensate $\langle \bar{q}_i q_i \rangle$ can also be separated into three parts

$$\langle \bar{q}_i q_i \rangle = \langle \bar{q}_i q_i \rangle_{\text{vac}} + \langle \bar{q}_i q_i \rangle_{\text{mag}} + \langle \bar{q}_i q_i \rangle_{\text{med}},$$

which are given by [70–72]

$$\langle \bar{q}_i q_i \rangle_{\text{vac}} = -6 \int_\Lambda \frac{d^3p}{(2\pi)^3} \frac{M_i}{E_i} \tag{3.65}$$

$$\langle \bar{q}_i q_i \rangle_{\text{mag}} = -\frac{3 m_i |q_i| B}{2\pi^2} \left[\ln \Gamma(x_i) - \frac{1}{2} \ln(2\pi) + x_i - \frac{1}{2}(2x_i - 1) \ln(x_i) \right]$$

$$\langle \bar{q}_i q_i \rangle_{\text{med}} = \frac{3(|q_i|B)^2}{2\pi} \sum_n^\infty \alpha_n \int_{-\infty}^{+\infty} \frac{dp_z^i}{2\pi} \left(f_\Phi^{(+)}(E_i^n) + f_\Phi^{(-)}(E_i^n) \right). \tag{3.66}$$

Therefore, in the presence of the magnetic field, we must solve the gap equations [Eq. (3.12)] at any (T, μ), using the above definitions for the quark condensates $\langle \bar{q}_i q_i \rangle$, and then calculate the thermodynamic potential as a function of (T, μ). Thermal transitions can occur between any LL at finite temperature and n runs from 0 (LLL) to ∞ in the medium expressions. In our numerical calculations, we stopped at the LL which contributes only 10^{-8} to the net medium value.

3.6 Entanglement interaction

Due to the weak correlation between the chiral condensate and the Polyakov loop, the PNJL model cannot reproduce LQCD data at imaginary chemical potential. LQCD simulations are possible at imaginary μ (there is no sign problem). At imaginary chemical potential the thermodynamic potential of QCD has a Roberge-Weiss (RW) periodicity [194]. LQCD simulations show that at $\mu_q = i\theta_q T$ the order of the RW transition at the end point $T = T_E$ is of first-order for small and larger quark masses, but the order is weakened and could be second-order at intermediate masses [195, 196]. The entanglement interaction (EPNJL model) reproduces the quark-mass dependence of the RW end point predicted by LQCD [197]. An extension to the PNJL model was then proposed in [197]: a Φ dependence on the effective four-quark vertex G_s^0. The G_s^0 vertex of the NJL model can be seen as originated by one-gluon exchange diagram between two quarks and its higher-order diagrams. If the time component of gluon field A_ν has a finite expectation value $\langle A_0 \rangle$, which is related to Φ, then the G_s^0 is transformed into an effective vertex that depends on Φ [197]. This phenomenological effective vertex $G_s(\Phi)$ (entanglement interaction) generates a strong correlation between chiral and deconfinement phase transitions. Its functional form is determined by the invariance under extended $\mathbb{Z}_3$ symmetry, chiral symmetry, and its strength must reproduce LQCD data at complex μ [197–199].

One possible functional form of $G_s(\Phi,\bar{\Phi})$, which preserves chiral symmetry, C symmetry, and extended $\mathbb{Z}_3$ symmetry, is [197]

$$G_s(\Phi,\bar{\Phi}) = G_s^0\left[1-\alpha_1\Phi\bar{\Phi}-\alpha_2(\Phi^3+\bar{\Phi}^3))\right], \tag{3.67}$$

where α_1 and α_2 are free parameters.

The parametrization of the entanglement interaction, i.e., the (α_1,α_2) values, was performed for both 2-flavors [197] and 2+1-flavors [199]. For the 2+1-flavors case, using $T_0 = 150\,\mathrm{MeV}$, the domain of (α_1,α_2) satisfying

$$\{-1.5\alpha_1+0.3<\alpha_2<-0.86\alpha_1+0.32, \alpha_2>0\},$$

reproduces the chiral crossover of 2+1-flavors LQCD at $\mu=0$ [200], and the transition nature of the Roberge-Weiss end point at $\theta=\pi$ [196].

As we will see in the next Chapter, the PNJL model gives a pseudocritical temperature of deconfinement lower than the pseudocritical temperature of chiral transition. An opposite result is obtained in LQCD simulations, i.e., a higher pseudocritical deconfinement transition temperature is obtained. The introduction of the entanglement interaction (EPNJL model) reduces the gap between both pseudocritical temperatures of the PNJL, and thus goes in the right direction to reproduce LQCD results even though we cannot reproduce a pseudocritical deconfinement transition temperature higher than the pseudocritical chiral transition temperature.

Chapter 4

Hot quark matter under an external magnetic field

In this Chapter, we study how an external magnetic field affects three-flavor quark matter at zero baryonic chemical potential, using both PNJL and EPNJL models. Pseudocritical temperatures of chiral and deconfinement transitions are calculated. We determine how the entanglement interaction and its parametrization affect the chiral and deconfinement transitions and several thermodynamical quantities.

The last section is devoted to the study of the strange quark chiral transition. The strange quark differs from its light partners by mass scale: $m_s/m_{u,d} \approx 26$ in all three models (see Table 3.1). This mass scale difference produces a distinct behavior between the light and strange quark sectors. The strange quark is coupled to the light quarks through the six-quark interaction 't Hooft term $\mathcal{L}_6$ [see Eq. (3.1)]. The 't Hooft coupling K is fixed in the vacuum in order to reproduce the $\eta^{'}$ mass, although its value could be medium dependent [169]. The value of the 't Hooft coupling also affects the structure of the QCD phase diagram; in particular, the location of the CEP depends on its strength [188]. In the chiral limit ($m_u = m_d = 0$), the pattern of chiral symmetry restoration at $\mu_B = 0$ is also affected by the current strange quark mass m_s: it is restored via a first-order phase transition for $m_s < m_s^{crit} \approx 9$ MeV, and via second-order phase transition for $m_s \geq m_s^{crit}$ [201]. The dependence of the tricritical point on the m_s value is studied in [201]. Therefore, we investigate the effect of the magnetic field on the strange quark chiral transition, analyzing the impact of the 't Hooft coupling K and the strange current quark mass m_s on the results.

4.1 PNJL and EPNJL models results

At zero temperature and zero baryonic chemical potential, chiral symmetry of QCD is broken explicitly by the current quark masses and spontaneously by the presence of a non-vanishing quark condensate $\langle \bar{q}q \rangle$. We expect that as the temperature increases chiral symmetry is partially restored – the symmetry is completely restored only in the chiral limit ($m_q = 0$), where the order parameter $\langle \bar{q}q \rangle$ vanishes in the restored phase. Confinement is realized at low temperatures and we have a confined phase (hadronic matter). With increasing temperature, a transition from confined matter to deconfined matter takes place. To study these symmetries, we must define order parameters that probe the state of each symmetry at any temperature and/or chemical potential. Since we are working with the (2+1)-flavors version of the (E)PNJL models, we have three order parameters for the chiral symmetry (one for each flavor), the quark condensates $\langle \bar{q}_i q_i \rangle$ [Eq. (3.35)]. The Polyakov loop Φ [Eq. (3.36)] is the order parameter for deconfinement transition.

At zero magnetic field, the chiral and deconfinement transitions are analytic transitions (crossover transitions) in both PNJL [188] and EPNJL [197] models. The crossover, unlike first- and second-order phase transitions, is characterized, as already referred, by a smooth and continuous change of the order parameters and thermodynamical quantities with temperature and/or chemical potential. Therefore, only a pseudocritical temperature can be defined for a crossover [22, 25, 26]. We define the chiral pseudocritical temperature T_i^χ for the i-quark as the temperature at which the inflection point of the quark condensates $\langle \bar{q}_i q_i \rangle$ occurs, i.e., the temperature at which $d^2 \langle \bar{q}_i q_i \rangle (T)/dT^2 = 0$. The pseudocritical temperature for the deconfinement transition T_c^Φ is also defined as the inflection point of the Polyakov loop. For each order parameter i, we define the respective susceptibility C_i as

$$C_i = -m_\pi \frac{\partial \sigma_f}{\partial T}, \quad i = u, d, s \tag{4.1}$$

$$C_\Phi = m_\pi \frac{\partial \Phi}{\partial T}, \tag{4.2}$$

where

$$\sigma_i(B,T) = \frac{\langle \bar{q}_i q_i \rangle (B,T)}{\langle \bar{q}_u q_u \rangle (0,0)} \tag{4.3}$$

is the vacuum renormalized quark condensate. The multiplication by m_π in the susceptibilities C_f ensures a dimensionless quantity and is just a matter of convenience. Likewise, the minus sign in the quark susceptibilities ensures a positive quantity. Because of the distinct electric charge of the up ($q_u = 2e/3$) and the down ($q_d = -e/3$) quarks, the pseudocritical transitions T_u^χ and T_d^χ are different in the presence of a magnetic field. Thus, we define the pseudocritical temperature of the chiral transition as $T_c^\chi = (T_u^\chi + T_d^\chi)/2$, where T_u^χ and T_d^χ are, respectively, the pseudocritical transition temperature for u- and d-quarks. The pseudocritical temperature of the strange quark transition T_s^χ will be analyzed in Section 4.3.

We show all order parameters (σ_i and Φ) and respective susceptibilities (C_i and C_Φ) as a function of temperature in Fig. 4.1, for three magnetic field intensities: $eB = 0$, 0.4, and 0.8 GeV^2. The Magnetic Catalysis (MC) effect is clear: the magnetic field enhances all quark condensates at any temperature. Moreover, as the magnetic field increases, the effect of the electric charge of each quark becomes dominant in the MC effect. For $eB = 0.4$ GeV^2 and $T < 175$ MeV, the u-quark condensate σ_u is already bigger than s-quark condensate σ_s despite its much lower current mass ($m_s/m_{u,d} \approx 26$). As a consequence of the MC mechanism, the inflection point of both light quark condensates moves towards higher temperatures with increasing magnetic field strength, and the pseudocritical temperature for the chiral transition increases. For a fixed temperature, the Polyakov loop decreases with B and the pseudocritical temperature of the deconfinement transition is also shifted to higher temperatures, which is confirmed by the location of the C_Φ maximum value in the lower panels of Fig. 4.1, for both models.

We present the pseudocritical temperatures for the different transitions in Table 4.1 and Fig. 4.2. Due to the different electric charges, the pseudocritical temperatures for u- and d-quark transitions become different as B increases although a stronger difference occurs for the PNJL model. The effective mass of the u-quark becomes larger due to its higher electric charge, affecting the behavior of the respective quark condensate, see left (right) panel of Fig. 4.1 for the PNJL (EPNJL) model. The partial restoration of chiral symmetry in the u-sector is delayed and the transition occurs at a higher pseudocritical temperature than in the d-sector. As the magnetic field becomes stronger, the separation between the chiral (dashed green line) and deconfined (dashed-dotted blue line) pseudocritical transition temperatures increases, as Table 4.1 and Fig. 4.2 show. This effect is much stronger for the PNJL model than for the EPNJL model (see Fig. 4.2). In the EPNJL model, the entanglement interaction creates a strong correlation between the quarks and the Polyakov loop, making both pseudocritical temperatures T_c^χ and T_c^Φ almost coincident at zero magnetic field - this mechanism will be analyzed in detail in the next Section. Anyway, this coincidence is destroyed by the magnetic field presence. A gap between chiral and deconfinement pseudocritical transition temperatures is obtained, being, however, much wider in PNJL model than in the EPNJL model (see Fig. 4.2).

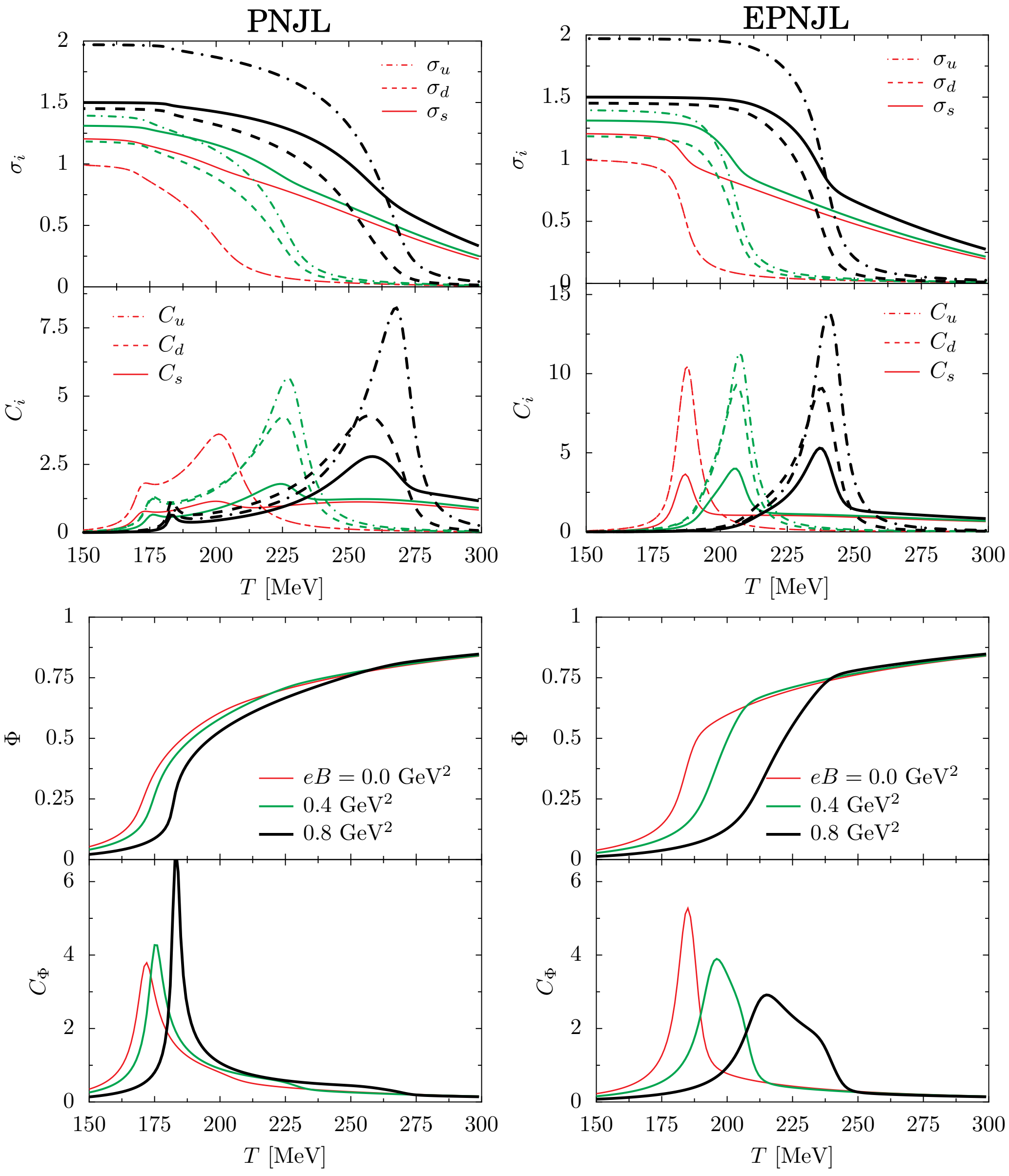

Figure 4.1: Vacuum renormalized quark condensates σ_i (top panel), the Polyakov loop Φ (bottom panel), and their respective susceptibilities C_i as a function of temperature, within PNJL (left) and EPNJL (right) models, for three magnetic field strengths: $eB = 0$ GeV^2 (red lines), $eB = 0.4$ GeV^2 (green lines), and $eB = 0.8$ GeV^2 (black lines)

eB	PNJL				EPNJL			
(GeV^2)	T_c^u	T_c^d	T_c^χ	T_c^Φ	T_c^u	T_c^d	T_c^χ	T_c^Φ
0	200	200	200	171	187	187	187	184
0.2	209	208	208	172	193	193	193	187
0.4	226	224	225	174	206	205	206	195
0.6	246	242	244	178	222	221	222	204
0.8	267	257	262	182	240	237	238	214
1.0	288	271	279	186	257	252	255	224

Table 4.1: Pseudocritical temperatures in MeV for the chiral $T_c^\chi = (T_u^\chi + T_d^\chi)/2$ and the deconfinement T_c^Φ transitions, for both PNJL and EPNJL models with $T_0 = 210$ MeV. We use $T_0 = 210$ MeV in order to obtain $T_c^\Phi(eB = 0) = 171$ MeV as in LQCD calculations - see Section 3.4.1.

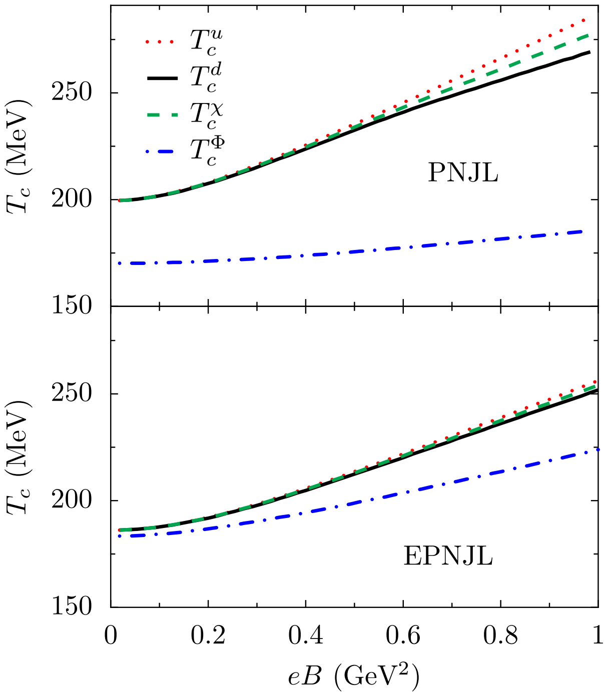

Figure 4.2: Pseudocritical temperatures for up quark, down quark, chiral, and deconfinement transitions as a function of the magnetic field intensity, for PNJL (top panel) and EPNJL (bottom panel).

In the (2+1)-flavor PNJL model, as in the two-flavor PNJL model [96–98], the magnetic field has a smaller impact on the pseudocritical temperature of the deconfinement transition. As eB grows from 0 to 1 GeV^2, the variation in the pseudocritical temperatures is $\Delta T_c^{\Phi} \approx 15$ MeV and $\Delta T_c^{\chi} \approx 79$ MeV. Moreover, the Polyakov loop susceptibilities become narrower with increasing B, and eventually, for sufficiently strong magnetic fields, a first-order phase transition might occur. A different behavior is obtained in the EPNJL model, where the ΔT_c^{Φ} increases by ≈ 40 MeV, as eB goes from 0 to 1 GeV^2. Due to the entanglement interaction, the Polyakov loop susceptibility peak is shifted towards higher temperatures together with the C_u and C_d peaks. However, also due to the entanglement interaction, the C_u and C_d peaks do not move to so high temperatures as in the PNJL model.

It is visible in the PNJL condensate susceptibilities C_i (left top panel of Fig. 4.1) small peaks around the temperature of the C_Φ peak location, which are induced by the deconfinement transition [191, 202, 203]. They do not signal a chiral transition since the variation of the quark condensates (order parameters) are very small around this temperature. A similar effect is seen in the EPNJL Polyakov loop susceptibility C_Φ, but now are of the u- and d-quarks chiral transitions that induce some bumps on the Polyakov loop close to the temperature of the C_u and C_d peaks locations, which are visible on the right bottom panel of Fig. 4.1 for $eB = 0.8$ GeV^2 (black lines).

To understand the magnetic field dependence of the pseudocritical temperatures T_c^i, we perform the parametrization of the crossover transition line introduced in Refs. [62, 115], which is valid for small values of the magnetic field ($eB \lesssim 0.5$ GeV^2):

$$\frac{T_c^i(eB)}{T_c^i(0)} = 1 + A\left(\frac{eB}{m_\pi^2}\right)^{\alpha} \tag{4.4}$$

The numerical values for the best-fit coefficients are given in Table 4.2. The results show what Fig. 4.2 also reveals: the curvature for the deconfinement transition is softer in the PNJL model than in the EPNJL model due to the entanglement interaction between the Polyakov loop and the chiral condensate. Besides the general agreement of the obtained fit coefficients for the $T_c^{\chi}(eB)/T_c^{\chi}(0)$ for both models with the LQCD results obtained in [62], the EPNJL model is the one that has the closest values.

	PNJL		EPNJL	
	A	α	A	α
$T_c^u(eB)/T_c^u(0)$	1.38×10^{-3}	1.50	6.71×10^{-4}	1.65
$T_c^d(eB)/T_c^d(0)$	1.20×10^{-3}	1.52	5.90×10^{-4}	1.68
$T_c^\chi(eB)/T_c^\chi(0)$	1.29×10^{-3}	1.51	6.31×10^{-4}	1.67
$T_c^\Phi(eB)/T_c^\Phi(0)$	5.87×10^{-5}	1.90	4.42×10^{-4}	1.61

Table 4.2: Coefficient A and exponent α of the expansion of the transition temperatures for small values of the magnetic field B [see Eq. (4.4)].

4.2 Entanglement interaction parametrization

In the present section, our aim is to deepen the comparison between the EPNJL and PNJL models. Therefore, we continue to use $T_0 = 210\,\mathrm{MeV}$ in both models. The only constraint we impose on the entanglement interaction parametrization, (α_1, α_2), is that both chiral and deconfinement transitions are crossovers. To study how the order parameters $\langle \bar{q}_i q_i \rangle$ and Φ depend on the entanglement parametrization, we define several sets listed in Table 4.3 that we analyze and compare. These sets sample all the crossover region of the entanglement interaction.

4.2.1 The zero magnetic field case

In Fig 4.3 we show the vacuum normalized condensates σ_i, the Polyakov loop Φ, and their susceptibilities C_i [see Eq. (4.2)] at zero magnetic field. An exact $SU(2)$ isospin symmetry occurs in the magnetic field absence, and thus $\sigma_u = \sigma_d$. The correlation created by the entanglement interaction between the chiral and the deconfinement transitions is clear seen in the C_i.

We recall that the pseudocritical temperatures in the PNJL are $T_c^\chi = 200\,\mathrm{MeV}$ and $T_c^\Phi = 171\,\mathrm{MeV}$, while the results for some parametrization sets that sample all the crossover region are listed in Table 4.3. A conclusion from Table 4.3 is that the restoration of chiral symmetry in the EPNJL model is influenced by the gauge fields mimicked by the Polyakov loop: the deconfinement transition affects the chiral transition, by decreasing the interaction responsible for the chiral symmetry breaking $G_s(\Phi)$ [see Eq. (3.67)] and shifting the chiral symmetry restoration to smaller temperatures; thus, bringing both transition temperatures closer to each other. Furthermore, the $(0.45, 0.00)$ and $(0.00, 0.50)$ sets are in the limit of turning the crossover transition into a first-order phase transition. This is reflected in the susceptibility values at the pseudocritical temperatures, being these more pronounced than for the $(0.20, 0.20)$ set.

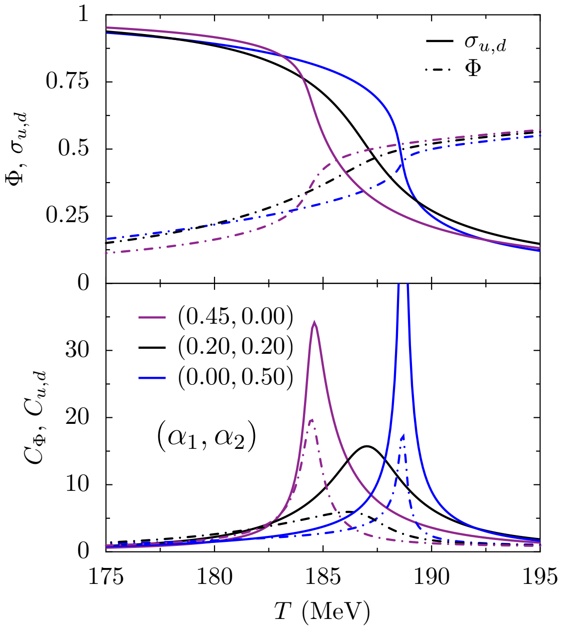

Figure 4.3: Normalized vacuum condensates σ_u and the Polyakov loop Φ (top panel), and their respective susceptibilities (bottom panel), for three parametrization sets (α_1, α_2).

(α_1, α_2)	T_c^χ[MeV]	T_c^Φ[MeV]
$(0.45, 0.00)$	184.6	184.5
$(0.25, 0.10)$	186.4	183.6
$(0.20, 0.10)$	187.3	182.1
$(0.20, 0.20)$	187.0	186.2
$(0.10, 0.20)$	188.4	184.6
$(0.00, 0.50)$	188.7	188.7

Table 4.3: Pseudocritical temperatures for the chiral $T_c^\chi = (T_c^u + T_c^d)/2$ and deconfinement T_c^Φ transitions, for several parametrization sets (α_1, α_2), with $T_0 = 210$ MeV.

We also notice that, even at zero magnetic field, the pseudocritical transition temperatures are quite sensitive to the parametrization (α_1, α_2). They almost coincide for $(0.45, 0.00)$ and $(0.00, 0.50)$, but for $(0.10, 0.20)$ and $(0.20, 0.10)$ we obtain $\Delta T_c = T_c^\chi - T_c^\Phi = 3.8\,\mathrm{MeV}$ and $\Delta T_c = 5.2\,\mathrm{MeV}$, respectively. Therefore, the coincidence of the pseudocritical transition temperatures, the main feature of the entanglement interaction [197], depends on its parametrization.

Now, we analyze within the EPNJL model, how the T_0 value of the Polyakov potential affects, in particular, the pseudocritical transition temperatures. We calculate the pseudocritical temperatures T_c^χ and T_c^Φ as a function of T_0, for three sets of Table 4.3. The results are plotted in Fig. 4.4.

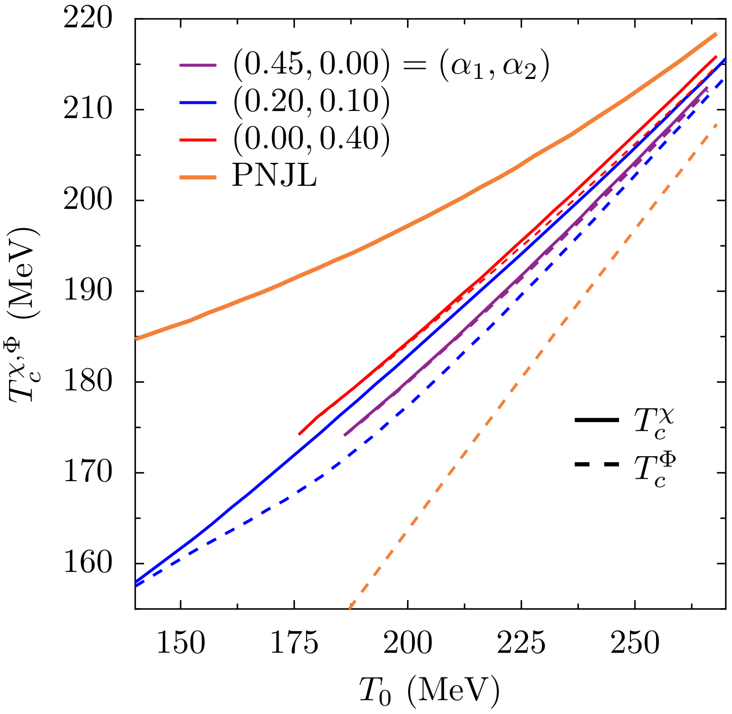

Figure 4.4: Pseudocritical temperatures for chiral $T_c^\chi = (T_c^u + T_c^d)/2$ and deconfinement T_c^Φ transitions as a function of T_0 for several sets (α_1, α_2).

There is a lower value of T_0 (T_0^{1st}) for each set (α_1, α_2) that still gives a crossover transition for both chiral and deconfinement transitions. A first-order phase transition occurs if $T_0 < T_0^{1st}$. The T_0^{1st} values are: $T_0^{1st} = 186$, 125, and 176 MeV, for $(0.45, 0.00)$, $(0.20, 0.10)$, and $(0.00, 0.40)$ sets, respectively. We see in Fig. 4.4 that for T_0 values close to T_0^{1st}, the pseudocritical temperatures of both chiral and deconfinement transitions coincide for all sets. The coincidence of the pseudocritical temperatures for $T_0 > T_0^{1st}$ (crossover region) depends on the parametrization set. A good coincidence is obtained for all range of T_0 within the $(0.45, 0.00)$, but a difference as large as $\Delta T_c \approx 8$ MeV is seen with the $(0.20, 0.10)$ set. The PNJL model result is also shown in Fig. 4.4, having a much larger gap ΔT_c that grows as T_0 decreases.

4.2.2 The effect of an external magnetic field

Now, we are going to analyze how the magnetic field affects the pseudocritical transition temperatures and how it depends on the entanglement interaction parametrization. As we already saw, due to the different electric charges of the up ($q_u = 2e/3$) and down ($q_d = -e/3$) quarks, the isospin symmetry is broken when an external magnetic field is applied to the system, and the u- and d-quark chiral transitions do not coincide anymore.

The pseudocritical temperatures as a function of the magnetic field B for $T_0 = 210\,\mathrm{MeV}$ (hereafter we use again $T_0 = 210\,\mathrm{MeV}$ in both models) are in Fig. 4.5, for three sets: $(0.45, 0.00)$, $(0.20, 0.20)$ and $(0.00, 0.35)$. The pseudocritical transition temperatures coincide for $(0.20, 0.20)$ and $(0.00, 0.35)$ even with a finite magnetic field. In the last set we obtain a first-order phase transition for $eB > 0.91\,\mathrm{GeV}^2$, and for lower values the coincidence on the pseudocritical transition temperatures is perfect. For $(0.45, 0.00)$, unlike the other sets, the magnetic field breaks the coincidence of the chiral and deconfinement transitions at $eB \approx 0.3\,\mathrm{GeV}^2$, and the deconfinement pseudocritical transition temperature is less affected than the chiral pseudocritical transition temperature, even though the magnetic field has the same effect for any (α_1, α_2) parametrization: for a given temperature, B enhances the quark condensates and reduces the Polyakov loop value.

As a result of the charge difference between u- and d-quarks, we obtain a higher pseudocritical transition temperature for the u- than d-quark, and this difference grows as the magnetic field increases. This pattern was also found in the context of the instanton-liquid model, modified by the Harrington-Shepard caloron solution at finite T in the chiral limit [204], or in the Sakai-Sugimoto model [205].

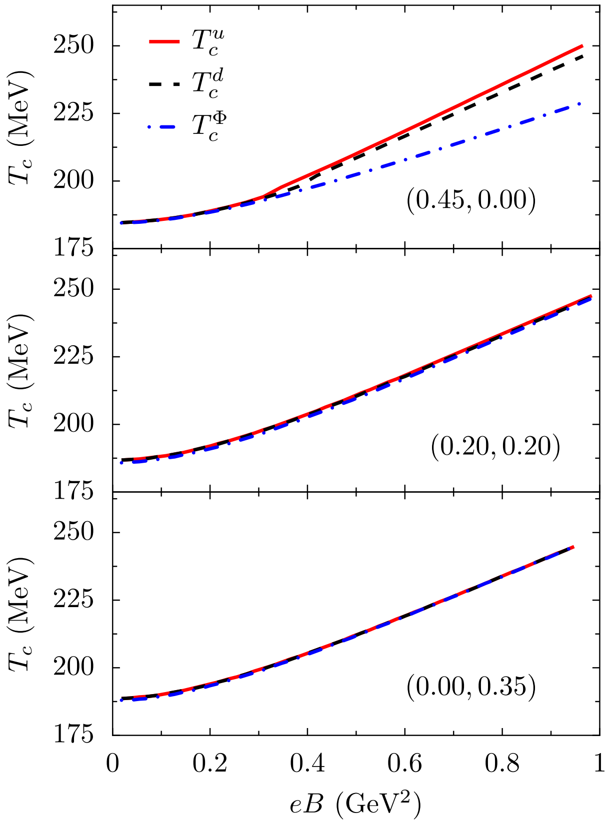

Figure 4.5: Pseudocritical temperatures as a function of the magnetic field for three sets: $(0.00, 0.35)$ (bottom panel), $(0.20, 0.20)$ (middle panel), and $(0.45, 0.00)$ (top panel).

Next, we do a systematic study of the dependence of the pseudocritical temperatures on the entanglement parametrization (α_1, α_2). First, we set $\alpha_1 = \alpha_2 = \alpha$ and calculate the transition temperatures as a function of α, for three magnetic field intensities: $eB = 0$, 0.4, and $0.6\,\text{GeV}^2$. The results are in Fig. 4.6. As α increases, the deconfinement pseudocritical temperature increases and the chiral pseudocritical temperature decreases. At some critical value of α for $eB = 0.4$ and $0.6\,\text{GeV}^2$, the gap between both pseudocritical temperatures abruptly decreases before a first-order phase transition sets in. The gray line of Fig. 4.6 indicates the region plotted in the middle panel of Fig. 4.5, i.e., for the $(0.20, 0.20)$ set.

The effect of varying the entanglement parametrization was already studied in [98], using the two-flavor PNJL model with and without 8-quark interaction term [206–208]. As in the present work, it was found the existence of a magnetic field dependent critical value $\alpha^{1\text{st}}$, where the crossover is replaced by a first-order phase transition. Figure 4.6 also shows that the $\alpha^{1\text{st}}$ depends on B, having smaller values with increasing B. For $\alpha = 0$ the entanglement interaction $G_s(\Phi)$ turns into the coupling G_s^0 [see Eq. (3.67)], therefore, the EPNJL model reduces to the PNJL model for $\alpha = 0$. For any magnetic field strength, the EPNJL model always predicts a smaller gap in $\Delta T_c = T_c^\chi - T_c^\Phi$ than the PNJL model. The ratio $G_s(\Phi)/G_s^0$ is always equal or smaller than one, which means that the model coupling responsible for the chiral symmetry breaking in the PNJL model is always larger than the one in the EPNJL model.

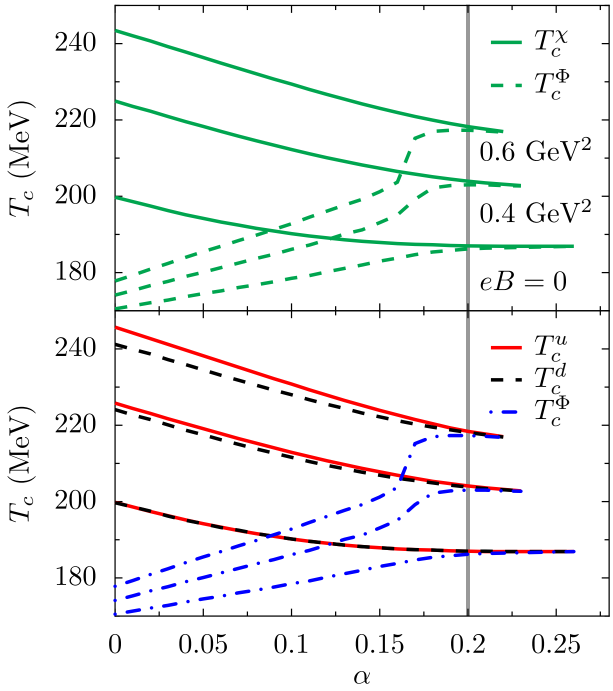

Figure 4.6: Pseudocritical temperatures for chiral T_c^χ and deconfinement T_c^Φ transitions (top panel), and T_c^i, with $i = u, d, \Phi$, (bottom panel) as a function of (α, α), for $eB = 0$, 0.4 and, $0.6\,\text{GeV}^2$. The gray line is the case plotted in the middle panel of the Fig. 4.5

Now, we set $\alpha_1 = 0$ or $\alpha_2 = 0$, and calculate the pseudocritical transition temperatures as a function of $(0, \alpha_2)$ and $(\alpha_1, 0)$, respectively. With $\alpha_1 = 0$ or $\alpha_2 = 0$, the functional form of the entanglement interaction [see Eq. (3.67)] becomes $G(\Phi) \propto \alpha_2 \Phi^3$ or $G(\Phi) \propto \alpha_1 \Phi^2$, respectively. The results are in Fig. 4.7 and show two main differences:

- the α_1^{1st} grows with increasing B for $(\alpha_1, 0)$ (left panel of Fig. 4.7). The transition remains a crossover at any magnetic field strength if we use an α_1 that gives a crossover transition at $B = 0$ (i.e., $\alpha_1 < \alpha_1^{\text{1st}}$ for $B = 0$). Nevertheless, some $(\alpha_1, 0)$ parametrizations allow a first-order phase transition for low B, while a crossover is obtained for higher values of B. The α_2^{1st} has the opposite behavior in the $(0, \alpha_2)$ case (right panel of Fig. 4.7): it is possible to select a $(0, \alpha_2)$ set where a crossover is obtained at $B = 0$, but a first-order phase transition emerges when B increases. This behavior is qualitatively similar to the one found for (α, α) in Fig. 4.6;

- the gap ΔT_c decreases as α_1 or α_2 increase for a fixed B. While the T_c^{Φ} smoothly increases as α_1 grows for $(\alpha_1, 0)$ (left panel of Fig. 4.7), the T_c^{χ} has a sudden change at α_1 values near the critical value α_1^{1st} and then follows the T_c^{Φ} behavior. The opposite happens in the $(0, \alpha_2)$ case: at some α_2 values the T_c^{Φ} shows a sudden increase and then it follows the T_c^{χ} behavior (right panel of Fig. 4.7).

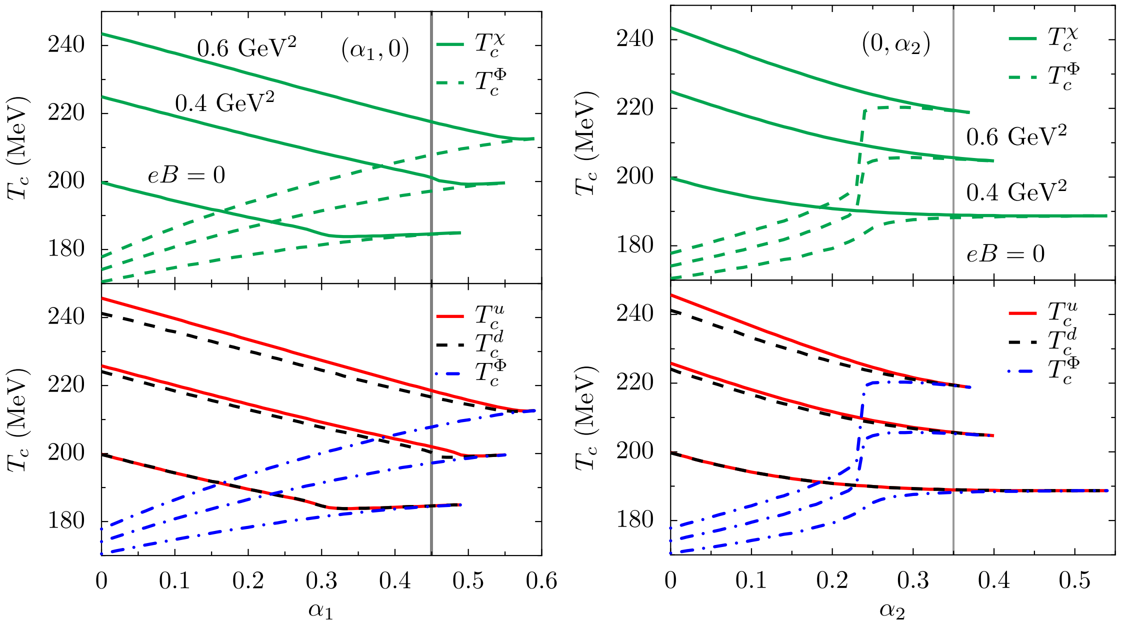

Figure 4.7: Pseudocritical temperatures for chiral T_c^{χ} and deconfinement T_c^{Φ} transitions (top panels), and T_c^i, with $i = u, d, \Phi$, (bottom panels) as a function of $(0, \alpha_2)$ (right panels) and $(\alpha_1, 0)$ (left panels), for $eB = 0$, 0.4, and $0.6\,\mathrm{GeV}^2$. The gray lines are the cases plotted in the top and bottom panels of the Fig. 4.5 for $(0.45, 0.00)$ and $(0.00, 0.35)$ sets, respectively.

The gray lines in both panels of Fig. 4.7 represent the $(0.45, 0.00)$ and $(0.00, 0.35)$ parametrization sets discussed in Fig. 4.5. Their behavior becomes now clear: we are close to a first-order phase transition for $(0.45, 0.00)$ at low B (upper panel of Fig. 4.5); however, the α_1^{1st} grows with increasing B and we are moving into the crossover region where a ΔT_c gap emerges. Because at $B = 0$ we are already close to the $\alpha_2^{\rm 1st}$ for $(0.00, 0.35)$ (bottom panel of Fig. 4.5), there is no ΔT_c gap at low B and a first-order phase transition takes place for $eB > 0.91\,\mathrm{GeV}^2$ (when $\alpha_{\rm 1st} < 0.35$).

4.2.3 Thermodynamics

In the following, we study the behavior of several thermodynamical quantities in the presence of an external magnetic field. The dependence of these quantities on the entanglement interaction parametrization is discussed.

Because we want to study how the entanglement parametrization affects the thermodynamical quantities for fixed values of B, we normalize the thermodynamical potential as follows

$$\Omega_R(B,T) = \Omega(B,T) - \Omega(B,0), \tag{4.5}$$

where $\Omega(B,T)$ is given by Eq. (3.64). Herein, we only analyze the zero baryonic chemical potential ($\mu_B = 0$) case. Therefore, the thermodynamical quantities vanish at zero temperature for any B strength, i.e., $\Omega_R(B,T=0) = 0$.

From the thermodynamic potential $\Omega_R(B,T)$ one can derive some important thermodynamic observables, which can be calculated in lattice QCD. The pressure $P(B,T)$ is given by

$$P(B,T) = -\Omega_R(B,T), \tag{4.6}$$

the entropy density $\mathcal{S}$ by

$$\mathcal{S}(B,T) = \left(\frac{\partial P}{\partial T}\right)_\mu, \tag{4.7}$$

and from the following fundamental relation of thermodynamics, at zero baryonic chemical potential, we can calculate the energy density $\mathcal{E}$ as

$$\mathcal{E}(B,T) = T\mathcal{S}(B,T) - P(B,T). \tag{4.8}$$

The interaction measure is defined as

$$\Delta(B,T) = \frac{\mathcal{E} - 3P}{T^4}, \tag{4.9}$$

which quantifies the deviation from the equation of state of an ideal gas of massless constituents. LQCD studies show that the interaction measure remains large even at very high temperatures, where the Stefan–Boltzmann (SB) limit is not yet reached, and thus some interactions must still be present.

The speed of sound squared

$$v_s^2(B,T)=\left(\frac{\partial P}{\partial \mathcal{E}}\right)_V, \tag{4.10}$$

and the specific heat

$$C_V(B,T)=\left(\frac{\partial \mathcal{E}}{\partial T}\right)_V, \tag{4.11}$$

are important quantities that have also been calculated in LQCD.

For several entanglement parametrizations and the PNJL model, we plot in Fig. 4.8 the scaled pressure P/T^4, scaled energy density $\mathcal{E}/T^4$, and interaction measure Δ as a function of temperature, for three magnetic field strengths: $B=0$; $eB=0.27\,\mathrm{GeV}^2$, being this value an estimation of the maximal magnetic field strength for the LHC [54]; and $0.6\,\mathrm{GeV}^2$, an already very high magnetic field.

Due to the crossover nature of both the chiral and the deconfinement transitions, the pressure, the energy density, and the interaction measure are continuous functions of the temperature. We observe a similar behavior for the three parametrizations of the EPNJL model: a sharp increase in the vicinity of the pseudocritical transition temperature and then a tendency to saturate at the corresponding ideal gas limit. The sharp increase in the PNJL model occurs at lower temperatures than the corresponding effect in the EPNJL model due to the difference in the pseudocritical deconfinement transition temperature given by both models: $T_c^\Phi=171\,\mathrm{MeV}$ in the PNJL model and $T_c^\Phi=182-189\,\mathrm{MeV}$ in the EPNJL (see Table 4.3). The energy density sharply rises above the pseudocritical transition temperature in the EPNJL. In the PNJL model, at $eB=0.6\,\mathrm{GeV}^2$, the energy density shows two bumps corresponding to deconfinement and chiral transitions that are $T_c^\Phi=178\,\mathrm{MeV}$ and $T_c^\chi=244\,\mathrm{MeV}$ (Fig. 4.8), respectively.

The EPNJL model has a much stronger crossover transition than the PNJL model due to the entanglement interaction. The parametrization set $(0.45, 0.00)$ has the sharpest crossover transition. Instead, as the magnetic field increases, the PNJL model shows a much softer and broader crossover transition due to the increasing difference between the pseudocritical temperatures of deconfinement and chiral transitions.

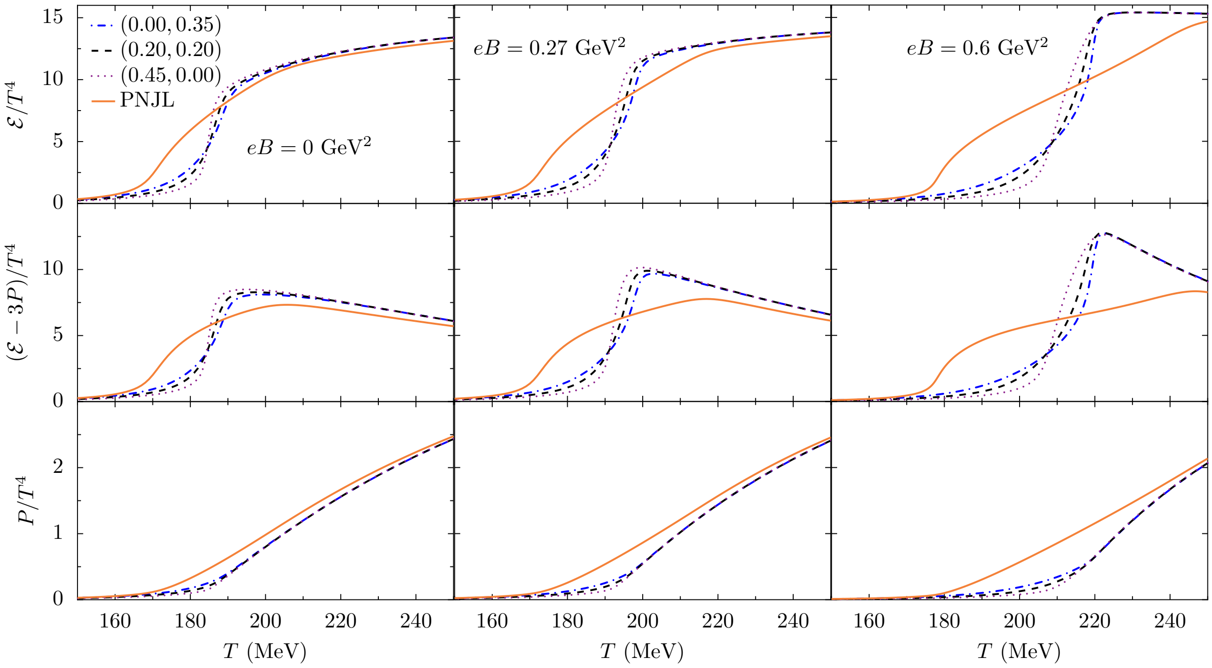

Figure 4.8: The scaled energy density $\mathcal{E}/T^4$ (top panel), the interaction measure $\Delta(T) = (\mathcal{E} - 3P)/T^4$ (middle panel), and the scaled pressure P/T^4 (bottom panel) as a function of temperature, for three magnetic field strengths: 0 (left panel), 0.27 (center panel), and $0.6\,\mathrm{GeV}^2$ (right panel) in both PNJL and EPNL models.

Figure 4.9 shows the scaled specific heat C_V/T^3 and the speed of sound squared v_s^2 as a function of the temperature, also for $eB = 0$, 0.27, and $0.6\,\mathrm{GeV}^2$. At high temperatures a common limit is obtained for the two observables in both models. This was expected since both models have the same number of degrees of freedom. The specific heat increases strongly near the pseudocritical transition temperature at $B = 0$, being much higher in the EPNJL model. Once more we see that the PNJL model shows two peaks in C_V at any B, caused by the distinct chiral and deconfinement pseudocritical transitions temperatures. The first peak is due to the deconfinement and the second to the chiral transition. The speed of sound squared v_s^2 passes through a local minimum around the deconfinement pseudocritical temperature, and then reaches the limit of $1/3$ (SB limit) at high temperatures. This minimum signals a fast change in the quark masses for both EPNJL and PNJL models. The pattern of local minimum shown by v_s^2 as a function of the magnetic field is related to the pseudocritical temperatures at which both transitions occur, as in the case of the peaks of C_V/T^3. Both models approach the SB limit for temperatures lower than 230 MeV for $eB = 0$ and $eB = 0.27$ GeV^2 (left and middle panel of Fig. 4.9), but for $eB = 0.6$ GeV^2 (right panel of Fig. 4.9) the PNJL model is still far from the SB limit because the chiral pseudocritical transition temperature only occurs at 244 MeV, while for the EPNJL model it occurs already for 222 MeV (see Table 4.1).

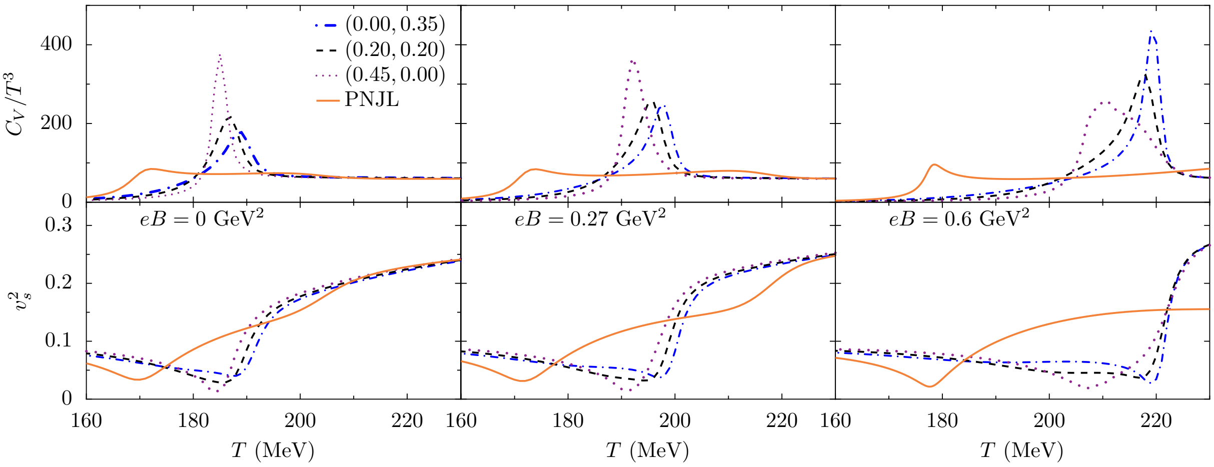

Figure 4.9: The scaled specific heat C_V/T^3 (top panel) and speed of sound squared v_s^2 (bottom panel) as a function of temperature, for three magnetic field strengths: 0 (left panel), 0.27 (center panel) and $0.6\,\mathrm{GeV}^2$ (right panel) in both PNJL and EPNJL models.

It is interesting to look at each entanglement parametrization separately. For $(0.45, 0.00)$, we know (top panel of Fig. 4.5) that T_c^Φ and T_c^χ coincide at low B but not at high B. This is also reflected in the quantities C_V/T^3 and v_s^2: at $B = 0$ the $(0.45, 0.00)$ parametrization has the maximum C_V/T^3 among all the parametrizations, but it decreases as we increase B; at $0.6\,\mathrm{GeV}^2$, aside from having the lowest value, it has the broadest peak, signaling the increasing ΔT_c gap with B. The $(0.00, 0.35)$ parametrization has the lowest C_V/T^3 peak at $B = 0$, but the highest at $eB = 0.6\,\mathrm{GeV}^2$, showing that the parametrization keeps the ΔT_c gap close to zero at any magnetic field strength (see middle panel of Fig. 4.5), and with increasing B the first-order phase transitions becomes closer. At last, for the $(0.20, 0.20)$ parametrization, the maximum value of C_V/T^3 increases slightly with B. Looking at Fig. 4.6, we see that at $eB = 0.6\,\mathrm{GeV}^2$ we have $\alpha_{1\mathrm{st}} > 0.20$, i.e., we are in the crossover region for magnetic fields up to $0.6\,\mathrm{GeV}^2$.

To elucidate the relation between both the chiral and the deconfinement transitions and the induced bumps on the thermodynamic observables, we show in Fig. 4.10 for the PNJL model the scaled specific heat C_V/T^3 for several B values as a function of temperature that is normalized by: the deconfinement pseudocritical transition temperature T_c^Φ (top panel), the down quark pseudocritical transition temperature T_c^d (middle panel), and the up quark pseudocritical transition temperature T_c^u (bottom panel). In the top panel of Fig. 4.10 we clearly see that the first peak location is exactly at the pseudocritical transition temperature of deconfinement for any B value. Since we have defined the pseudocritical temperature of deconfinement as the inflection point of the Polyakov loop, we realize that a pseudocritical temperature defined as the first peak location of C_V/T^3 would give exactly the same T_c^Φ. Despite the small difference of $T_c^d - T_c^u$ for low B values, it increases with B (middle and bottom panels of Fig. 4.10), and at $eB = 1.0$ GeV^2 a two bump structure already appeared, being the first bump induced by the chiral transition of the d-quark and the second by the u-quark. The bump structure of the speed of sound squared v_s^2 would lead to the same conclusions.

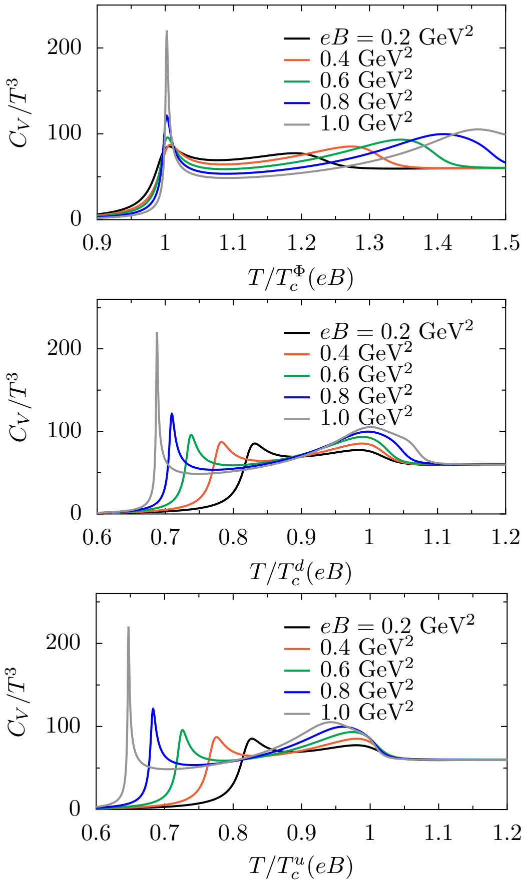

Figure 4.10: The scaled specific heat C_V/T^3 for several B values as a function of temperature that is renormalized by: the deconfinement pseudocritical transition temperature T_c^Φ (top panel), the d-quark pseudocritical transition temperature T_c^d (middle panel), and the u-quark pseudocritical transition temperature T_c^u (bottom panel)

4.3 The strange quark transition

The enhancement in strangeness production is one possible signature of the QGP formation [45]. Thus, the production of strange particles, like strange mesons and baryons, can be used to study the features of QGP. Not only the strange quarks are the easiest quarks to produce after the up and down quarks, but particles with non-zero strange quarks can only be produced in the collision process (strange quarks are absent from the original colliding nuclei). Therefore, the physics related to the strange quarks can give us important information about the properties of the QGP phase.

In the present section, we investigate the effect of the magnetic field on the strange quark chiral transition. As we have mentioned in the introduction of the present Chapter, several features of the QCD phase structure, e.g., the nature of the chiral phase transition in the chiral limit (see Fig. 1.3 in Chapter 1), depend on the current strange quark mass and also on the 't Hooft coupling strength. Therefore, we analyze the impact of the 't Hooft coupling K and strange current quark mass m_s on the quark condensates and on their respective pseudocritical transition temperatures, in the presence of an external magnetic field.

Let us first analyze the order parameters within the complete PNJL model, including the 't Hooft term. In Fig. 4.11 the normalized quark condensates, $\sigma_i = \langle\bar{q}_i q_i\rangle(B,T)/\langle\bar{q}_u q_u\rangle(0,0)$, and their respective susceptibilities, $C_i = -m_\pi \partial\sigma_i/\partial T$, are plotted for three magnetic field strengths.

As we have seen, the quark condensates are enhanced by the presence of the magnetic field. Due to the quark electric charge difference, the up quark condensate σ_u is larger than the strange quark condensate σ_s for $eB = 0.8$ GeV^2, even though the larger current mass of the strange quark ($m_s = 140.7$ MeV) compared with the up quark ($m_u = 5.5$ MeV). The first peaks in the susceptibilities at low temperatures are induced by the deconfinement transition, i.e., by the rapid change of the Polyakov loop with temperature that signals the deconfinement transition (see Section 4.1). As also pointed out in Section 4.1, the deconfinement transition is quite insensitive to the presence of the magnetic field when compared with the chiral transition. A pseudocritical temperature for the strange quark transition can be defined through the third inflection point of its susceptibility. Despite not being as noticeable as the first two C_s inflection points, which are originated by the deconfinement and the up/down chiral transitions, a third inflection point is present at $T \approx 250$ MeV for eB up to ≈ 0.4 GeV^2, as we will analyze in the following.

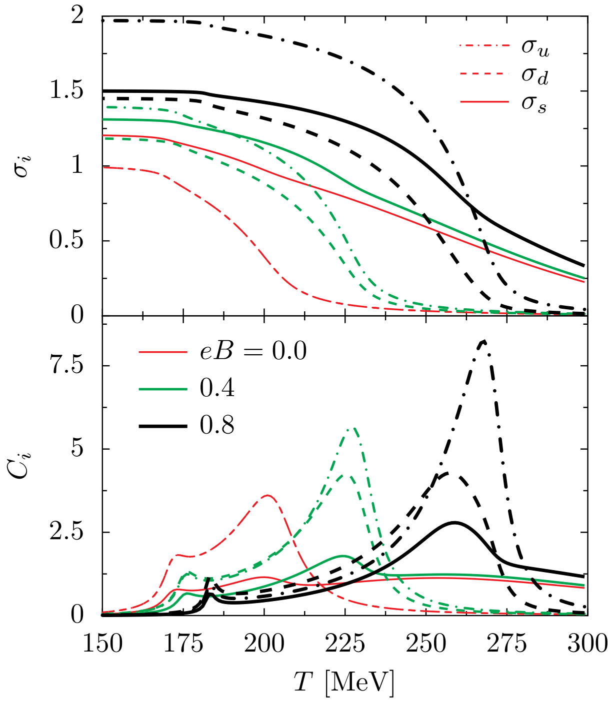

Figure 4.11: The quark condensates (top panel) and their susceptibilities (bottom panel) as a function of temperature, for three magnetic field strengths: $eB = 0$, 0.4, and 0.8 GeV^2.

4.3.1 The impact of the ’t Hooft term

In order to analyze the impact of the ’t Hooft term on the pseudocritical transition temperatures as a function of the magnetic field strength, we consider two cases: the PNJL model with ($K \neq 0$) and without ($K = 0$) the ’t Hooft term. The results are shown in Fig. 4.12, where we have used the following two criteria to calculate the pseudocritical temperatures.

Criterion I: the temperature T_c^i at which the inflection point of the quark condensate $\langle \bar{q}_i q_i \rangle$ occurs (which is the definition that we have been using):

$$\left. \frac{\partial^2 \langle \bar{q}_i q_i \rangle (B,T)}{\partial T^2} \right|_{T=T_c^i} = 0;$$

Criterion II: the temperature T_c^i at which the quark condensate is half of its zero temperature value $\langle \bar{q}_i q_i \rangle (B,0)$:

$$\langle \bar{q}_i q_i \rangle (B, T_c^i) = 0.5 \langle \bar{q}_i q_i \rangle (B,0).$$

Using the first criterion (solid lines) for the $K \neq 0$ case (top panel of Fig. 4.12), the pseudocritical temperature for the strange quark can only be determined up to some maximum B value. For larger B values, the chiral transition for the u- and d-quarks washes out the strange quark transition, and the inflection point of the strange quark condensate, which defines the pseudocritical temperature of the strange quark transition, cannot be defined anymore. This can be overcome if the second criterion (dashed lines) is used. A similar behavior is obtained for the s-quark using the second criterion, but with lower pseudocritical transition temperatures. We also notice from the top panel of Fig. 4.12 that the pseudocritical transition temperatures for the light quarks increase faster with B than for the s-quark. In fact, the pseudocritical strange transition temperature is almost insensitive to the magnetic field strength up to $eB \approx 0.4$ GeV^2, mainly due to its larger effective mass. Another interesting aspect is the increasing split between the pseudocritical temperatures at which chiral and deconfinement transitions occur for the light quarks. This particular feature was already found in the context of the linear sigma model coupled to quarks and to the Polyakov loop in [109]. The Sakai-Sugimoto model also predicts a similar behavior [205].

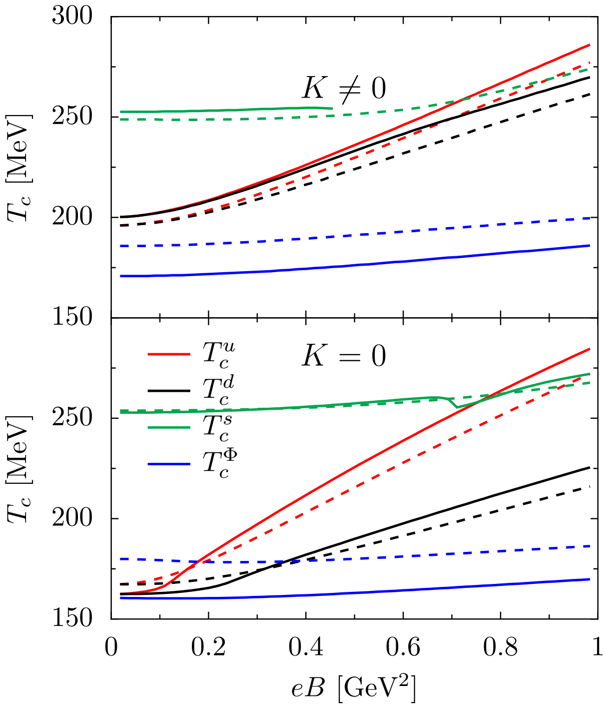

Figure 4.12: The pseudocritical temperatures T_c^i as a function of B for $K \neq 0$ (top panel) and $K = 0$ (bottom panel) using two criteria: the peak of the susceptibilities (solid lines) and half the vacuum value of the order parameters (dashed lines).

When we compare the $K = 0$ case (bottom panel of Fig. 4.12) with the $K \neq 0$ case (top panel of Fig. 4.12), some important features should be pointed out concerning the light quark sector. For $K = 0$ we have:

- For low B values, smaller chiral pseudocritical transition temperatures are obtained, and the difference $T_c^u - T_c^d$ increases faster with B;
- For low B values ($eB \lesssim 0.2$ GeV^2), using the second criterion (dashed lines), the deconfinement pseudocritical transition temperature is higher than the chiral pseudocritical transition temperature, as obtained in LQCD calculations [26, 209];
- The gap between the chiral and deconfinement pseudocritical transitions temperatures is quite small for low B. When we turn on the 't Hooft term, the light chiral transition is pushed to higher temperature values due to the mixing with the strange quark transition. We conclude that the chiral transitions are strongly correlated due to the 't Hooft term, and some features of the QCD phase diagram are precisely defined by this term, e.g., the location of the CEP [169, 188].

Furthermore, we also notice that the strange quark transition is almost insensitive to the presence of the mixing term K: for both cases, $K = 0$ and $K \neq 0$, the strange pseudocritical transition temperature remains almost unchanged (see Fig. 4.12).

In order to understand how the magnetic field affects the strange quark and its pseudocritical transition temperature, it is important to figure out the impact of the chiral restoration of the light sector on its behavior. In Figs. 4.13 and 4.14 we calculate, respectively, for $K \neq 0$ and $K = 0$: the strange quark susceptibilities C_s (top panel), the derivative of the susceptibilities $m_\pi dC_s/dT$ (middle panel), and the susceptibilities of the light quarks $C_{u,d}$ (bottom panel) for several values of B. For the $K \neq 0$ case (Fig. 4.13), the strange quark transition is more strongly influenced by the chiral restoration of the light sector than for the $K = 0$ case (Fig. 4.14). Due to the mixing flavor effect of the 't Hooft term (see the gap equations [Eq. (3.12)] the most pronounced peak in the strange quark susceptibility C_s for $K \neq 0$ is originated by the chiral transition of the up and down quarks (see upper and bottom panels of Fig. 4.13).

The strange quark transition is reflected in the last inflection point of C_s. We see that this inflection point disappears for $eB = 0.6$ GeV^2 (middle panel of Fig. 4.13), being washed out by the transition of the light quarks. With no Hooft term ($K = 0$), there is no flavor mixing in the gap equations, and therefore the pseudocritical temperature of the strange quark transition is clearly identified on its susceptibility. Although some bumps still appear in the derivative of the C_s due to the light quarks, their intensity is much weaker than the transition of the strange quark itself. The absence of flavor mixing effect is confirmed in the bottom panel of Fig. 4.14, where no direct coupling between the u- and d-quarks is seen as the magnetic field increases, contrarily to what happens in the $K \neq 0$ case (see bottom panel of Fig. 4.13).

4.3.2 The impact of the current strange quark mass

As we have seen in the last Section, due to its larger current mass ($m_s/m_{u,d} \approx 26$), the transition to the partially restored region for the strange quark has a different behavior when compared with the light quarks. For low magnetic field strengths, its pseudocritical temperature does not change much when compared with the light quarks. As expected, the restoration of the chiral symmetry will depend not only on the quark electric charges, but also on their current quark masses. Effects of the magnetic field become noticeable when B becomes of the order of the quark mass squared.

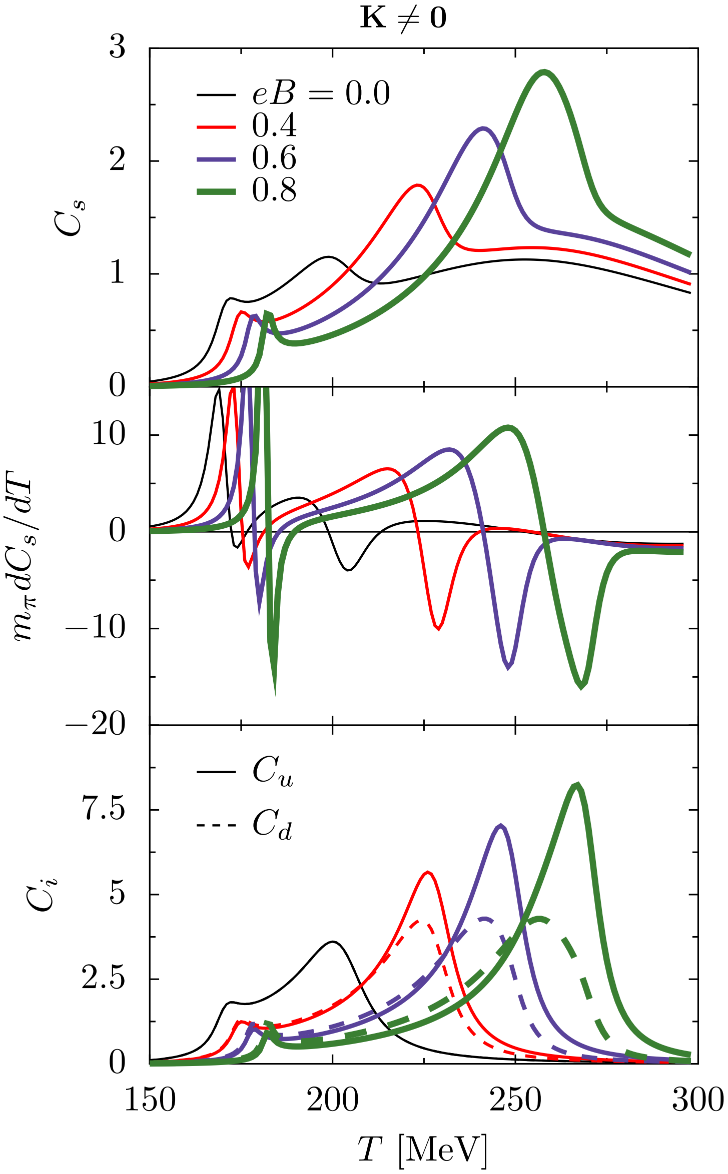

Figure 4.13: The strange quark susceptibilities C_s (top panel), $m_\pi dC_s/dT$ (middle panel), and the up (solid lines) and down (dashed lines) quarks susceptibilities $C_{u,d}$ as a function of B with the 't Hooft term.

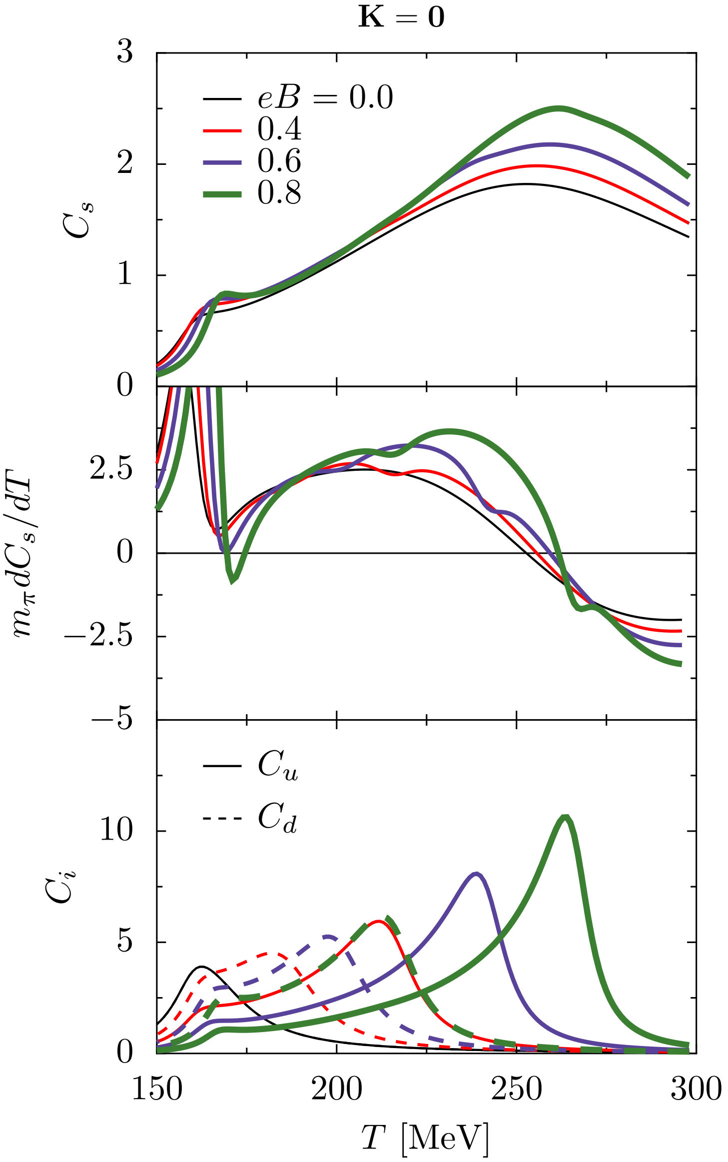

Figure 4.14: The strange quark susceptibilities C_s (top panel), $m_\pi dC_s/dT$ (middle panel), and the up (solid lines) and down (dashed lines) quarks susceptibilities $C_{u,d}$ as a function of B without the 't Hooft term.

Next, we analyze how the restoration of the chiral symmetry depends on the strange quark current mass m_s value, keeping $m_{u,d} = 5.5$ MeV fixed. This dependence was already investigated in both NJL and PNJL models at zero magnetic field [191,201]. In this section the PNJL model with 't Hooft term ($K = 12.36/\Lambda^5$) is used.

Let us start by analyzing the impact of the current mass of the strange quark on the quark condensates. The renormalized quark condensates are plotted as function of temperature in Fig. 4.15 for $eB = 0.1$ GeV^2 (top panel) and 0.5 GeV^2 (bottom panel), using three values of strange current mass: $m_s = m_{u,d} = 5.5$ MeV (red lines), 40 MeV (black lines), and 140.7 MeV (green lines). The three quarks form an isospin triplet for $m_s = m_{u,d}$ that is broken by the magnetic field presence. Therefore, the differences in the condensates are only induced by the electric charge difference of each quark, having the σ_u the highest absolute value ($|q_u| = 2e/3$), and both σ_d and σ_s the lowest ($|q_{d,s}| = e/3$). The effect of the charge is always present independently of the quark masses.

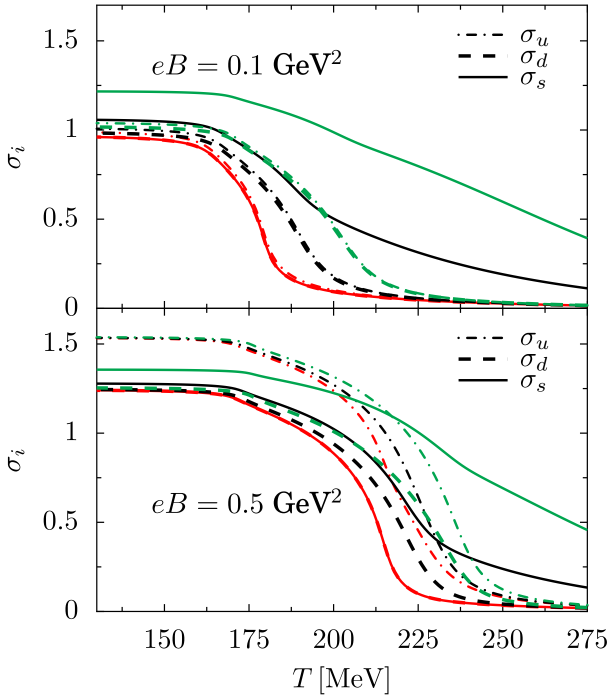

Figure 4.15: The quark condensates as a function of temperature with $m_s = m_{u,d} = 5.5$ MeV (red lines), $m_s = 40$ MeV (black lines), and $m_s = 140.7$ MeV (green lines), for $eB = 0.1$ GeV^2 (top panel) and 0.5 GeV^2 (bottom panel).

The degeneracy of σ_d and σ_s is lifted when we set $m_{u,d} \neq m_s$, i.e., for $m_s = 40$ and 140.7 MeV. We see that for a low magnetic field strength, 0.1 GeV^2 (top panel of Fig. 4.15), with $m_s = m_{u,d}$ (red), the up quark condensate has the highest value at any temperature due to its electric charge. However, if $m_s = 40$ (black line) or 140.7 MeV (green line), the strange quark condensate has the highest value. If m_s is of the order of $m_{u,d}$, the MC effect is mainly determined by the quark electric charge at low B, and it gets weaker with increasing m_s. As the strange current quark mass increases, the restoration of chiral symmetry in the light sector is pushed to higher temperatures due to the flavor mixing induced by the 't Hooft term. For larger magnetic fields, e.g. 0.5 GeV^2 (bottom panel of Fig. 4.15), and low temperatures, the up and down quark condensates are not much affected by the m_s value. At low temperatures, the effect of the quark electric charge in MC predominates over the effect of the strange current quark mass.

In Fig. 4.16, we fix the m_s value to its physical current mass of 140.7 MeV, and calculate the quark condensates (top panel) and masses (bottom panel) as a function of B, for three temperatures: 190 (solid lines), 240 (dashed lines), and 270 MeV (dashed-dotted lines).

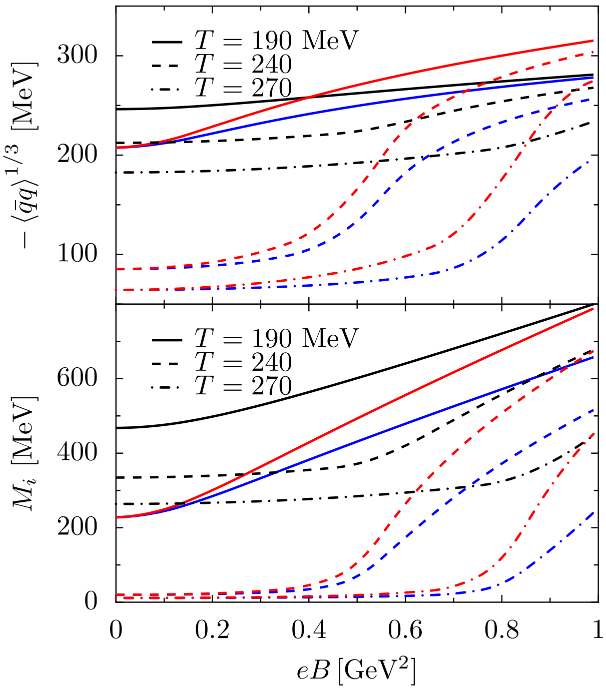

Figure 4.16: The quark condensates (top panel) and masses (bottom panel) of the strange (black lines), up (red lines), and down (blues) quarks as a function of B, for three temperatures ($m_s = 140.7$ MeV).

The distinct behavior between both sectors is clear: at low B and for both $T = 240$ and 270 MeV, the light quarks are in a restored chiral phase, but for higher value of B, the magnetic field drives the light quarks into a chiral broken phase, manifested in the sudden increase of the condensate values. This occurs for larger values of B and temperature. The values of the strange quark condensate and mass are high for all the calculated B range, and for the three temperatures. Although it is difficult to define the chiral restored/broken phase for the strange quark, a similar behavior can be noticed when compared with the light sector, mainly by the quark masses at $T = 240$ and 270 MeV (bottom panel of Fig. 4.16): the strange quark condensate increases slightly for low B , and there is a steeper increase of the masses at some B value.

Next, we perform the same calculation as we did in Fig. 4.16, but now for three m_s values: 5.5 MeV (bottom panel), 40 MeV (middle panel), and 140.7 MeV (top panel). The result is in Fig. 4.17. In the bottom panel we have three degenerate quark masses and, as we mention before, the differences between the different flavors are only due to the quark electric charge. As m_s increases, in the center and top left panels of Fig. 4.17, the strange quark condensate gets less affected by B, reflecting its higher constituent mass and the consequent shift of the chiral restoration to larger temperatures. As it can be seen on the right panel of Fig. 4.17, the light sector also feels the change in m_s. This is more clearly seen for $T = 190$ MeV (solid lines): the condensates are softened with increasing m_s. As we increase the m_s value, due to the flavor mixing, not only the pseudocritical transition temperature of the strange quark increases, but also the transition of the light quarks is shifted to larger temperatures.

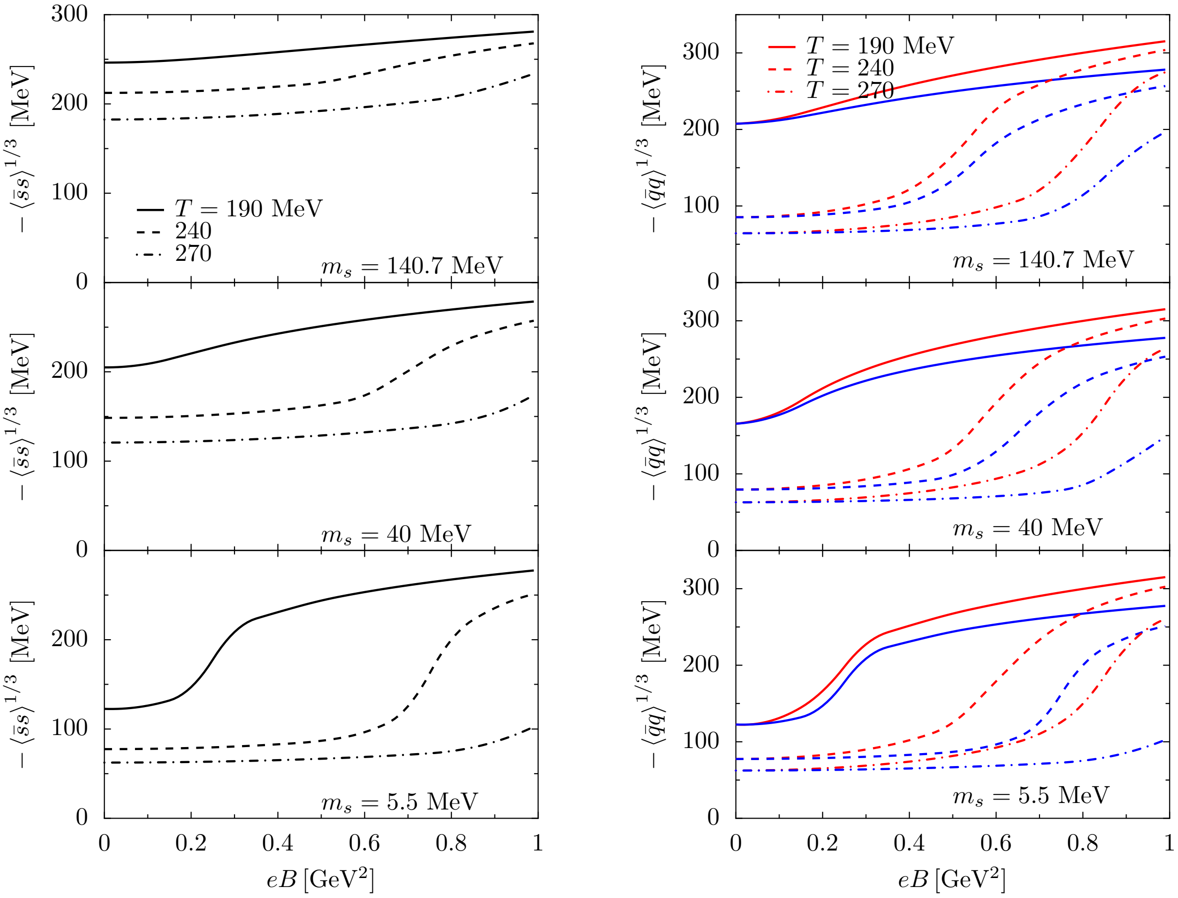

Figure 4.17: The strange quark condensate (black) on the left panel, and up (red) and down (blue) quark condensates on right panel as a function of B, for three temperatures and three current strange quark mass values: 140.7 MeV (top panels), 40 MeV (middle panels), and 5.5 MeV (bottom panels).

Next, we calculate the pseudocritical temperatures as a function of B for two cases: an intermediate case between the light and heavy quark sectors, $m_s = 40$ MeV (top panel), and an extreme heavy case, $m_s = 300$ MeV (bottom panel). The result is presented in Fig. 4.18. Two main conclusions can be drawn:

- for $m_s = 40$ MeV and at high magnetic fields ($eB > 0.3$ GeV^2), the transition of the strange quark occurs at the same pseudocritical temperature as the down quark. This indicates that for a sufficiently high magnetic field, because the current quark masses of all quarks are not too different, the pseudocritical temperatures at which the chiral symmetry restoration occur are mainly determined by the quark electric charge;

- for $m_s = 300$ MeV, the pseudocritical temperature of the strange quark does not change much with the magnetic field due to its very large mass.

Although the MC affects all quarks, the light sector shows an increase of the pseudocritical temperature with the magnetic field, while the strange sector is almost insensitive at low magnetic fields, and increases only slightly for high magnetic fields.

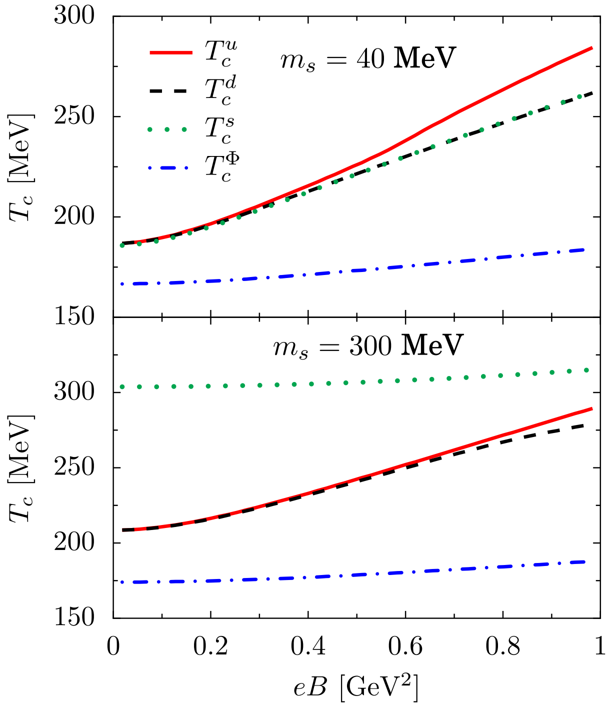

Figure 4.18: The pseudocritical temperatures as a function of B for two current quark mass values: $m_s = 40$ MeV (top panel) and $m_s = 300$ MeV (bottom panel).

4.4 Conclusions

We have seen that an external magnetic field catalyzes the chiral symmetry breaking, effect known as Magnetic Catalysis (MC), in both the PNJL and the EPNJL models: the magnetic field strengthens the quark condensates. The enhancement of the quark condensates, due to the MC effect, occurs at any temperature, leading to an increase pseudocritical temperature as a function of the magnetic field strength. The effect of the electric charge of each quark becomes dominant as the magnetic field increases, which is manifested in the increasing gap between the up and down quark chiral pseudocritical transition temperatures with B. The Polyakov loop decreases with B for a fixed temperature, and the pseudocritical temperature of the deconfinement transition is also shifted to higher temperatures in both models.

The entanglement interaction generates a strong correlation between the quark condensates and the Polyakov loop, turning the gap between the pseudocritical temperatures of the chiral and the deconfinement transitions smaller in the EPNJL model. A systematic study of the dependence of the pseudocritical temperatures on the entanglement parametrization (α_1, α_2) was performed. Even in the presence of a magnetic field, the coincidence of both pseudocritical temperatures can be realized with a proper parametrization.

The pattern of local minimum shown by some thermodynamical quantities, such as the speed of sound squared v_s^2 and the scaled specific heat C_V/T^3, are related to the pseudocritical temperatures at which both, chiral and deconfinement, transitions occur. Due to the chiral restoration of the light quarks at lower temperatures, the strange quark transition, which happens at higher temperatures, is not noticeable in the thermodynamical quantities.

The impact of the 't Hooft term and the current strange quark mass in the strange quark transition was also studied. Without the 't Hooft term there is no flavor mixing in the EPNJL/PNJL model gap equations. While the light quarks are affected by the flavor mixing, the strange quark is almost insensitive to its presence, even in the presence of an external magnetic field. This feature is related to its higher current mass m_s, when compared with the masses of the light quarks.

Chapter 5

(E)PNJL model versus LQCD results

In the previous Chapter, we saw that the chiral pseudocritical transition temperature increases with the magnetic field strength in both EPNJL and PNJL models, just as in almost all effective models and some older LQCD studies [62]. This behavior arises from the Magnetic Catalysis (MC) mechanism: the magnetic field enhances the quark condensates at any temperature, leading to an increase of the pseudocritical transition temperature with B. The strength of the MC depends on the quark flavor due to the electric charge difference.

However, the most recent LQCD results show the inverse mechanism, the so-called Inverse Magnetic Catalysis (IMC), where the quark condensate has a non-monotonic behavior with B for temperatures around the pseudocritical transition temperature region [57, 60]. Instead of enhancing, the magnetic field suppresses the quark condensates near the pseudocritical transition temperature, giving them a non-monotonic behavior as a function of B. Thus, a decreasing dependence of the chiral pseudocritical transition temperature on the magnetic field was obtained [57, 60].

In the present Chapter, we compare both (E)PNJL models with the LQCD results [57, 60], and confirm that the models do not reproduce IMC.

5.1 Behavior of the quark condensates

At zero temperature, the Polyakov loop is zero and all three NJL, PNJL, and EPNJL models coincide. In order to compare the models with the LQCD results, we define, according to [60], the change of the quark condensate due to the magnetic field as

$$\Delta\Sigma_f(B,T) = \Sigma_f(B,T) - \Sigma_f(0,T), \tag{5.1}$$

with

$$\Sigma_f(B,T) = \frac{2M_f}{m_\pi^2 f_\pi^2}\left[\langle \bar{q}_f q_f\rangle (B,T) - \langle \bar{q}_f q_f\rangle (0,0)\right] + 1, \tag{5.2}$$

where m_π^2 is the vacuum pion mass ($m_\pi = 135$ MeV), and f_π^2 the pion decay constant ($f_\pi = 87.9$ MeV) of the NJL model in the chiral limit.

We compare the change of the PNJL renormalized condensate $\Delta(\Sigma_u + \Sigma_d)/2$ at zero temperature with LQCD results [60] in the top panel of Fig. 5.1. Our results agree quantitatively well, and even at $eB = 1$ GeV^2 the discrepancy is only $\sim 10\,\%$, which is much smaller than the prediction of chiral perturbation theory and two-flavor PNJL model (see Ref. [60]). As expected, we obtain a quadratic dependence of $\Delta(\Sigma_u + \Sigma_d)/2$ on B for small fields ($eB < m_\pi^2$), and a linear dependence for higher fields ($eB \gg m_\pi^2$) [143].

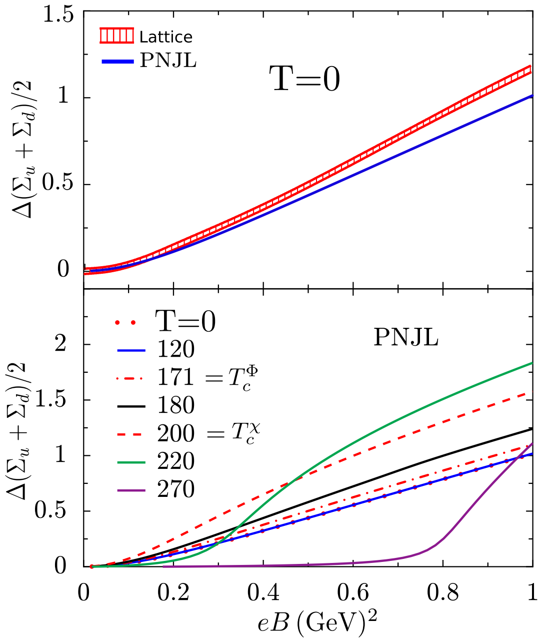

Figure 5.1: $\Delta(\Sigma_u + \Sigma_d)/2$ as a function of B at zero temperature for PNJL and LQCD results [60] (top panel), and within PNJL for several temperatures (in MeV) close to the pseudocritical temperatures (bottom panel): $T_c^\Phi(B=0) = 171$ MeV for deconfinement and $T_c^\chi(B=0) = 200$ MeV for chiral transitions (see Table 4.1).

Using the PNJL model, we plot the change of average light quark condensate $\Delta(\Sigma_u + \Sigma_d)/2$ as a function of the magnetic field intensity for several temperatures in bottom panel of Fig. 5.1. We see that $\Delta(\Sigma_u + \Sigma_d)/2$ increases with B for $T < T_c^\chi(B = 0)$ due to the MC effect, being its value greater at higher temperatures. When $T > T_c^\chi(B = 0)$ we are in the region where the partial restoration of chiral symmetry already took place, where two competitive effects are present: partial restoration of chiral symmetry and MC. The former effect prevails at lower values of B, making the quark condensate approximately zero. The latter effect becomes dominant as the magnetic field increases and the quark condensate becomes nonzero. As an example, let us take the $T = 270$ MeV case (purple line): since $T = 270$ MeV is larger than $T_c^\chi(B = 0)$, the quark condensate is approximately zero already for small values of B and starts to increase around $eB = 0.6$ GeV^2, which is a strong enough magnetic field to counterbalance the effect of the restoration of chiral symmetry. Therefore, the quark matter, which in the absence of a magnetic field was in a chiral restored phase, is forced by B into a broken chiral phase again.

The EPNJL model results are qualitatively similar to PNJL model ones. However, it is important to remember some new features of the EPNJL model. As already mentioned, the coincidence that exists between the deconfinement and chiral pseudocritical transition temperatures at $B = 0$ (see Table 4.1 of Section 4.1) is destroyed by the presence of an external magnetic field. When compared with PNJL, the effect of the entanglement interaction (EPNJL model) is seen on the larger (smaller) increase of T_c^Φ (T_c^χ), as already discussed in the previous Chapter.

The values of light quark condensate sum $(\Sigma_u + \Sigma_d)/2$ and difference $(\Sigma_u - \Sigma_d)$ at zero temperature as functions of B from LQCD [60] and PNJL model (the NJL, PNJL, and EPNJL models coincide at zero temperature) are in Table 5.1. Both the average and the difference of light condensates are in good agreement with LQCD results, especially at low magnetic fields. However, a significant difference between PNJL and LQCD calculations occurs for larger values of B, with the LQCD predicting a larger difference between both condensates. This means that the effect due to the different electric charge of each quark is stronger in the LQCD calculations [60].

At zero temperature the model predictions agree qualitatively and, to some extent, quantitatively with LQCD results [57,60]. But when one compares the bottom panel of Fig. 5.1 with Fig. 5.2 (taken from [60]), an absent feature from our results shows up: there is no suppression of the quark condensate near the pseudocritical temperature. Instead, the quark condensate is enhanced at any temperature by the magnetic field. Therefore, the model does not reproduce the non-monotonic behavior of the condensates with B near the pseudocritical transition temperature seen in LQCD results [57, 60].

$T = 0$	$eB = 0$		$eB = 0.2$ GeV^2		$eB = 0.4$ GeV^2	
	$+/2$	$-$	$+/2$	$-$	$+/2$	$-$
(E)PNJL	1	0	1.11	0.08	1.32	0.23
Latt. [60]	1	0	1.14(2)	0.09(2)	1.37(2)	0.28(2)

$T = 0$	$eB = 0.6$ GeV^2		$eB = 0.8$ GeV^2		$eB = 1.0$ GeV^2	
	$+/2$	$-$	$+/2$	$-$	$+/2$	$-$
(E)PNJL	1.55	0.40	1.79	0.58	2.02	0.76
Latt. [60]	1.63(3)	0.47(3)	1.90(3)	0.67(3)	2.16(3)	0.87(3)

Table 5.1: The average light quark condensate $(\Sigma_u + \Sigma_d)/2$ and the difference $(\Sigma_u - \Sigma_d)$ for the (E)PNJL models together with the continuum extrapolated lattice results at zero temperature [60].

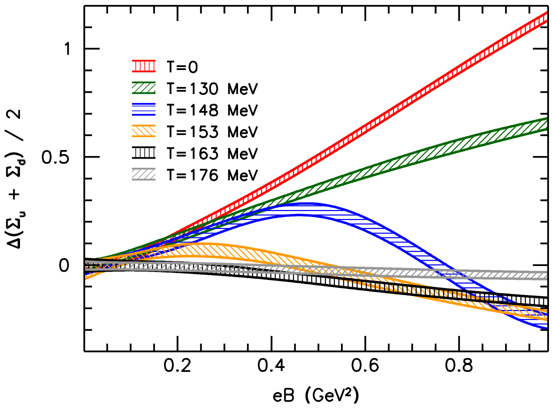

Figure 5.2: The LQCD results for the average light quark condensate as a function of B for several temperatures. The figure was taken from [60].

To compare the average $(\Sigma_u + \Sigma_d)/2$ and difference $(\Sigma_u - \Sigma_d)$ of the light quark condensates at finite temperature with LQCD, we need to remove, somehow, the IMC effect from LQCD results. For that, we calculate the quark condensate average and difference as a function of renormalized temperatures $T/T_c^\chi(eB)$. The average (top panel) and the difference (bottom panel) between light quark condensates are plotted in Fig. 5.3 as a function of $T/T_c^\chi(eB)$, for several values of B, for the PNJL model (dashed lines), the EPNJL model (full lines), and also the LQCD results [57, 60].

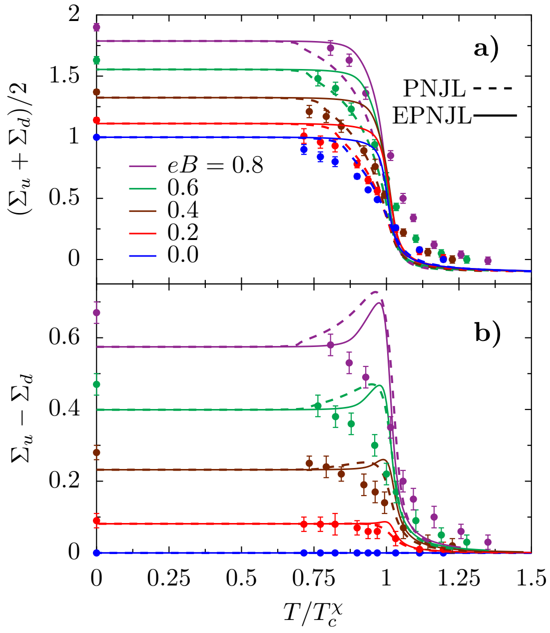

Figure 5.3: Light quark condensate average (top panel) and the light quark condensate difference (bottom panel) together with the LQCD results [57, 60] as a function of temperature (renormalized by $T_c^\chi(B)$) for several values of eB (in GeV^2).

The model results for $(\Sigma_u + \Sigma_d)/2$ in top panel of Fig. 5.3 show that, in general, both PNJL and EPNJL models have the same behavior as LQCD results, except for a too fast drop at the respective pseudocritical transition temperatures. A stronger MC effect on u-quark at finite temperatures due to its larger electric charge is clear from bottom panel of Fig. 5.3: the larger the magnetic field, the larger the difference between up and down quark condensates, and also the respective chiral pseudocritical transition temperatures (see Table 4.1). This feature is particularly strong close to the pseudocritical transition temperature, where curves for stronger fields have a larger bump. This behavior was already found in [204], where the authors use the instanton-liquid model, modified by the Harrington-Shepard caloron solution at finite temperature, to investigate the chiral restoration in the presence of a strong external magnetic field. Above the chiral pseudocritical transition temperature T_c^χ, the quark masses are smaller due to partial restoration of chiral symmetry, prevailing this effect over the MC effect. For these temperatures the u- and d-quark condensate difference is small.

In order to understand the bumps that appear in $\Sigma_u - \Sigma_d$ near the pseudocritical transition temperature for both PNJL and EPNJL model (see bottom panel of Fig. 5.3), we remove the temperature renormalization and show in Fig. 5.4 the i-quark condensate Σ_i, the difference $\Sigma_u - \Sigma_d$, and the susceptibilities of Σ_i, for $eB = 0.4$ (left panel) and $eB = 0.8$ GeV^2 (right panel), in both PNJL (blue) and EPNJL (black) models.

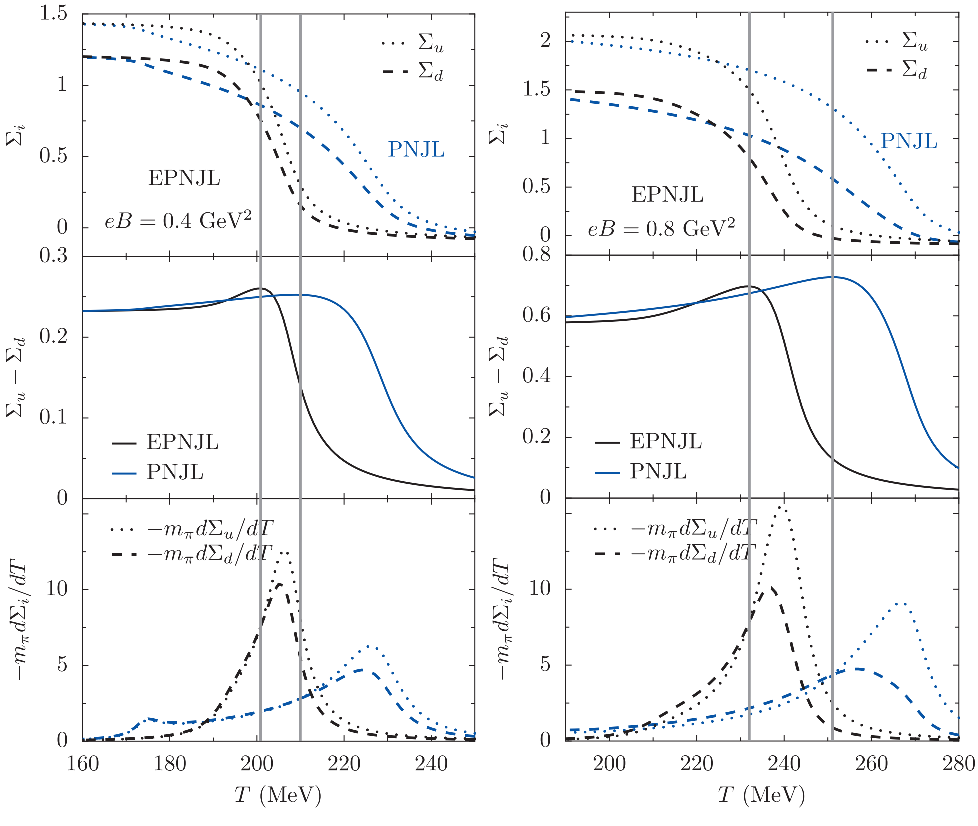

Figure 5.4: The quark condensates Σ_i (top panels), the difference between the u- and d-quark condensates $\Sigma_u - \Sigma_d$ (center panels), and the quark condensates Σ_i susceptibilities (bottom panels) as a function of temperature for the PNJL (blue) and the EPNJL (black), for two magnetic field strengths: $eB = 0.4$ GeV^2 (left) and $eB = 0.8$ GeV^2 (right).

The appearance of these bumps are due to the change of susceptibilities behavior, which is clearer for $eB = 0.8$ GeV^2. The vertical gray lines indicate the temperature at which the $\Sigma_u - \Sigma_d$ takes its maximum value. For temperatures below this value we have $|d\Sigma_d/dT| > |d\Sigma_u/dT|$, and above the opposite happens, i.e., $|d\Sigma_d/dT| < |d\Sigma_u/dT|$. Due to the charge difference, the MC is stronger for u- than d-quarks, therefore: the decrease of the d-quark condensate with temperature is faster at lower temperatures because the partial restoration of chiral symmetry in the up sector is delayed; and at temperatures near the transition temperature region, the Σ_u must decrease with temperature faster than the Σ_d. Thus, the $\Sigma_u - \Sigma_d$ remains constant at low temperatures, then it increases up to a value below the down quark chiral pseudocritical transition temperature, and finally decreases until the chiral symmetry is restored. Instead, a monotonous decrease of the $\Sigma_u - \Sigma_d$ with temperature is seen in LQCD [60].

5.2 The crossover transition

LQCD results show that both chiral and deconfinement transitions remain as analytic crossovers for magnetic fields, at least, up to 1 GeV^2 [57]. In particular, the u-quark transition width decreases only mildly and the height grows significantly. The susceptibilities C_u and C_d are plotted as a function of $T - T_c(eB)$ in Fig. 5.5 for several magnetic field intensities.

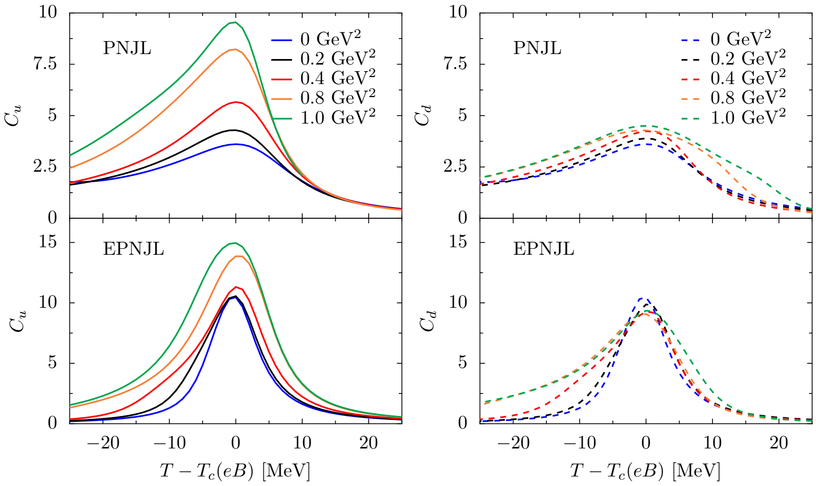

Figure 5.5: Relative changes in the temperature dependence of the chiral susceptibility for the u-quark (left) and the d-quark (right) for different B values within PNJL (top panel) and EPNJL (bottom panel).

In order to have a measure of the transition temperature region, we calculate the Full Widths at Half Maximum (FWHM) of the susceptibilities. The results are in Table 5.2. The FWHM of both C_u and C_d increases with B in the EPNJL model, indicating that the chiral transition becomes broader as B increases. The height does not change much for C_d, but increases for C_u, showing a stronger MC effect on the u-quark. Therefore, the EPNJL model predicts a broader crossover with increasing B, not signaling a first-order phase transition for higher magnetic field strengths. The PNJL model has a different behavior: the FWHM of both C_u and C_d decreases until $eB = 0.8$ GeV^2, and the height increases substantially for the u-quark and slightly for the d-quark. Therefore, the PNJL model predicts a narrower transition band and a stronger chiral transition as B increases up to $eB = 0.8$ GeV^2. For magnetic fields higher than $eB = 0.8$ GeV^2, even though the height of C_u and C_d still increases, as for lower B values, the FWHM of both C_u and C_d increases. This behavior is understandable looking at the PNJL results in the bottom panel of Fig. 5.4, where the separation of both the u- and d-quark chiral transitions becomes more visible for magnetic fields higher than $eB = 0.8$ GeV^2, and the susceptibility of the d-quark becomes broader, reflecting not only its transition, but also the transition of the u-quark occurring at higher but near temperatures.

	PNJL		EPNJL	
eB (GeV^2)	u (MeV)	d (MeV)	u (MeV)	d (MeV)
0.0	37	37	9	9
0.2	26	27	10	11
0.4	22	28	11	13
0.8	21	28	13	16
1.0	22	36	15	17

Table 5.2: Full Widths at Half Maximum (in MeV) of C_u and C_d of Fig. 5.5.

5.3 Conclusions

In this Chapter, we have confirmed that even though the models reproduce the LQCD results at zero temperature they do not predict any suppression of the quark condensates near the transition temperature region. The quark condensates have a monotonic behavior: at any temperature they are increasing functions of the magnetic field strength, and thus no IMC effect is present. Anyway, both chiral and deconfinement transitions are analytic crossovers within EPNJL/PNJL models for magnetic fields up to 1 GeV^2, in agreement with LQCD results [57, 60].

In the next Chapter, we explore two mechanisms that reproduce the IMC effect seen in LQCD results.

Chapter 6

Inverse Magnetic Catalysis

Recent LQCD calculations using $N_f = 2+1$ flavors with physical quark masses have investigated the effect of an external magnetic field on QCD matter [57,58,60]. An unexpected result was obtained: the magnetic field suppresses the light quark condensates – the light and strange quark sectors respond differently – near the transition temperature region, the so-called Inverse Magnetic Catalysis (IMC) effect, resulting in a non-monotonic behavior of the light quark condensates with B. The deconfinement pseudocritical transition temperature, calculated from the renormalized Polyakov loop, also decreases with the magnetic field [58]. Furthermore, the strange quark number susceptibility that is also a quantity that signals the deconfinement transition also decreases with B [57]. Therefore, these LQCD results show that both pseudocritical temperatures of chiral, due to the suppression of the light quark condensates near the pseudocritical chiral transition, and deconfinement transitions are decreasing functions of the magnetic field.

In [58], the effect of the magnetic field on chiral symmetry breaking was separated into two distinct mechanisms: sea and valence effects. The valence effect explains the Magnetic Catalysis (MC) mechanism: the magnetic field enhances the spectral density around zero, and thus, through Banks-Casher relation [149], the quark condensate. The sea effect is a consequence of the re-weight of the gauge configurations in the path integral due to B. This re-weight suppresses small and favors large values of the Polyakov loop, being more intense around the pseudocritical transition temperature. The increase of the Polyakov loop value suppresses low Dirac eigenvalues, and thus the condensate is suppressed around the pseudocritical transition temperature (IMC effect).

The thermo-magnetic correction to the quark-gluon vertex in the presence of a weak magnetic field within the hard thermal loop approximation was studied in [156]. The authors have shown that the effective thermo-magnetic quark-gluon coupling decreases as a function of the field strength [156]. The effects of strong magnetic fields on the QCD phase diagram solving the gluon and quark gap equations was performed in [155]. The main argument is that the phenomenon of IMC is due to the combination of gluon screening effects and the weakening of the strong coupling [155].

In this Chapter, based on several studies that show a weakening of the QCD running coupling constant in the presence of an external magnetic field, two mechanisms are developed to incorporate into NJL-type models, through the model coupling, the back-reaction of the magnetized quarks on the gauge fields, and investigate if IMC can be reproduced.

6.1 The Polyakov loop with a B dependence

In (E)PNJL models the deconfinement is described by the Polyakov loop that couples weakly to the magnetic field, as we saw in Chapter 4. The Polyakov loop potential was originally parametrized to reproduce pure gauge lattice results ($T_0 = 270$ MeV). Later, it was realized that the inclusion of dynamical quarks leads to a decrease of the scale parameter T_0 to 210 MeV in order to obtain $T_c^\Phi = 171$ MeV. Since a strong magnetic field affects dynamical quarks, one expects that the B presence can also influence the value of T_0.

One possible approach to mimic the back-reaction of the gluon sector to the presence of an external magnetic field is to introduce a magnetic field dependent $T_0(B)$, which reproduces the correct LQCD deconfinement transition temperatures [57, 60]. This kind of procedure on T_0 had already been proposed in a different context [210–212]: based on renormalization group arguments, an explicit quark chemical potential and N_f dependence on T_0 in the Polyakov loop potential takes into account the back-reaction of the quark degrees of freedom on the Polyakov loop.

Next, by imposing a magnetic field dependence through T_0 in the Polyakov potential within the (E)PNJL models, we analyze whether the LQCD results [57, 60] can be reproduced. It should, however, be mentioned that a too small T_0 value originates a first-order phase transition for both chiral and deconfinement transitions. We limit T_0 to a range of values that preserve the crossover nature of both transitions.

6.1.1 Parametrization of the $T_0(eB)$

We start by pointing out that it is impossible to implement the above scheme using the PNJL model: even though a decreasing T_0 with increasing B brings the deconfinement pseudocritical transition temperature to lower values (as in LQCD [57]), the chiral pseudocritical transition temperature, which is very sensitive to the magnetic field (see Chapter 4), still increases with B. The light quark condensate suppression, which is originated by the decreasing of T_0 with B, is insufficient to bring the chiral pseudocritical transition temperature to lower values. Though we might get a sufficient light quark condensate suppression for very low T_0 values, the PNJL model already predicts first-order phase transitions, unlike the crossover transitions seen in LQCD [57].

However, as we saw in Section 4.2, the entanglement interaction [Eq. (3.67)] creates a correlation between both deconfinement and chiral transitions. Therefore, in the EPNJL model, the chiral transition is sensitive to the deconfinement transition, being both pseudocritical temperatures very close, even in the presence of a magnetic field. Setting the deconfinement transition at lower pseudocritical temperatures with increasing B through $T_0(eB)$, the entanglement interaction generates the required light quark condensate suppression leading to a decreasing chiral pseudocritical transition temperature. We can understand this distinct model behavior as follows: in the EPNJL model the scalar coupling G_s^0 is not constant as in PNJL model, but has a dependence on the Polyakov loop value $G_s[\Phi(T)]$; therefore, the $G_s[\Phi(T)]$ decreases because it depends on $T_0(eB)$ and on the temperature. Like the PNJL model, also the EPNJL model predicts a first-order phase transition for a too small T_0 value, even at moderate magnetic field strengths. Anyway, there are indications that a first-order deconfinement phase transition should appear in the high magnetic field limit. Using general arguments, the existence of a Critical End Point in the $T-B$ diagram was proposed in [213]. Recently, it was found strong evidence for a first-order deconfinement phase transition in the asymptotically strong magnetic field limit of QCD, implying the presence of a Critical End Point in the $T-B$ QCD phase diagram [148].

In order to proceed, we fit a magnetic field dependent $T_0(eB)$ using the following generic functional dependence,

$$T_0(eB) = T_0(eB = 0) + \zeta(eB)^2 + \xi(eB)^4 \tag{6.1}$$

to reproduce the pseudocritical temperature of the deconfinement transition [57].

One way to define a pseudocritical temperature for the deconfinement transition is by the peak position of the Polyakov loop susceptibility, which is the definition we use throughout this work. However, as mentioned in Chapter 1, instead of the Polyakov loop, it is also possible to use the strange quark number susceptibility,

$$\chi_s = \frac{T}{V}\frac{\partial^2(\ln Z)}{\partial\mu_s^2},$$

to define a deconfinement pseudocritical temperature, where μ_s is the chemical potential for the strange quarks. The strange quark number susceptibility behaves in a way similar to the Polyakov loop. It was shown in the PNJL model that when the quark mass of the strange quark is large enough, the susceptibility χ_s is proportional to the Polyakov loop, which makes this quantity qualified as an order parameter [28]. Therefore, the inflection point of χ_s gives a pseudocritical temperature consistent with the use of the peak position of the Polyakov loop susceptibility. In the framework of lattice QCD calculations, the strange quark number susceptibility is also a very interesting quantity because no renormalization ambiguities appear [26].

Therefore, we use the strange quark number susceptibility LQCD data of [57] to fit the Eq. (6.1). The pseudocritical deconfinement transition temperature calculated from χ_s at zero magnetic field is 173.9 MeV [57]. This value it compatible with $170(4)(3)$ MeV obtained from the renormalized Polyakov loop [25], where the first error comes from the statistical errors and the second from the scale determination accuracy. Thus, a rescale of the T_0 value to 186 MeV is needed to reproduce the $T_c^\Phi(B=0) = 173.9$ value of LQCD (see Table 6.1). The calculated fit values, ζ and ξ of Eq. (6.1), are in the first line of Table 6.1.

$T_0(eB=0)$ [MeV]	T_c^Φ [MeV]	T_c^χ [MeV]	eB^{max} [GeV^2]	ζ [MeV/GeV^4]	ξ [MeV/GeV^8]
186	173.9	176.0	0.25	-646.491	78.8961
195	177.4	179.9	0.30	-845.467	2813.38
270	214.0	216.0	0.61	-162.632	-545.027

Table 6.1: The pseudocritical temperatures for chiral T_c^χ and deconfinement T_c^Φ transitions for three values of $T_0(B=0)$ within EPNJL model. The eB^{max} is the magnetic field value above which a first-order phase transition sets in. ζ and ξ are fitting parameters of Eq. (6.1)

The $T_0(eB)$ parametrization, which we represent as a blue line in Fig. 6.1, gives rise to a first-order phase transition for $eB > 0.25$ GeV^2. A similar scenario also occurs if we fit $T_0(B)$ to reproduce the upper limit of the pseudocritical deconfinement transition temperature, which is $T_c^\Phi = 177.4$ MeV for $B = 0$ (Fig. 10 of [57]).

This parametrization gives a crossover for $eB \lesssim 0.3$ GeV^2, see Table 6.1 and red line of Fig. 6.1. A larger analytic transition range can be obtained if the quark back-reaction is not accounted for, i.e., if we set $T_0 = 270$ MeV as obtained in pure gauge for $B = 0$, giving $T_c^\Phi = 214$ MeV, 40 MeV higher than the prediction of LQCD data [57]. This parametrization is in the third line of Table 6.1 and is represented by a black line in Fig. 6.1. It reproduces LQCD values for $T_c^\Phi(B)$ [57] shifted by an amount of 40 MeV for magnetic fields up to 0.61 GeV^2, above which a first-order phase transition also occurs.

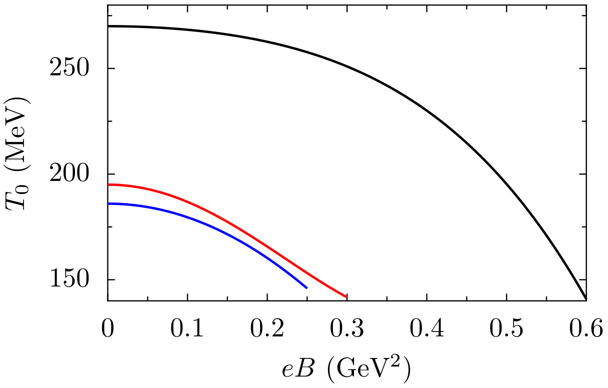

Figure 6.1: T_0 as a function of B, defined by Eq. (6.1), using different values of $T_0(B = 0)$ of Table 6.1: 270 (black line), 195 (red line), and 186 MeV (blue line).

6.1.2 EPNJL model results with $T_0(eB)$

To better illustrate the effect of the $T_0(eB)$ parametrization we use the last scenario of Table 6.1 (i.e., $T_0(eB = 0) = 270$ MeV), because larger magnetic field strengths are attained.

We plot the change of the average light quark condensate, $\Delta(\Sigma_u + \Sigma_d)/2$, as a function of magnetic field in the top panel of Fig. 6.2, up to $eB = 0.61$ GeV^2, for $T = 0$ and several temperatures close to $T_c^\chi(eB = 0)$.

The main conclusions are:

- The qualitative behavior of Fig. 5.2 from LQCD results is reproduced: a monotonic behavior of the condensates as a function of the magnetic field for low temperatures, and a non-monotonic behavior for temperatures around the transition temperature;

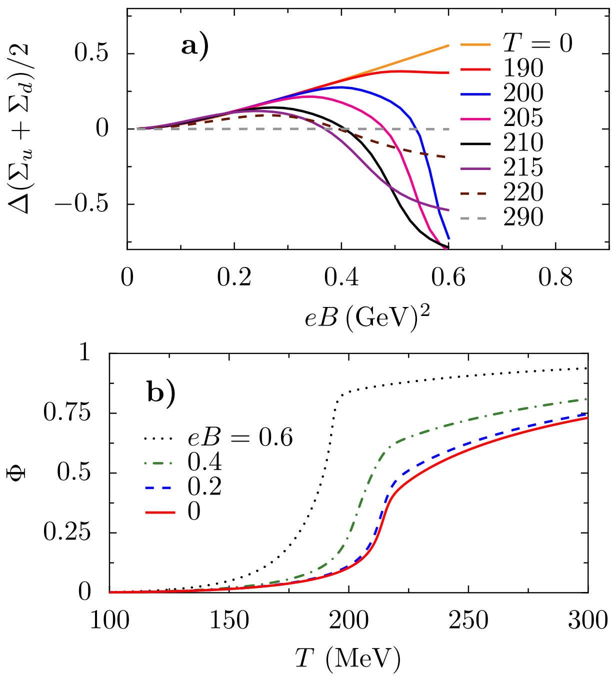

Figure 6.2: The average light quark condensates $\Delta(\Sigma_u + \Sigma_d)/2$ as a function of eB in GeV^2 for several temperatures in MeV (top panel) and and the Polyakov loop as a function of temperature, for different values of eB in GeV^2 (bottom panel) using the EPNJL model with $T_0(B)$ defined in Eq. (6.1).

- The curve for zero temperature has the highest $\Delta(\Sigma_u + \Sigma_d)/2$ values as it happens for LQCD results (see Fig. 5.2);
- The non-monotonic behavior of $\Delta(\Sigma_u + \Sigma_d)/2$ with B for $200 < T < 220$ MeV can only be attributed to the IMC effect; Instead of enhancing, the magnetic field suppresses the quark condensates.
- The $\Delta(\Sigma_u + \Sigma_d)/2$ has negative values for temperatures near 200 MeV. By Eq. (5.1) we see that negative values of $\Delta(\Sigma_u + \Sigma_d)/2$ means $\Sigma_f(0, T) > \Sigma_f(B, T)$: the quark condensate has a lower value in the B presence (the quark condensate is suppressed by B);
- The Polyakov loop behavior shown in the bottom panel of Fig. 6.2 follows the same trend predicted by the LQCD [58]: for a given temperature it increases with B and presents a stiffer variation at the transition region. From the bottom panel of the figure is also clear that the transition region moves to smaller values of T.

Similar results are obtained if the $T_0(eB = 0)$ includes the quark back-reaction (i.e.

the first and second lines of Table 6.1), however, in a smaller magnetic field intensity range, if we restrict the chiral and deconfinement transitions to a crossover nature.

We plot in Fig. 6.3 the pseudocritical temperature for both the deconfinement (dashed lines) and the chiral (dotted line) transitions, for the three scenarios of $T_0(eB=0)$ shown in Table 6.1: 270 MeV (black), 195 MeV (red), and 186 MeV (blue). In agreement with LQCD [57, 60], both pseudocritical temperatures decrease with increasing magnetic field.

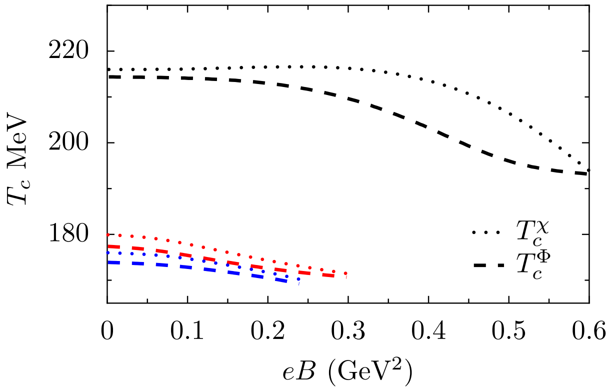

Figure 6.3: EPNJL results with $T_0(B)$ defined in Eq. (6.1): pseudo-critical temperatures as a function of B, for different values of $T_0(B)$ presented in Table 6.1: 270 MeV (black), 195 MeV (red), and 186 MeV (blue).

6.2 A magnetic field dependent coupling

In [214] it is shown that there is a strong screening effect of the gluon interactions in the region of low momenta, relevant for chiral symmetry breaking. In [155, 156], the IMC mechanism is attributed to the combination of gluon screening effects and the weakening of the strong coupling.

In the NJL model the quarks interact through local current-current coupling. In the QCD vacuum the color fields propagate in a small region (~ 0.2 fm), corresponding to a characteristic momentum scale $\Lambda \sim 1$ GeV. In perturbative QCD, a non-local interaction between two quark color currents generates the non-local one-gluon exchange interaction between quarks. For temperatures around the pseudocritical temperature (~ 200 MeV) the strong screening effects experienced by the gluons cannot be handled perturbatively. Restricting the color interaction to a short distance scale Λ^{-1}, larger than the typical quark momentum scale, the non-local interaction between quarks can be approximated by a local coupling G between their color currents. This effective coupling $G \sim \bar{g}^2\Lambda^{-2}$ encodes the QCD coupling g averaged over the relevant distance scale, in combination with the square correlation length Λ^{-2} [215]. The gluon degrees of freedom were absorbed into the four-quark interaction. Therefore, if the QCD coupling is affected by the presence of an external magnetic field, it should be reflected in the four-quark interaction coupling G_s^0 of the NJL model.

6.2.1 Parametrization of the $G_s(eB)$ in the NJL model

The way the QCD coupling α_s is related to the scale $\sqrt{|eB|}$ in leading-order and for sufficiently strong magnetic fields ($eB \gg \Lambda_{QCD}^2$) is investigated in [214] and is given by

$$\alpha_s(eB) \sim \frac{1}{b \ln \frac{|eB|}{\Lambda_{QCD}^2}}, \tag{6.2}$$

where $b = (11N_c - 2N_f)/12\pi = 27/12\pi$, and the energy scale $\sqrt{|eB|}$ is fixed only up to a factor of order 1 [214].

To analyze the effect of a magnetic field running coupling in the NJL model, we use, as a first step, the simple *ansatz*

$$G_s(eB) = G_s^0 / \ln\left(e + |eB|/\Lambda_{QCD}^2\right). \tag{6.3}$$

The high magnetic field limit ($B \to \infty$) gives a zero coupling constant ($G_s \to 0$), and in the opposite limit, i.e., for zero magnetic field ($B \to 0$), we get $G_s = G_s^0$. The magnetic field weakens the NJL coupling; thus, we have $G_s(eB) < G_s^0$ at any B strength, and in the zero magnetic field limit the usual NJL model parametrization value G_s^0 is recovered.

The chiral normalized pseudocritical temperatures are given in Fig. 6.4, for $G_s = G_s^0$ (the normal NJL model) and $G_s(eB)$. When we use $G_s = G_s^0$, the model predicts an increasing $T_c^\chi/T_c^\chi(eB = 0)$ for all range of magnetic fields, as we saw in the previous Chapter. With $G_s(eB)$ defined by Eq. (6.3), the $T_c^\chi/T_c^\chi(eB = 0)$ decreases for low magnetic fields ($eB < 0.3$ GeV^2), though much faster than LQCD, and increases for higher B values. The $T_c^\chi/T_c^\chi(eB = 0)$ decreasing dependence with B arises from the IMC effect. Thus, with this simple *ansatz*, the model predicts a decreasing pseudocritical transition temperature due to the IMC mechanism at low B. Anyway, the logarithm dependence of the running coupling $\alpha_s(p^2)$ of QCD is valid for high momentum transfers $p \gg 1$ GeV. Therefore, the $\alpha_s(eB) \propto \ln(|eB|/\Lambda_{QCD}^2)^{-1}$

dependence may not be suitable for the low magnetic field range ($eB < 1$ GeV^2).

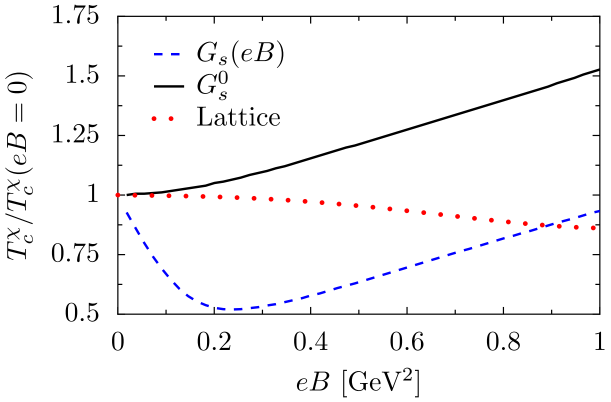

Figure 6.4: The normalized pseudocritical temperatures of the chiral transition ($T_c^\chi(eB=0) = 178$ MeV for the NJL model) as a function of B: in the NJL model with a magnetic field dependent coupling $G_s(eB)$ (blue dashed line), with a constant coupling G_s^0 (black solid line), and the lattice results (red dots) [57].

Since there is no LQCD data available for $\alpha_s(eB)$, we use another strategy: we fit $G_s(eB)$ to reproduce the normalized pseudocritical temperature of the chiral transition $T_c^\chi(B)/T_c^\chi(eB=0)$ (we are reproducing the temperature decrease ratio) obtained in LQCD calculations [57]. The resulting fit function of $G_s(eB)$ is shown in Fig. 6.5 and has the following functional dependence:

$$G_s(\zeta) = G_s^0 \left(\frac{1 + a\,\zeta^2 + b\,\zeta^3}{1 + c\,\zeta^2 + d\,\zeta^4} \right) \tag{6.4}$$

where $a = 0.0108805$, $b = -1.0133 \times 10^{-4}$, $c = 0.02228$, $d = 1.84558 \times 10^{-4}$, and $\zeta = eB/\Lambda_{QCD}^2$. We have used $\Lambda_{QCD} = 300$ MeV. The chiral pseudocritical transition temperature as a function of the magnetic field is shown in Fig. 6.6. The parametrization $G_s(eB)$ was obtained using the LQCD results [57] for the chiral pseudocritical transition temperatures in the range $0 < eB < 1$ GeV^2. From asymptotic freedom we expect that as $B \to \infty$ we have $G_s(eB) \to 0$. The above polynomial form ensures that G_s goes as $1/eB$ for $B \to \infty$.

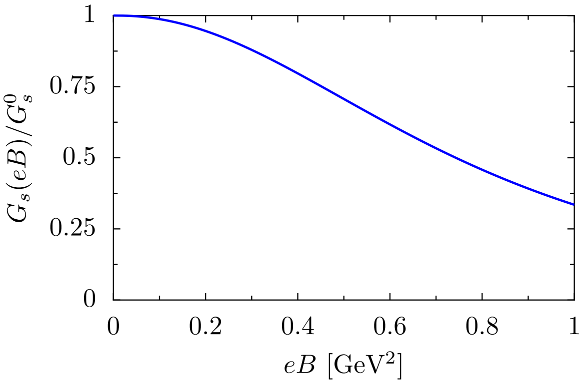

Figure 6.5: The fitted $G_s(eB)$ dependence [Eq. (6.4)] calculated in the NJL model that reproduces LQCD normalized chiral pseudocritical transition temperature [57] shown in Fig. 6.6.

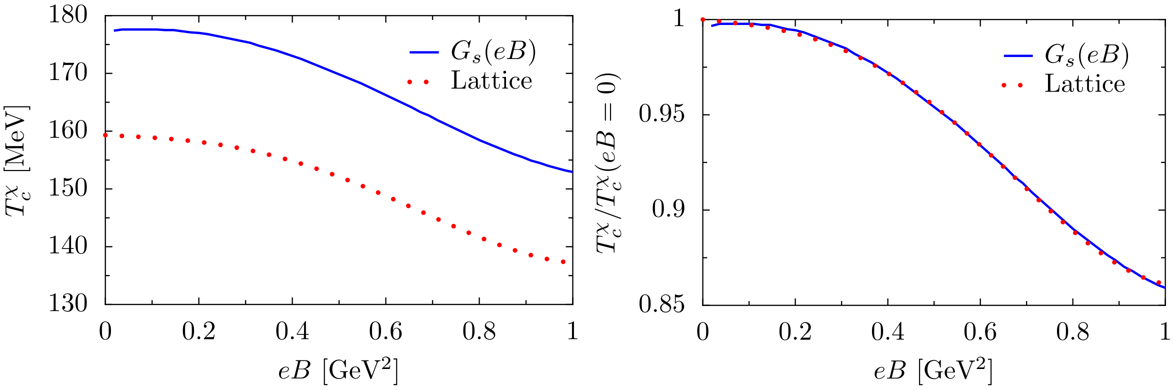

Figure 6.6: The chiral pseudocritical transition temperature in the NJL model with the $G_s(eB)$ dependence [Eq. (6.4)] (blue line) and the LQCD result [57] on the left panel, and the respective normalized chiral pseudocritical transition temperature on the right.

6.2.2 NJL model results with $G_s(eB)$

The behavior of the quark condensates with the magnetic field within the NJL model is shown in Figs. 6.7-6.10.

Figure 6.7 shows $\Delta(\Sigma_u+\Sigma_d)/2$ as a function of B for several temperatures, with $G_s(eB)$ defined in Eq. (6.4) (top panel) and $G_s=G_s^0$ (bottom panel). The $\Delta(\Sigma_u+\Sigma_d)/2$ calculated with $G_s(eB)$ shows the same behavior as LQCD calculations: at low and high temperatures the magnetic field enhances the condensates (MC effect), but at temperatures near the pseudocritical chiral transition temperature it suppresses the condensates. For $G_s=G_s^0$ case, MC is predicted at any temperature.

The same conclusions are obtained from Fig. 6.8, where the average of the light

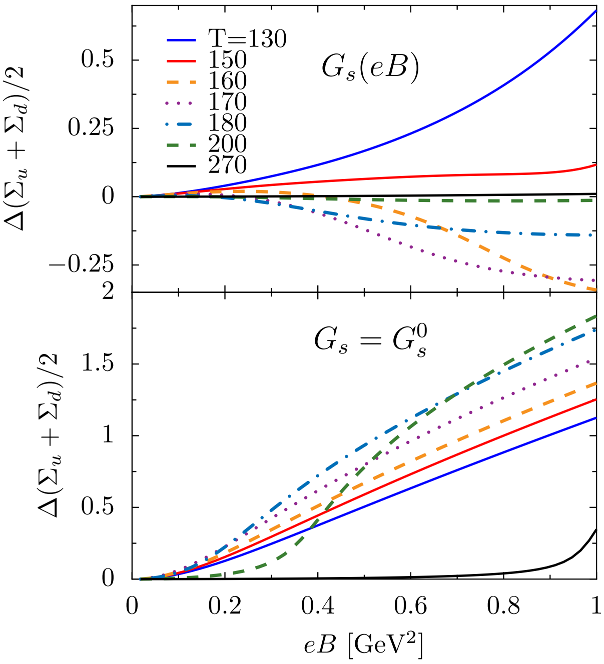

Figure 6.7: The NJL model light chiral condensate change $\Delta(\Sigma_u+\Sigma_d)/2$ as a function of B, for several values of temperature in MeV, with the magnetic field dependent coupling $G_s(eB)$ (top panel), and with a constant coupling G_s^0 (bottom panel).

quark condensate is plotted as function of T for several values of B. The lattice results extracted from [57] have also been included in the top panel, together with the results obtained with $G_s(eB)$ from Eq. (6.4). The overall behavior is reproduced by the NJL model with the $G_s(eB)$. A very different result is obtained with a constant coupling G_s^0 (see bottom panel of Fig. 6.8), where the transition occurs for larger temperatures with increasing B.

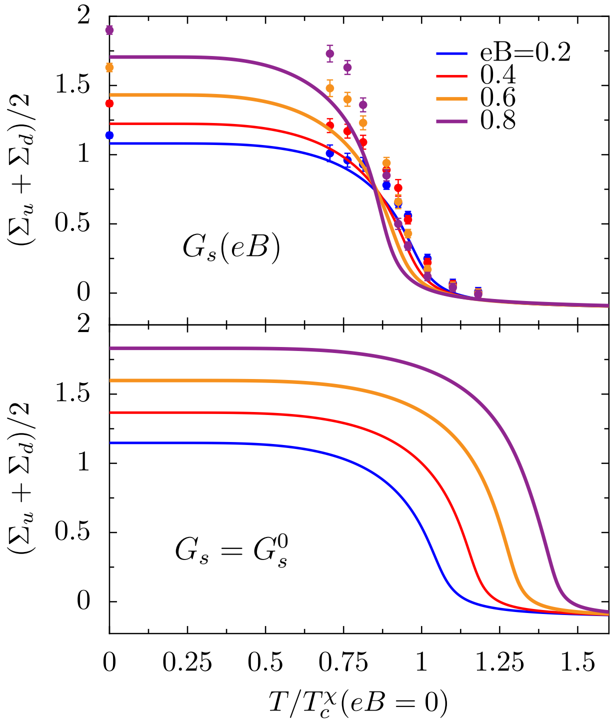

Figure 6.8: The light chiral condensate average $(\Sigma_u + \Sigma_d)/2$ as a function of temperature for several values of eB in GeV^2 in the NJL model, with a magnetic field dependent coupling $G_s(eB)$ from Eq. (6.4) compared with LQCD results [57] (top panel), and a constant coupling G_s^0 (bottom panel). The LQCD data was normalized by $T_c^\chi(eB=0) = 160$ MeV [57] and the NJL model results by $T_c^\chi(eB=0) = 178$ MeV.

In Figs. 6.9 and 6.10 the difference between the light quark condensates is plotted as a function of temperature for several values of B, and as a function of B for several temperatures, respectively. The lattice results from [57] are also included in the top panel of Fig. 6.9 together with the results for the $G_s(eB)$ case. For comparison, we also show the results for $G_s = G_s^0$ in the bottom panel of Fig. 6.9.

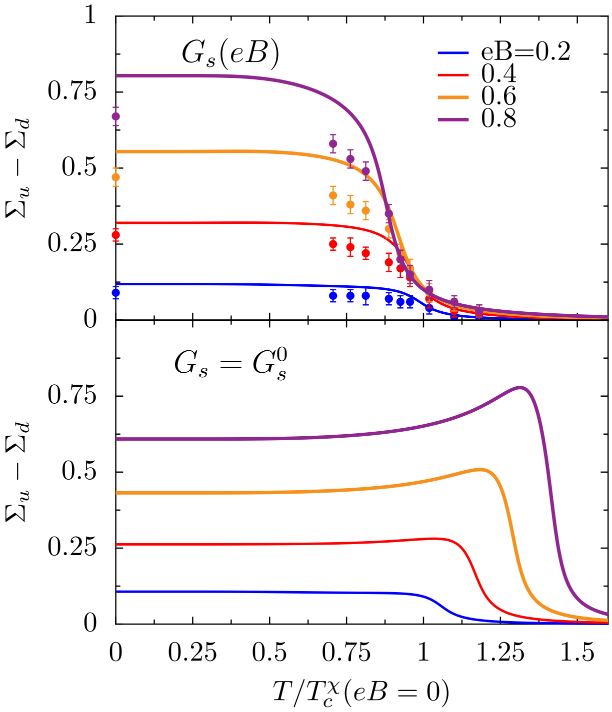

Figure 6.9: The chiral condensate difference $\Sigma_u - \Sigma_d$ as a function of temperature, for several values of eB in GeV^2, in the NJL model, calculated with a magnetic field dependent coupling $G_s(eB)$ [Eq. (6.4)] compared with LQCD results [57] (top panel), and a constant coupling G_s^0 (bottom panel). The LQCD data was normalized by $T_c^\chi(eB=0) = 160$ MeV [57] and the NJL model results by $T_c^\chi(eB=0) = 178$ MeV.

The bumps present in curves for the $G_s = G_s^0$ case (bottom panel of Fig. 6.9) around the transition temperatures do not appear when $G_s(eB)$ is used (top panel of Fig. 6.9), where a reasonable agreement with the LQCD results is achieved. As we saw in the previous Chapter, these bumps result of a stronger MC effect on the u-quark, due to its larger electric charge (the larger the magnetic field the larger the difference between u- and d-condensates, and the respective chiral transition temperatures), being this feature particularly strong close to the transition temperature, where the curves for stronger fields have a larger bump. When $G_s = G_s(eB)$, the partial restoration of chiral symmetry mechanism prevails over the MC, due to a weaker interaction, and the bumps will disappear in accordance with LQCD results. The $\Sigma_u - \Sigma_d$ value in the top panel of Fig. 6.9 always decreases with the temperature for any B.

The condensate difference $\Sigma_u - \Sigma_d$ is plotted as a function of B for several temperatures in Fig. 6.10. The larger electric charge of the u-quark makes the difference $\Sigma_u - \Sigma_d$ always positive (i.e. $\Sigma_u > \Sigma_d$) for any temperature and B. As the temperature increases, due to the restoration of chiral symmetry, the values of the constituent light quark masses approximate their current values of $m_u = m_d = 5.5$ MeV; thus, for a fixed value of B, the $\Sigma_u - \Sigma_d$ is a decreasing function of temperature. Therefore, at higher temperatures, e.g., $T = 270$ MeV (solid black line), the $\Sigma_u - \Sigma_d$ is low due to the partial restoration of the chiral symmetry. The IMC effect is also seen for $T = 160$ MeV (dashed orange line) and $T = 170$ MeV (dotted purple line). A non-monotonic behavior with B arises, being the inflection point for $T = 160$ MeV at higher B than for $T = 170$ MeV: this reflects in a decrease of the chiral pseudocritical transition temperature with B.

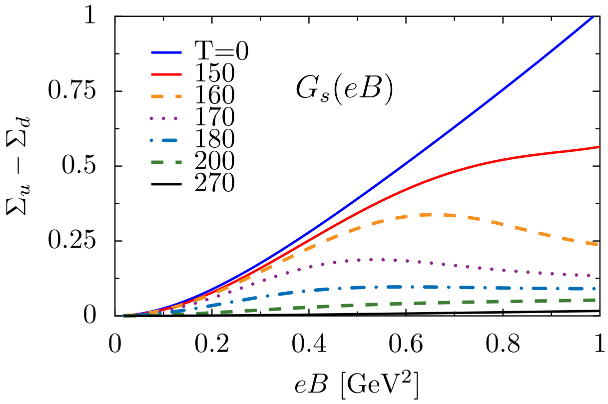

Figure 6.10: The NJL chiral condensate difference $\Sigma_u - \Sigma_d$ as a function of eB for several values of temperature in MeV with a magnetic field dependent coupling $G_s(eB)$ [Eq. (6.4)].

We next analyze the $T - B$ phase diagram obtained within the NJL with the magnetic field dependent coupling. The calculated chiral pseudocritical transition temperature is shown in Fig. 6.11 for a range of magnetic field intensities larger than the one used in the fit.

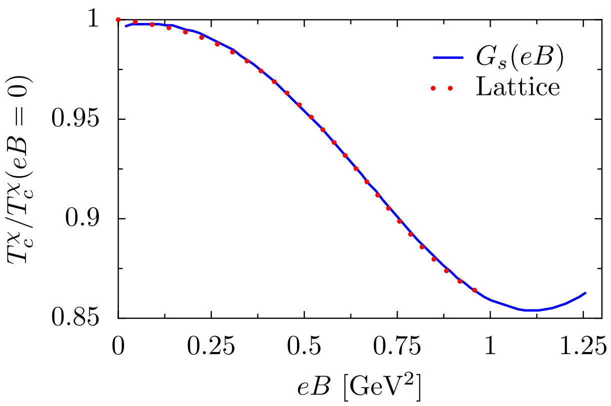

Figure 6.11: The normalized pseudocritical temperature of the chiral transition as a function of eB in the NJL model, with the magnetic field dependent coupling $G_s(eB)$ [Eq. (6.4)] (blue line) and LQCD results (red dots) [57].

For $eB \approx 1.1$ GeV^2, the pseudocritical temperature starts to increase with B. This behavior was also obtained by some LQCD calculations [61], which predict that the MC effect is dominant at high values of B. A chiral first-order phase transition appears for $eB \approx 1.25$ GeV^2 . The LQCD as well as the NJL results from Fig. 6.8 show that the average chiral condensate slope increases with increasing magnetic field. Thus, if this behavior persists for higher magnetic field strengths, it is expected from the LQCD results that the transition turns into a first-order at some critical B; therefore, a Critical End Point is expected in the $T-B$ diagram [148, 213].

6.2.3 PNJL model results with $G_s(eB)$

In the present section, we consider the PNJL model. As we already said, in the PNJL model the quark degrees of freedom are coupled to a Polyakov loop field which allows us to study the deconfinement transition at finite temperature. Several studies about the deconfinement and chiral symmetry restoration of hot QCD matter in the presence of an external magnetic field have recently been made [101, 105, 106]. Now, we will take for the scalar coupling the same magnetic field dependent parametrization $G_s(eB)$ obtained in the previous section [Eq. (6.4)]. Next, we will discuss the effect of the magnetic field on the Polyakov loop and on the quark condensates .

It should be remembered that in this model, besides the chiral point-like coupling between quarks, the gluon dynamics is reduced to a simple static background field, represented by the Polyakov loop. As referred in Section 3.4, we set the parameter T_0 in the Polyakov loop as 210 MeV, which takes into account the quark back-reaction and reproduces a deconfinement pseudocritical temperature of 171

MeV.

In Fig. 6.12 we plot both the chiral and the deconfinement pseudocritical transition temperatures as a function of B. Both T_c^χ and T_c^Φ are decreasing functions of B as in LQCD [57]. Due to the existing coupling in the PNJL model between the Polyakov loop field and the quarks, the $G_s(eB)$ affects both the chiral and the deconfinement transitions. Both pseudocritical temperatures have a very similar dependence on B. The gap between them can be reduced by increasing the T_0 value of the Polyakov potential or using the EPNJL model.

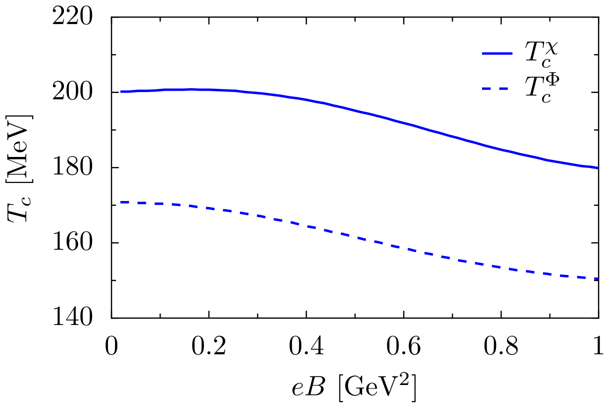

Figure 6.12: The chiral and deconfinement transitions temperatures as a function of B in the PNJL, using the magnetic field dependent coupling $G_s(eB)$ [Eq. (6.4)].

The effect of the magnetic field on the Polyakov loop is clear in Fig. 6.13, where we plot Φ as a function of the magnetic field intensity for different values of the temperature (left panel), and as a function of temperature for several magnetic field strengths (right panel).

For example, at $T = 150$ MeV (red line in the left panel) the Polyakov loop value increases with B, i.e., the deconfinement transition is shifted to lower temperature due to the magnetic field. This can be confirmed by the displacement of the inflection point of the Polyakov loop (right panel) towards lower temperatures with increasing B. The suppression of the condensates induced by the magnetic field dependence of the coupling $G_s(eB)$ translates into an increase of the Polyakov loop. The effect of the magnetic field on Φ is stronger for temperatures in the respective crossover transition region (see left panel of Fig. 6.13), showing the same behavior as LQCD results [58].

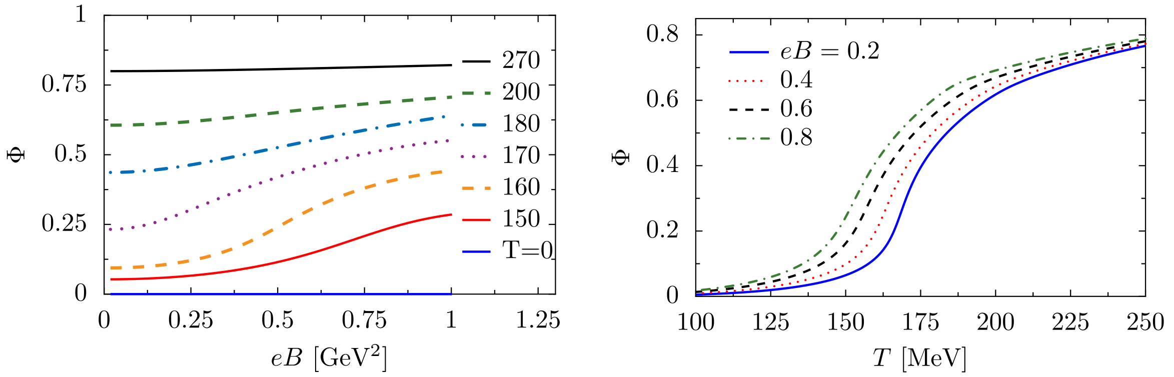

Figure 6.13: The value of the Polyakov loop as a function of B for several values of T in MeV (left panel) and as a function of T for several values of B in GeV^2 (right panel).

We plot the change of the average chiral condensate $\Delta(\Sigma_u + \Sigma_d)/2$ as a function of B for several temperatures in Fig. 6.14. As in the LQCD [57], the model gives a non-monotonic behavior with B for temperatures near the transition temperature and a monotonous increase for lower and higher temperatures.

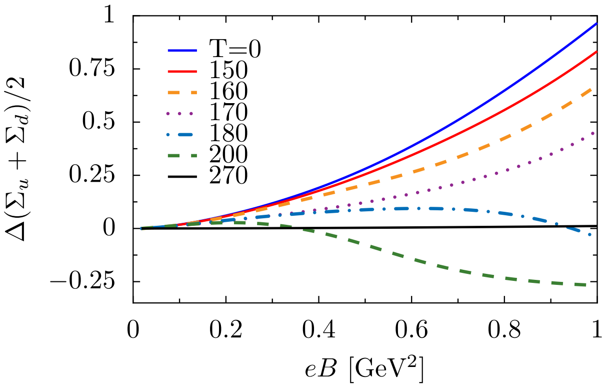

Figure 6.14: The light chiral condensate $\Delta(\Sigma_u+\Sigma_d)/2$ as a function of eB, for several values of temperature in MeV, in the PNJL model.

In Fig. 6.15, both the $(\Sigma_u + \Sigma_d)/2$ (top panel) and the $\Sigma_u - \Sigma_d$ (bottom panel) are plotted as a function of the temperature, normalized by the pseudocritical temperature at zero magnetic field, for several magnetic field strengths, and compared with the LQCD results [57]. Just as already obtained for NJL model, the general behavior of the LQCD results are reproduced.

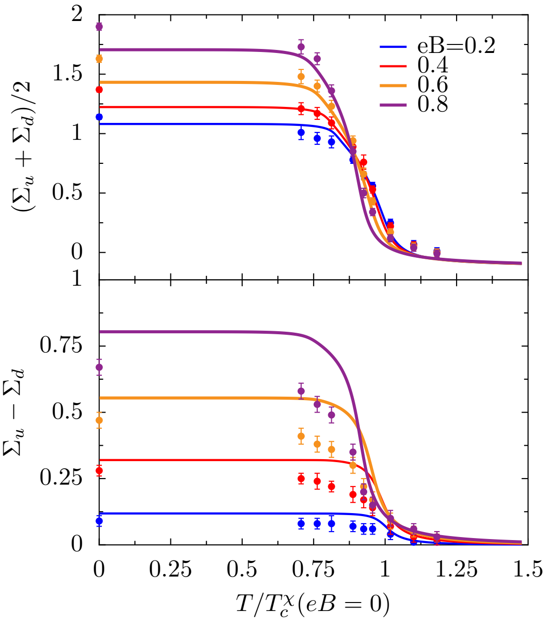

Figure 6.15: The average $(\Sigma_u + \Sigma_d)/2$ (top panel) and the difference $(\Sigma_u - \Sigma_d)$ (bottom panel) of the light chiral condensates as a function of temperature, for several values of eB in GeV^2, and the LQCD results [57]. The LQCD data was normalized by $T_c^{\chi}(eB = 0) = 160$ MeV [57] and the PNJL model results by $T_c^{\chi}(eB = 0) = 200$ MeV.

We observe that a $SU(3)$ symmetry of the point-like effective interactions between quarks is assumed in the magnetic background. However, it is expected that the electromagnetic field breaks this symmetry, and, in fact, the comparison with the LQCD results for $\Sigma_u - \Sigma_d$ (in bottom panel of Fig. 6.15) suggests that the up quark interaction is depleted with respect to down quark. That seems reasonable as the effect of the magnetic field on the up quark is larger than in the down quark, and therefore the interaction between the up quarks should become weaker with respect to the down quarks as the magnetic field increases.

6.3 Comparison between the two approaches

An effective Polyakov potential that depends on the magnetic field, through the parameter $T_0(eB)$, could describe the IMC effect only within the EPNJL model, as we saw in Section 6.1. Neither the PNJL model nor the two-flavor thermal quark-meson model [116] were able to reproduce the IMC effect with a T_0 dependence on the magnetic field. These results are in accordance with the ones of the Section 6.2: the coupling G_s, which in the EPNJL model depends on the Polyakov loop, becomes weaker at the crossover transition region, where the Polyakov loop increases. This is shown in the top panel of Fig. 6.16, where the coupling $G_s[\Phi(T)]$ of Section 6.1 is plotted for several temperatures (dashed curves) and, for comparison, the parametrization $G_s(eB)$ [Eq. (6.4)] is also included (solid black line). It is interesting to realize that in the range $eB < 0.6$ GeV^2, the curve obtained for $T = 210$ MeV (blue dashed line), which is close to the deconfinement pseudocritical transition temperature $T_c^\Phi = 214$ MeV at $T_0(B = 0) = 270$ MeV (see Table 6.1), behaves in accordance with the results of the $G_s(eB)$ parametrization (solid black line). No IMC effect was obtained within the PNJL model because the parameter $T_0(eB)$ does not affect the coupling G_s.

In Fig. 6.16 we compare the pseudocritical transition temperatures as a function of B (middle panel) and the Polyakov loop as a function of $T/T_c^\Phi(eB = 0)$ (bottom panel) for the $G_s(eB)$ (solid lines) and $T_0(eB)$ (dashed lines) parametrizations.

The pseudocritical transition temperatures for $G_s(eB)$ have a smoother decrease with B, reflecting the B dependence of G_s instead of the B and T dependences of $G_s(\Phi)$ (see top panel of Fig. 6.16). Furthermore, the difference between the chiral and the deconfinement pseudocritical transitions temperatures is almost constant with B for $G_s(eB)$, and much larger than for $T_0(eB)$. Because the entanglement interaction couples the Polyakov loop and the quark condensates, the coincidence of T_c^χ and T_c^Φ at $B = 0$ disappears, but they approximate again at $eB = 0.61$ GeV^2 due to the emergence of a first-order phase transition (see top panel of Fig. 6.16). The PNJL model predicts crossover transitions for this magnetic field range, and thus the $G_s(eB)$ coupling does not change its normal behavior of predicting different temperatures for T_c^χ and T_c^Φ. The Polyakov loop behavior with the temperature (bottom panel) shows two main differences. For $T_0(eB)$ in the EPNJL model, the variation of Φ is much more intense and the stronger deconfinement transition for $eB = 0.6$ GeV^2 is signaling the emergence of a first-order phase transition for larger B values. Furthermore, the inflection point of the Polyakov loop moves to much lower values for $T_0(eB)$ (dashed lines) than $G_s(eB)$ (solid lines), and thus a bigger decrease of T_c^Φ with B is obtained for $T_0(eB)$ (see middle panel).

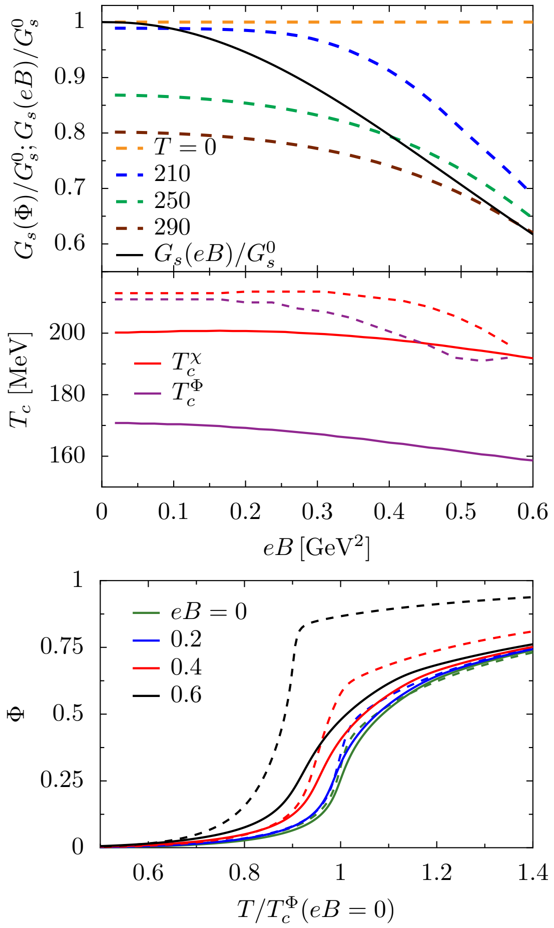

Figure 6.16: Comparison between $G_s(eB)$ (full lines) and $T_0(eB)$ (dashed lines). Top panel: The scalar coupling G_s versus the magnetic field, the black full line is the parametrization defined in [Eq. (6.4)] and plotted in Fig. 6.5; middle panel: the chiral and deconfinement pseudocritical transition temperatures versus the magnetic field; bottom panel: the Polyakov loop versus the temperature normalized by the deconfinement pseudocritical transition temperature T_c^Φ for $B = 0$, respectively, 171 MeV (PNJL with $G_s(eB)$) and 214 MeV (EPNJL with $T_0(eB)$).

6.4 The strange quark transition

In this section, using the $G_s(eB)$ parametrization calculated in the previous section, we focus on its effect on the strange quark transition. We plot the quark condensates and their susceptibilities in Fig. 6.17. All pseudocritical transition temperatures plotted in Fig. 6.18 decrease with B. Looking at the condensates behavior (top panel of Fig. 6.17), we see that all of them are enhanced at low temperatures and suppressed at temperatures near the transition temperature. Also the first peaks in the susceptibilities, induced by the deconfinement transition, are shifted to lower temperatures with increasing B (see bottom panel of Fig. 6.17).

Just as in Section 4.3, we define the same two criteria to calculate the pseudocritical transition temperatures:

Criterion I: the temperature T_c^i at which the inflection point of the quark condensate $\langle\bar{q}_i q_i\rangle$ occurs (which is the definition that we have been using):

$$\left.\frac{\partial^2\langle\bar{q}_i q_i\rangle(B,T)}{\partial T^2}\right|_{T=T_c^i} = 0;$$

Criterion II: the temperature T_c^i at which the quark condensate is half of its zero temperature value $\langle\bar{q}_i q_i\rangle(B,0)$:

$$\langle\bar{q}_i q_i\rangle(B,T_c^i) = 0.5\langle\bar{q}_i q_i\rangle(B,0).$$

We show in the bottom panel of Fig. 6.17 a zoom of the strange transition region. Even though we are using the magnetic field dependent coupling $G_s(eB)$, and thus the light quark susceptibilities peaks are moving to lower temperature values (see Fig. 6.17), the strange quark transition, which is reflected on the third peak of its susceptibility, is also washed out for $eB > 0.58$ GeV^2. Anyway, for $eB < 0.58$, we clearly see in the zoom of Fig. 6.17 that the inflection point moves to lower temperatures, i.e., the T_c^s decreases with B. For $eB > 0.58$, we use the second criterion (dashed lines) to define a pseudocritical temperature for the strange quark transition.

All the pseudocritical transition temperatures T_c^i are plotted in Fig. 6.18. For each T_c^i, both criteria show similar dependence with B. The T_c^Φ has the biggest gap between both criteria and is the only pseudocritical temperature that shows higher values for the second criterion (dashed lines). We see from Fig. 6.18 that the strange quark pseudocritical transition temperature (solid and dashed green lines) is the one that decreases the most with B.

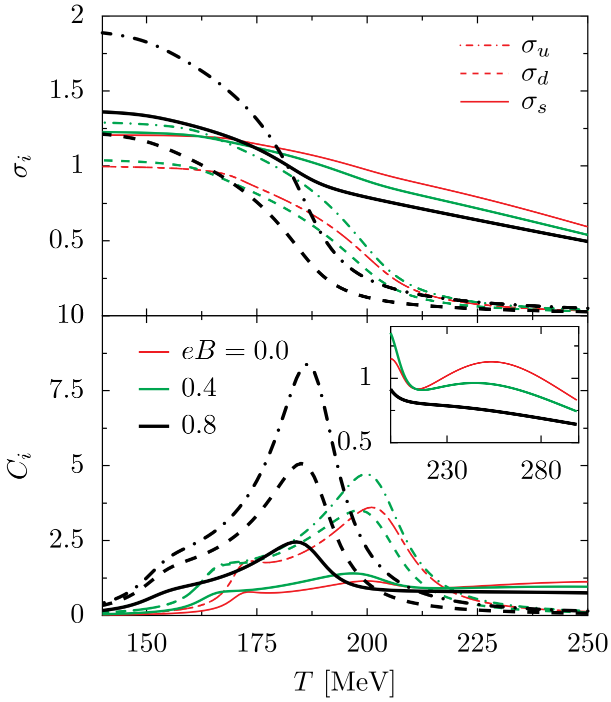

Figure 6.17: The quark condensates and their susceptibilities as a function of temperature for $eB = 0.0, 0.4$ and 0.8 GeV^2, using $G_s(eB)$.

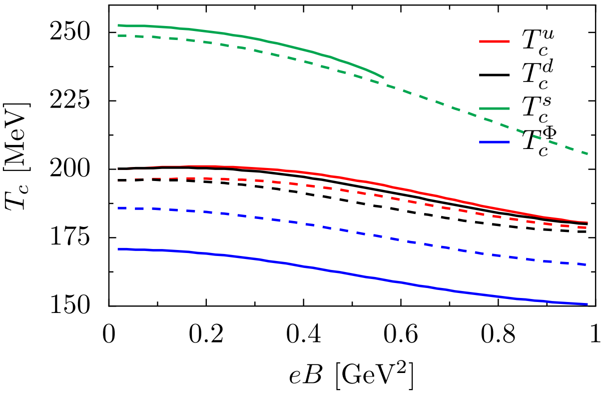

Figure 6.18: The critical temperatures T_c^i as a function of B, given by the peak of the susceptibilities (solid lines) and half the vacuum value of the order parameters (dashed lines), using $G_s(eB)$.

It is important to notice that the IMC effect is strongly influenced by the 't Hooft term. Indeed, in Fig. 6.19 the up, down, and strange quark condensates normalized to their values at zero magnetic field are plotted for $G_s(eB)$ case, in three different scenarios:

i) with the 't Hooft term ($K \neq 0$) (top panel);

ii) without the 't Hooft term ($K = 0$), but no refitting of the couplings in order to reproduce the vacuum properties of the pion and kaon (middle panel);

iii) without the 't Hooft term ($K = 0$), and using the parametrization proposed in [216], which reproduces the pion and kaon properties (bottom panel).

Just like the up and down quarks, the strange quark also shows the IMC effect (solid lines in top panel of Fig. 6.19). The strange quark condensate presents a non-monotonic behavior as a function of B, and thus its pseudocritical transition temperature is a decreasing function of B (solid and dashed green lines of Fig. 6.18). This behavior is not following the trend indicated in [60], where the strange quark condensate is said to increase with growing B for all temperatures. When we turn off the 't Hooft term (middle panel), the strange quark (solid lines) still undergoes IMC; furthermore, the pattern does not change much when compared with the $K = 0$ case (top panel). This can be understand as follows. Due to its larger current mass, the flavor mixing effect does not affect much its pseudocritical transition temperature, when compared with the up and down quarks for $G_s = G_s^0$ (see Fig 4.12 of Section 4.3). Therefore, it is expected that this feature persists even when one uses $G_s(eB)$, but now the T_c^s is a decreasing function of B.

For the light quarks, as we saw in Fig 4.12 of Section 4.3, the gap between T_c^u and T_c^d increases substantially for $K = 0$, being T_c^u bigger due to its larger electric charge. Now, using the $G_s(eB)$ and $K = 0$, the down quark will feel the IMC at lower temperatures than the up quark (see dashed lines in middle panel): for $T = 250$ MeV (green lines) the down quark undergoes IMC as the up quark is already feeling the MC effect again, i.e., for the up quark the IMC effect occurs at a higher temperature region than for the down quark.

The results of the bottom panel of Fig. 6.19 were also obtained excluding the 't Hooft term, but using a different parametrization that describes the vacuum properties of the pion and kaon [216]. The general behavior is similar to the results shown in the middle panel although the up quark shows a behavior closer to the upper panel, where the 't Hooft term was included. This is due to the larger mass of the up quark, within this parametrization [216], that compensates the effect of the strong magnetic field due to its larger charge.

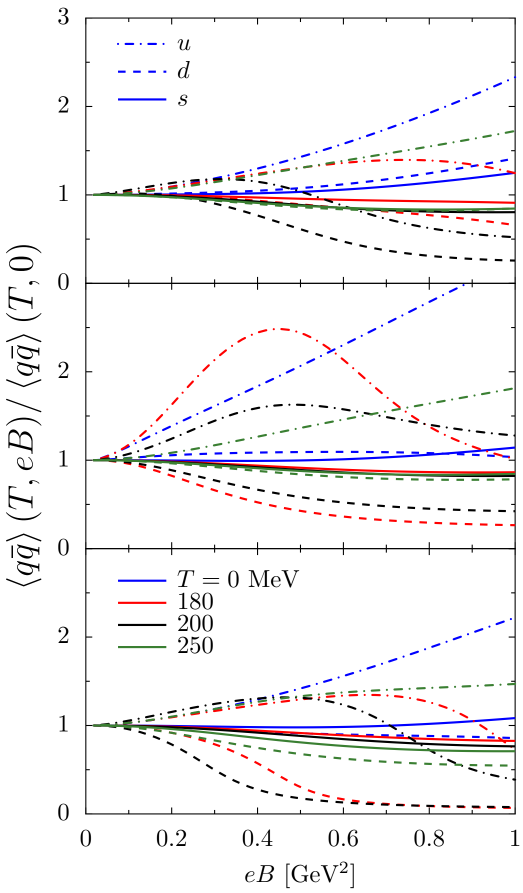

Figure 6.19: The ratios of the u, d and s condensates, $\langle q_i\bar{q}_i\rangle(T,eB)/\langle q_i\bar{q}_i\rangle(T,0)$, as a function of eB, for several values of T [0 (blue lines), 180 (red lines), 200 (black lines) and 250 (green lines) MeV] using $G_s(eB)$: including the 't Hooft term (upper panel), excluding the 't Hooft term without refitting the other parameters (middle panel), and excluding the 't Hooft term and using the parametrization of Ref. [216] (bottom panel).

It is worth pointing out that the behavior of the strange quark condensate is somehow expectable. On one hand, being the strange quark the one with larger current mass, it does not feel a strong MC effect for weak fields. Moreover, its charge is half of the up quark charge, and, therefore, it is also not as affected by the magnetic field as the up quark. On the other hand, the IMC effect is implemented in the present model through a parametrization of the scalar coupling, and, consequently, it is switched on as soon as $B > 0$. From these two effects, it results that the strange quark also feels the IMC effect. This is clearly seen by switching off the 't Hooft term, where no mixing with the up quark occurs, and the strange condensate still decreases for low B, even for $T = 0$ (blue solid line in the middle panel of Fig. 6.19).

6.5 Thermodynamical quantities

Finally, in this section we calculate for different scenarios the following thermodynamical quantities: the pressure $P(T, B)$ [Eq. (4.6)], the energy density $\mathcal{E}$ [Eq. (4.8)], the interaction measure $\Delta = (\mathcal{E} - 3P)/T^4$ [Eq. (4.9)], the speed of sound squared v_s^2 [Eq. (4.10)], and the specific heat C_V [Eq. (4.11)].

In Figs. 6.20-6.21 we plot these quantities for a magnetic field $eB = 0.3$ GeV^2 (the order of the maximal magnetic field strength for the LHC [54]) for three scenarios:

- In the left panel of Fig. 6.20 the 't Hooft term is included ($K \neq 0$) and the constant scalar coupling G_s^0 is used;
- In the right panel of Fig. 6.20 the 't Hooft term is included ($K \neq 0$) and the magnetic dependent scalar coupling $G_s(eB)$ is used;
- In Fig. 6.21 the 't Hooft term is excluded ($K = 0$) and the constant scalar coupling G_s^0 is used.

The vertical lines in Fig. 6.20 indicate the position of the maximum of the quark susceptibilities for the PNJL with the 't Hooft term and with the constant scalar coupling G_s^0.

As discussed before, comparing both Figs. 6.20 and 6.21, we see that the 't Hooft term pushes the deconfinement and the chiral transition temperatures to larger temperatures. Moreover, due to the flavor mixing effect, the up and down quarks susceptibilities maximum coincide approximately when we include the 't Hooft term (Fig. 6.20), but occur at quite different temperatures without the 't Hooft term (Fig. 6.21).

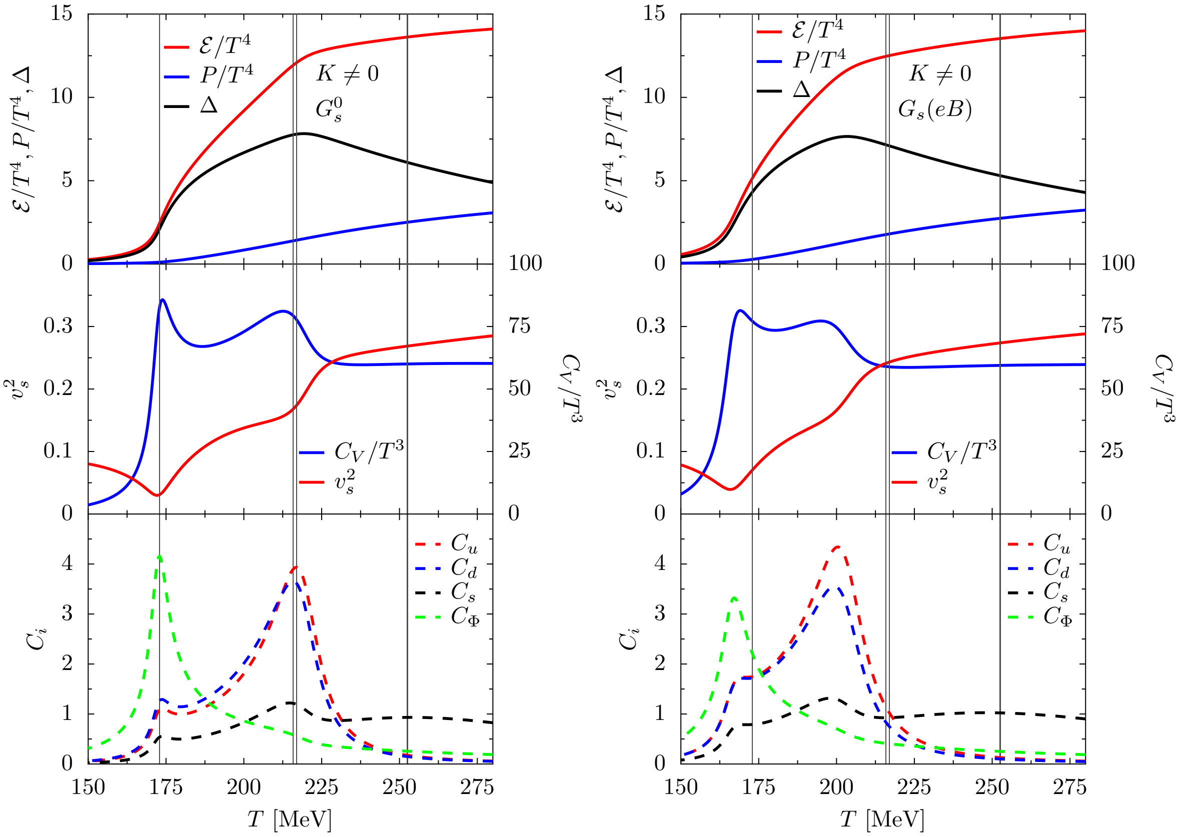

Figure 6.20: The following thermodynamical quantities using the PNJL model with the 't Hooft term, for $G_s = G_s^0$ (left panel) and $G_s = G_s(eB)$ (right panel), for $eB = 0.3$ GeV^2: the scaled energy density $\mathcal{E}/T^4$, the interaction measure $\Delta = (\mathcal{E} - 3P)/T^4$, and the scaled pressure P/T^4 as a function of temperature T (top panel); the scaled specific heat C_V/T^3, and speed of sound squared v_s^2 (middle panel); and the quark susceptibilities C_i (bottom panel) as a function of temperature T. The vertical lines indicate the position of the maximum of the quark susceptibilities for the $G_s = G_s^0$ case.

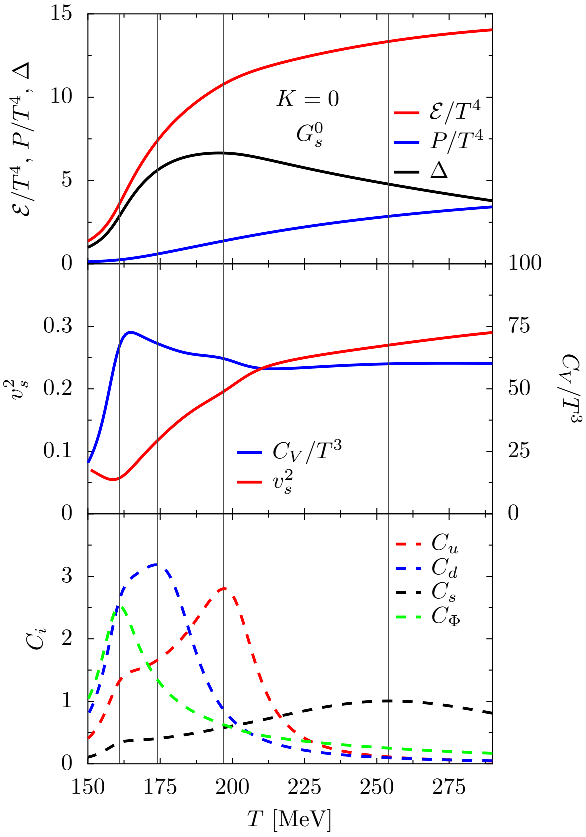

Figure 6.21: The following thermodynamical quantities using the PNJL model without the 't Hooft term and $G_s = G_s^0$ for $eB = 0.3$ GeV^2: the scaled energy density $\mathcal{E}/T^4$, the interaction measure $\Delta = (\mathcal{E} - 3P)/T^4$, and the scaled pressure P/T^4 as a function of temperature T (top panel); the scaled specific heat C_V/T^3, and speed of sound squared v_s^2 (middle panel); and the quark susceptibilities C_i (bottom panel) as a function of temperature T. The vertical lines indicate the position of the maximum of the quark susceptibilities.

For the three different scenarios considered it is seen that the scaled pressure (blue line), the energy density (red line), and thus the interaction measure (black line) in top panels are continuous functions of the temperature as expected due to the crossover transition. There is a sharp increase in the vicinity of the deconfinement pseudocritical transition temperature and then a tendency to saturate at the corresponding ideal gas limit. Excluding the 't Hooft term (Fig. 6.21) makes all curves smoother. The sharper increase occurs at lower temperatures if a magnetic field dependent coupling $G_s(eB)$ (right panel of Fig. 6.20) is considered because the pseudocritical transition temperatures are pushed to lower values.

The middle panels of Figs. 6.20-6.21 show the specific heat C_V/T^3 (blue line) and the speed of sound squared v_s^2 (red line) as a function of the temperature. The specific heat presents two peaks caused by the distinct pseudocritical temperatures of deconfinement and chiral transitions. Again, the effect of $G_s(eB)$ that pushes the peaks to lower temperatures is clearly seen. Moreover, there is a larger superposition between the Polyakov loop and both up and down quark susceptibilities and less pronounced peaks are observed. Due to the absence of the flavor mixing effect, the pseudocritical transition temperatures for the up and down quark are different, and thus the second peak that corresponds to the chiral transition is almost washed out when the 't Hooft term is excluded (Fig. 6.21).

The speed of sound squared v_s^2 passes through a local minimum around the deconfinement pseudocritical transition temperature and reaches the limit of $1/3$ (Stefan-Boltzmann limit) at high temperature. The minimum indicates the fast change in the quark masses. A second inflection occurs at the chiral pseudocritical transition temperature. As expected from the previous discussion, both features are more pronounced within the PNJL with 't Hooft term and a constant scalar coupling (Figs. 6.20 and 6.21). For the magnetic field considered ($eB = 0.3$ GeV^2), the peak of the strange quark susceptibility has no effect on the represented thermodynamical quantities, showing that the influence of the light quark sector is predominant over the strange quark one because the restoration of the chiral symmetry already happened in the light quark sector.

6.6 Conclusions

We have started this Chapter by summarizing several studies that connect the IMC effect to the weakening of the QCD running coupling in the presence of an external magnetic field. We have developed two mechanisms that incorporate into NJL-type models, through the model coupling and the free parameter of the Polyakov potential T_0, the back-reaction of the magnetized quarks on the gauge fields, and investigate if IMC could be reproduced.

Deconfinement is taken into account in the E/PNJL models by an effective gluon potential that describes a constant gauge field background on which quarks propagate. The Polyakov potential is fitted to reproduce thermodynamic lattice data of pure gauge theory [184]. The only free parameter of the Polyakov potential is the T_0 value that sets the onset of deconfinement for pure gauge theory, which is a first-order phase transition at $T_0 = 270$ MeV. In the E/PNJL models the T_0 value must be rescale to match the pseudocritical temperature of the deconfinement transition of LQCD. Then, to mimic the back-reaction of the gluon sector to the presence of an external magnetic field, we have introduced a magnetic field dependent $T_0(B)$, which reproduces the correct LQCD deconfinement transition temperatures in the magnetic field presence. Within the EPNJL model the IMC effect was reproduced. Although, the crossover nature of the transitions was only reproduced up to a maximum magnetic field strength, above which a first-order phase transition occurs. The IMC effect was reproduced in the EPNJL model but not in the PNJL model. While the scalar coupling G_s^0 is constant in PNJL model, it depends on the Polyakov loop value $G_s[\Phi(T)]$ in the EPNJL model; therefore, the $G_s[\Phi(T)]$ decreases because it depends on $T_0(eB)$ and on the temperature.

In the E/P/NJL models, the gluon degrees of freedom are absorbed into the four-quark interaction term; thus, the effective NJL scalar coupling G_s^0 encodes the QCD coupling averaged over the relevant distance scale. Therefore, if the QCD coupling is affected by the presence of an external magnetic field, it should be reflected in the four-quark interaction coupling G_s^0 of the NJL model. Then, we have directly introduced a magnetic field dependence on the scalar coupling G_s^0 that mimics the weakening of the strong coupling in the magnetic field presence. We have fitted the $G_s(eB)$ dependence to reproduce the normalized pseudocritical temperatures of the chiral transition $T_c^\chi(B)/T_c^\chi(eB=0)$ (the temperature decrease ratio) obtained in LQCD calculations [57]. The difference and average light quark condensates as a function of temperature for several magnetic field strengths obtained within the PNJL model shows similar behavior as in LQCD [57]. Furthermore, also the Polyakov loop follows the same trend given by LQCD [58]: it increases with B for a given temperature, making the pseudocritical deconfinement temperature a decreasing function of the magnetic field intensity.

Chapter 7

QCD Phase Diagram in an external magnetic field

In this Chapter, we will extend our study to finite baryon chemical potential analyzing the effect of an external magnetic field on several quark matter phase diagram scenarios. The influence of strong external magnetic fields on the structure of the QCD phase diagram is also very important because it can have relevant consequences on measurements in heavy-ion collisions at very high energies [54, 217, 218].

There are several aspects that can influence the location of the Critical-End-Point (CEP) like the strangeness or isospin content of the in-medium or the presence of an external magnetic field [106]. Indeed, in Ref. [78], within the NJL model, it was verified that the size of the first-order phase transition segment of the transition line expands with increasing B in such a way that the CEP becomes located at higher temperature and smaller chemical potential values. This was also verified by using the Ginzburg-Landau effective action formalism with the renormalized quark-meson model [117]. Due to its relevance for the understanding of the QCD phase diagram, we discuss how the CEP's location in the $T - \mu_B$ phase diagram changes with isospin asymmetry, and confirm previous results obtained within other models, showing it might not exist at sufficiently high isospin asymmetry [29, 219, 220]. We also consider the strangeness effect in the QCD phase diagram, analyzing different chemical equilibrium conditions.

Finally, we study the impact of the $G_s(eB)$ parametrization [Eq. (6.4)], calculated in the previous Chapter, on CEP's location.

7.1 Location of the CEP

We are going to discuss several scenarios that can influence the location of the CEP by starting to choose different values of isospin and strangeness chemical potentials. Let us denote the chemical potentials of strangeness by μ_S, of charge by μ_Q, and baryon number by μ_B, for a positive unit charge of strangeness, electric, and baryon, respectively. The chemical potential of a particle i with baryon B_i, electric Q_i, and strangeness S_i charges is [33]

$$\mu_i = B_i \mu_B + Q_i \mu_Q + S_i \mu_S.$$

The quark chemical potentials μ_i are written as a function of μ_S, μ_Q, and μ_B by

$$\mu_u = \frac{1}{3}\mu_B + \frac{2}{3}\mu_Q, \tag{7.1}$$

$$\mu_d = \frac{1}{3}\mu_B - \frac{1}{3}\mu_Q, \tag{7.2}$$

$$\mu_s = \frac{1}{3}\mu_B - \frac{1}{3}\mu_Q - \mu_S. \tag{7.3}$$

The baryonic and charge densities are respectively

$$\rho_B = \sum_i B_i \rho_i = \frac{1}{3}(\rho_u + \rho_d + \rho_s) \tag{7.4}$$

$$\rho_Q = \sum_i Q_i \rho_i = \frac{1}{3}(2\rho_u - \rho_d - \rho_s) - \rho_e, \tag{7.5}$$

where ρ_e is the electron density.

For zero temperature a first-order chiral phase transition is obtained at some μ_B^{crit}. As the temperature increases the first-order phase transition persists up to the CEP. At the CEP, the chiral phase transition becomes a second-order one. Along the line of a first-order phase transition the thermodynamic potential has two degenerate minima, which are separated by a finite potential barrier making the potential non-convex. The height of the barrier decreases as the temperature increases and disappears at the CEP. Again, this pattern is characteristic of a first-order phase transition: the two minima correspond, respectively, to the phases of broken and restored symmetry [191].

7.1.1 Without external magnetic field

To figure out the effect of the Polyakov loop on the CEP's location, we calculate the temperature, baryonic chemical potential, and baryonic density at the CEP for both

NJL and PNJL models.

With the definitions of Eqs. (7.1)-(7.3), we can introduce different quark matter scenarios that we analyze within both models:

- zero charge ($\mu_Q = 0$), or zero isospin chemical potential ($\mu_I = 0$), and zero strangeness chemical potential ($\mu_S = 0$). In terms of quark chemical potentials becomes $\mu_u = \mu_d = \mu_s$;
- zero charge ($\mu_Q = 0$), or zero isospin chemical potential ($\mu_I = 0$), and strangeness chemical potential of $\mu_S = \frac{1}{3}\mu_B$. In terms of quark chemical potentials becomes $\mu_u = \mu_d$ and $\mu_s = 0$;
- symmetric quark matter with equal amount of u, d, and s quarks ($\rho_u = \rho_d = \rho_s$), also known as strange quark matter;
- β-equilibrium matter (assuming neutrino escape): $\mu_u - \mu_d = \mu_Q = -\mu_e$ and $\mu_d = \mu_s$ ($\mu_S = 0$).

The four different scenarios results are plotted in Fig. 7.1, and the respective CEP values are given in Table 7.1.

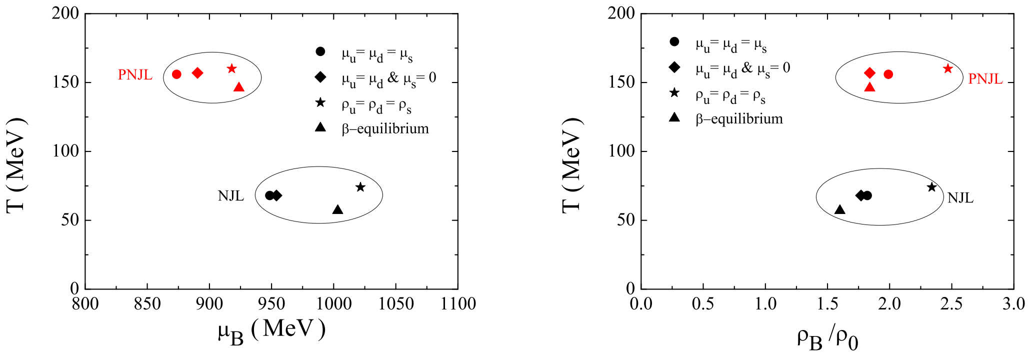

Figure 7.1: The CEP's location on a $T - \mu_B$ diagram (left) and $T - \rho_B$ (right) (in units of nuclear saturation density $\rho_0 = 0.16$ fm^{-3}) under the four scenarios considered: all quark chemical potentials equal (circle), the strange quark chemical potential equal to zero (diamond), all quark densities equal (star), and $\beta-$equilibrium condition (triangle) within NJL and PNJL models. No external magnetic field is considered.

As already discussed in [191, 202, 203], the Polyakov loop (i.e., in the PNJL model) shifts the CEP to higher temperatures (T^{CEP}), more than two times higher (see

Table 7.1) than in the NJL model, and slightly smaller baryonic chemical potentials (μ_B^{CEP}), or, slightly higher baryonic densities (ρ_B^{CEP}). The CEP's location in $\beta-$equilibrium quark matter occurs for one of the largest chemical potentials, only slightly below the one obtained for strange quark matter. However, it is interesting to see that for $\beta-$equilibrium, the CEP occurs at lower temperatures. The reason becomes clear when analyzing the right panel of Fig. 7.1: the $\beta-$equilibrium quark matter being more asymmetric is less bound and, therefore, the transition to a chirally symmetric phase occurs at a smaller temperature and density than for the symmetric case.

	NJL			PNJL		
	T^{CEP} [MeV]	μ_B^{CEP} [MeV]	$\rho_B^{\text{CEP}}/\rho_0$	T^{CEP} [MeV]	μ_B^{CEP} [MeV]	$\rho_B^{\text{CEP}}/\rho_0$
$\mu_u = \mu_d = \mu_s$	68	949	1.82	155	874	1.98
$\mu_u = \mu_d$; $\mu_s = 0$	68	954	1.77	157	890	1.84
$\rho_u = \rho_d = \rho_s$	74	1022	2.34	160	918	2.47
$\beta-$equilibrium	57	1003	1.60	146	924	1.84

Table 7.1: The temperature T^{CEP}, baryonic chemical potential μ_B^{CEP}, and baryonic density ρ_B^{CEP} at CEP, for the NJL and the PNJL models. The baryonic density is in nuclear saturation density units, $\rho_0 = 0.16$ fm^{-3}.

From Fig. 7.1 and Table 7.1 we see that for $\beta-$equilibrium matter the CEP occurs at larger baryonic chemical potentials and smaller temperatures. Being the only scenario that breaks the isospin symmetry, we conclude that the CEP's location depends on the isospin μ_I value. In the following, we analyze the effect of isospin asymmetry $|\mu_u - \mu_d| = |\mu_I| = |\mu_Q|$ in our system and focus our discussion on the PNJL model.

To study in a more systematic way the effect of the isospin μ_I on CEP, we take the strange quark chemical potential equal to zero ($\mu_s = 0$) and increase systematically μ_d with respect to μ_u. We are interested in the d-quark rich matter as it occurs in HIC and neutron stars: isospin asymmetry presently attained in HIC corresponds to $\mu_u < \mu_d < 1.1\mu_u$, and neutron matter has $\mu_d \sim 1.2\mu_u$. Larger isospin asymmetries are also possible in π^- rich matter [40, 220].

In Fig. 7.2, we calculate the CEP's location as a function of isospin asymmetry $|\mu_I| = |\mu_u - \mu_d|$. For reference, we also plot the CEP for $\mu_u = \mu_d = \mu_s$ by a red circle. The corresponding quark densities ρ_u and ρ_d are given Table 7.2. With increasing isospin asymmetry the CEP moves to smaller temperatures and larger baryonic chemical potentials (it can be understood by the same arguments as previously given for $\beta-$equilibrium case). Eventually, for quark matter with large enough asymmetry, the CEP disappears from the phase diagram. This threshold value corresponds to $\mu_d \simeq 1.45\mu_u$ and is represented in the figure by a star, at $T = 0$. This scenario corresponds to $|\mu_u - \mu_d| = |\mu_I| = |\mu_Q| = 130$ MeV, below the pion mass and, therefore, no pion condensation occurs under these conditions. The effect of pion condensation on the QCD phase diagram for finite chemical potentials has recently been discussed in [220–222]. We remark that, as pointed out in [29], where the effect of isospin on the QCD phase diagram has also been discussed, a larger isospin chemical potential corresponds to smaller baryonic chemical potential due to the definition of the baryonic chemical potential: the study was performed within the two-flavor quark-meson model and the relation $\mu_B = 3\mu_q = \frac{3}{2}(\mu_u + \mu_d)$ was used [29]; in the present work, from Eqs. (7.1)-(7.3), we have $\mu_B = \mu_u + 2\mu_d$. Therefore, in both works, the T^{CEP} decreases when the isospin asymmetry increases.

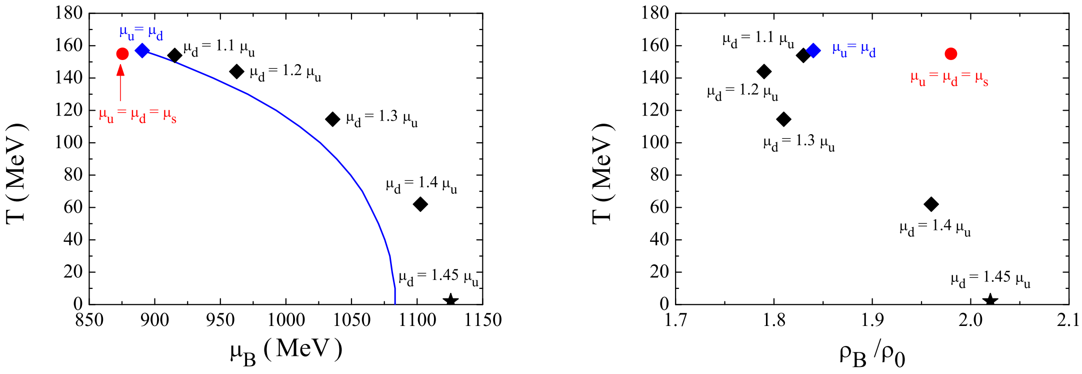

Figure 7.2: PNJL model results for CEP's location in a temperature T versus baryonic potential μ_B (left panel) and temperature T versus baryonic density ρ_B (right panel) diagrams, for several isospin chemical potential $\mu_I = |\mu_u - \mu_d|$ values. The full line is the first-order phase transition line for zero isospin matter ($\mu_d = \mu_u$, $\mu_s = 0$). The strange chemical potential is set to zero, $\mu_s = 0$. There is no CEP for $\mu_d > 1.45\mu_u$. The baryonic density is in nuclear saturation density units, $\rho_0 = 0.16$ fm^{-3}.

The right panel of Fig. 7.2 shows CEP's location in temperature T versus baryonic density ρ_B diagram. For $\mu_u < \mu_d < 1.2\mu_u$, the baryonic density of CEP decreases with asymmetry, but for $\mu_d \gtrsim 1.2\mu_u$, the opposite occurs, and at the threshold ($\mu_d = 1.45\mu_u$) $\rho_B \sim 1.91\rho_0$ the CEP disappears (see Table 7.2).

CEP	$T^{\rm CEP}$ [MeV]	$\mu_B^{\rm CEP}$ [MeV]	$\rho_B^{\rm CEP}/\rho_0$	$\rho_u^{\rm CEP}/\rho_B$	$\rho_d^{\rm CEP}/\rho_B$
$\mu_d = \mu_u$	157	890	1.84	1.50	1.50
$\mu_d = 1.1\mu_u$	154	915	1.83	1.28	1.72
$\mu_d = 1.2\mu_u$	144	962	1.79	1.04	1.96
$\mu_d = 1.3\mu_u$	115	1035	1.81	0.75	2.25
$\mu_d = 1.4\mu_u$	62	1103	1.96	0.50	2.50
$\mu_d = 1.45\mu_u$	~ 0	1126	2.02	0.39	2.61

Table 7.2: The temperature $T^{\rm CEP}$, baryonic chemical potential $\mu_B^{\rm CEP}$, baryonic density $\rho_B^{\rm CEP}$, and light quark densities ($\rho_u^{\rm CEP}$ and $\rho_d^{\rm CEP}$) at CEPs, for different ratio μ_d/μ_u scenarios, with $\mu_s = 0$ ($\rho_s = 0$). The baryonic and quark densities are in nuclear saturation density units, $\rho_0 = 0.16$ fm^{-3}.

7.1.2 With an external magnetic field

In the following, we focus on how the magnetic field affects the CEP's location, for symmetric quark matter: $\mu_u = \mu_d = \mu_s$.

The obtained $T - \mu_B$ phase diagram is presented in the left panel of Fig. 7.3 and shows a trend very similar to that of the results previously obtained for the NJL in [78]: as the intensity of the magnetic field increases, the temperature at which the CEP occurs ($T^{\rm CEP}$) increases monotonically (see Fig. 7.3 right panel) and the corresponding baryonic chemical potential ($\mu_B^{\rm CEP}$) decreases until the critical value $eB \sim 0.4$ GeV^2 is reached; for stronger magnetic fields both $T^{\rm CEP}$ and $\mu_B^{\rm CEP}$ increase. In the middle panel of Fig. 7.3 the CEP is given in a T versus baryonic density ρ_B/ρ_0 plot, and it can be seen that the $\rho_B^{\rm CEP}$ always increases as the magnetic field increases from 0 to 1 GeV^2.

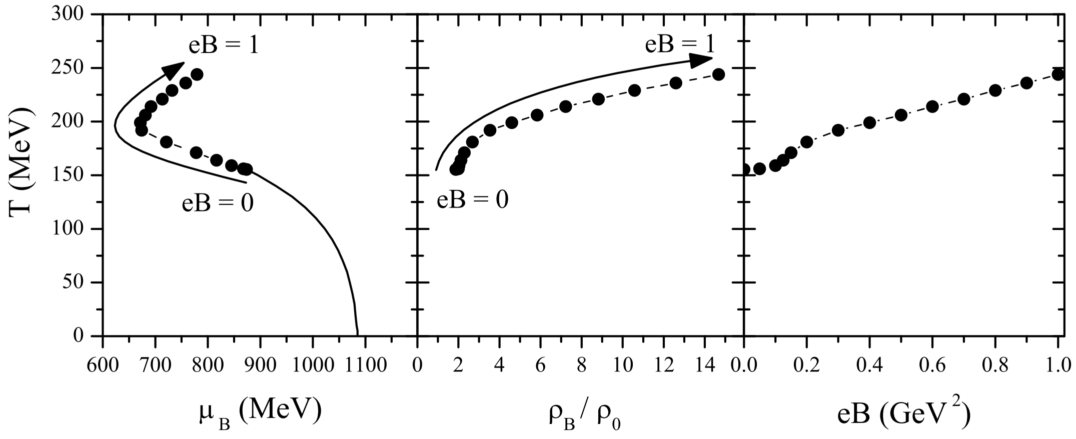

Figure 7.3: Location of the CEP on a diagram T vs the baryonic chemical potential μ_B (left panel), vs the baryonic density ρ_B (middle panel), and vs magnetic field eB (right panel)

To understand these behaviors at finite density we start by considering the case at $T = 0$ where a first-order phase transition takes place. In the left panel of Fig. 7.4, we present the critical chemical potential (μ_B^{crit}) at which the first-order phase transition occurs. The pattern followed by μ_B^{crit} at $T = 0$ in the PNJL model is similar, although for smaller values, to the one reported in [78] at $T = 1$ MeV and also at higher temperatures: a slow decrease for $0 < eB < 0.06$ GeV^2, a faster decrease until $0.12 - 0.18$ GeV^2 and a monotonically increase afterwards. We verify a lowering of μ_B^{crit} with B until $eB = 0.25$ GeV^2. The slow decrease in μ_B^{crit} for increasing magnetic field strength in the range $0 \leq eB \lesssim 0.08$ GeV^2 is followed by a faster decrease for $0.08 \lesssim eB \lesssim 0.25$ GeV^2. Stronger field strengths result in a monotonically increasing of μ_B^{crit}. This change in behavior corresponds to the point where just one Landau level (LL) is filled for each flavor in the partially chiral restored phase. Indeed, the stronger the magnetic field, the larger the spacing between the levels.

At $T = \mu_B = 0$ a stronger magnetic field results in an increase of the mass of the quarks (the increase is larger for M_u than M_d due to the difference in electric charges). At finite density, however, μ_B^{crit} starts to decrease with increasing magnetic fields, indicating an easier transition to the partially chiral restored phase [129]. This result was already seen in [78]. For eB above 0.25 GeV^2, μ_B^{crit} increases.

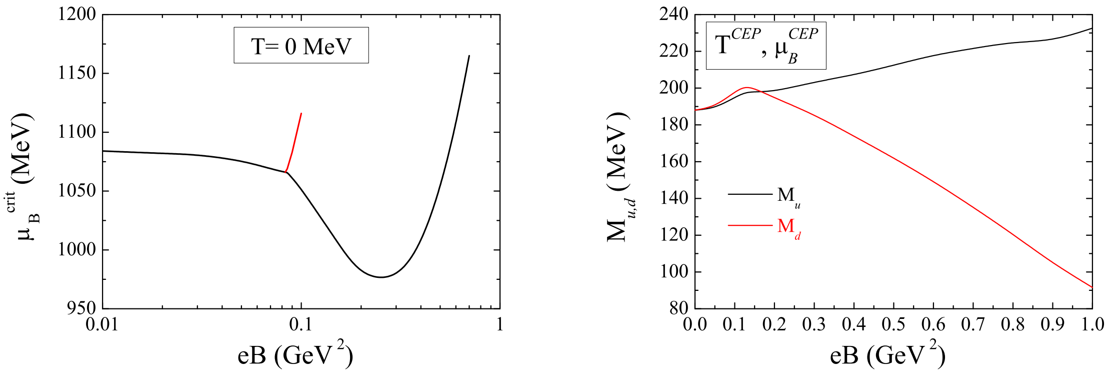

Figure 7.4: The critical chemical potential μ_B^{crit} at $T = 0$ MeV versus the magnetic field (left panel) and the up, and down quarks effective masses at the CEP (right panel) as a function of the magnetic field intensity.

Also noteworthy to point out is the existence of a range of magnetic fields, $0.083 \lesssim eB \lesssim 0.1$ GeV^2, where at least two first-order phase transitions occur (see left panel of Fig. 7.4[1]), in accordance with what was found in the two-flavor [82, 84] and three-flavor NJL models [86]. This cascade of transitions will result in the existence of multiple CEPs at finite temperature. The CEP on which we focus most of our attention in the present and next sections is the one that subsists to the highest temperature.

As was discussed above, in the weak magnetic field regime, an increasing magnetic field results in a smaller μ_B^{crit} for the first-order transition at $T = 0$, even if the quarks masses have already started to increase. As this corresponds to a shift of the first-order transition line towards a smaller chemical potential, the observed decrease in μ_B^{CEP} follows naturally. This effect is dominant over that of the increase of the quark masses at the CEP (both quark masses at the CEP increase with magnetic field strength for $eB \lesssim 0.125$ GeV^2) which should hinder the first-order partial chiral restoration (see right panel of Fig. 7.4). A similar behavior is also obtained within the NJL model used in [78].

Above a critical strength for the magnetic fields, $eB \gtrsim 0.125$ GeV^2, there is a clear asymmetry in the CEP quark mass response to an increasing magnetic field strength: a strong decrease in M_d as opposed to the smooth increase in M_u (due to the charge difference the $d-$quark coupling to the magnetic field is weaker). This behavior is accompanied by an increase of the baryonic density at which the CEP

---

[1] Around $eB \approx 0.085$ GeV^2 a small third phase transition (not visible on Fig. 7.4) can be found on a very small range.

occurs (right panel of Fig. 7.3).

For stronger magnetic fields ($eB \gtrsim 0.4$ GeV^2) both $T^{\rm CEP}$ and $\mu_B^{\rm CEP}$ increase (see left panel of Fig. 7.3). This can be understood as a result of a decreasing number of occupied LL due to the large intensity of the field and the greater difficulty in restoring chiral symmetry.

In the following, we focus on how the magnetic field affects the CEP's location, for two quark matter scenarios:

- isospin symmetric quark matter ($\mu_u = \mu_d$ and $\mu_s = 0$);
- isospin asymmetric quark matter ($\mu_d = 1.45\mu_u$ and $\mu_s = 0$):

The obtained results are in Table 7.3 and Fig. 7.5. For reference, we also show the results for symmetric quark matter ($\mu_u = \mu_d = \mu_s$) obtained above. Figure 7.5 shows the results in a temperature versus baryonic chemical potential diagram (top panel), temperature versus baryonic density (middle panel), and the quark density fractions ρ_i versus baryonic density ρ_B (bottom panel) for several magnetic field strength values, within the three scenarios above.

	$\mu_u = \mu_d = \mu_s$			$\mu_u = \mu_d$; $\mu_s = 0$		
eB [GeV^2]	$T^{\rm CEP}$ [MeV]	$\mu_B^{\rm CEP}$ [MeV]	$\rho_B^{\rm CEP}/\rho_0$	$T^{\rm CEP}$ [MeV]	$\mu_B^{\rm CEP}$ [MeV]	$\rho_B^{\rm CEP}/\rho_0$
0.0	155	874	1.98	157	890	1.84
0.1	159	845	2.03	160	867	1.85
0.2	181	721	2.68	183	741	2.40
0.3	192	674	3.54	194	692	3.13
0.4	199	672	4.60	202	684	4.01
0.5	206	681	5.83	210	688	5.02
0.6	214	692	7.22	217	708	6.15
0.7	221	713	8.81	225	726	7.37
0.8	229	732	10.58	234	740	8.63
0.9	236	758	12.59	243	755	10.00
1.0	244	779	14.67	253	763	11.38

Table 7.3: The temperature, baryonic chemical potential and density at the CEPs for different values of the magnetic field and two different scenarios: $\mu_u = \mu_d = \mu_s$ and $\mu_u = \mu_d$, $\mu_s = 0$. The baryonic density is given in terms of the saturation density $\rho_0 = 0.16$ fm^{-3}.

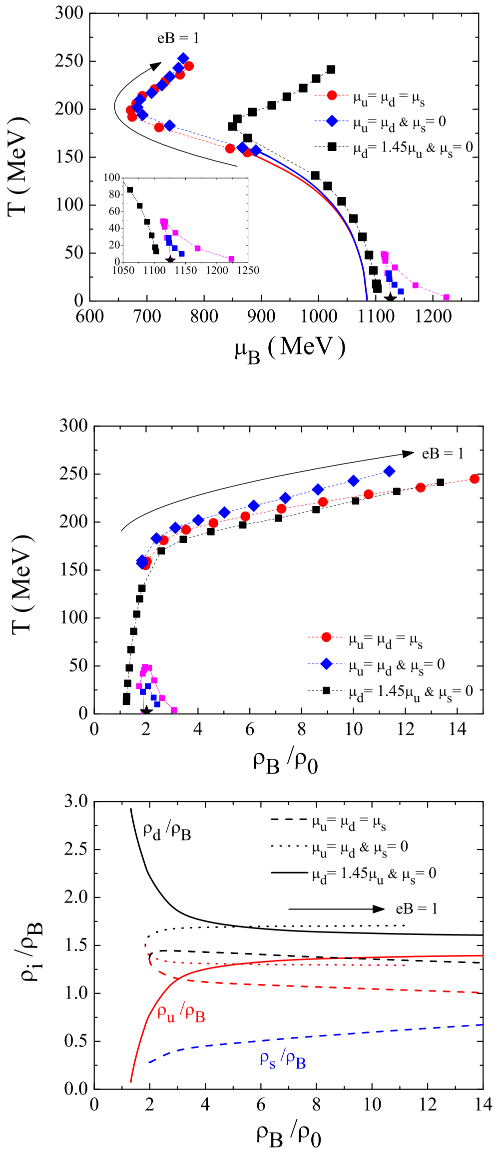

Figure 7.5: The T as a function of μ_B (top panel) and ρ_B (middle panel). The full lines are the first-order transitions at $B = 0$. Three scenarios are shown: $\mu_u = \mu_d = \mu_s$ (red dots), $\mu_u = \mu_d$; $\mu_s = 0$ (blue diamonds) and $\mu_d = 1.45\mu_u$, $\mu_s = 0$ (black squares) corresponding to the threshold isospin asymmetry above which no CEP occurs. In the last case for strong enough magnetic fields and low temperatures two or more CEPs exist at different temperatures for a given magnetic field intensity (pink and blue squares). The bottom panel shows the u, d and s quark fractions as a function of the baryonic density: $\mu_u = \mu_d = \mu_s$ (dashed line), $\mu_u = \mu_d$ and $\mu_s = 0$ (dotted line), and $\mu_d = 1.45\mu_u$; $\mu_s = 0$ (full line).

For the isospin symmetric quark matter scenario (blue diamonds), the magnetic field affects the CEP in a very similar way to the previous case, i.e. symmetric quark matter: the CEP's temperature is only slightly larger and its baryonic density is also slightly smaller.

As we have seen in Fig. 7.2, isospin asymmetrical matter with $\mu_d \simeq 1.45\mu_u$ (with $\mu_s = 0$) removes the CEP from the phase diagram, i.e. for $\mu_d \gtrsim 1.45\mu_u$, the chiral phase transition is a crossover at zero temperature. When one applies an external magnetic field, the CEP is recovered, thus, if $\mu_d \gtrsim 1.45\mu_u$, the magnetic field can drive again a first-order phase transition. When $\mu_d \simeq 1.45\mu_u$ two CEPs might appear for eB <0.1 GeV^2 . For sufficiently small values of B the T^{CEP} is small and the Landau level effects are visible.

The presence of an external magnetic field affects differently the u- and d-quarks in a complex pattern due to their different electric charges. A consequence is the possible appearance of two or more CEPs for a given magnetic field intensity. In our case two CEPs occur at different values of T and μ_B at the same magnetic field intensity for $0.03 \lesssim eB \lesssim 0.07$ GeV^2. Only one CEP remains above 0.07 GeV^2. For stronger fields we get $T^{\mathrm{CEP}} > 100$ MeV and the Landau level effects are completely washed out at these temperatures. In the lower panel of Fig. 7.5, we plot the u and d quark fractions corresponding to each CEP at different magnetic fields and for $\mu_d = 1.45\mu_u$ as a function of the baryonic density: it is seen that as the magnetic field becomes more intense the u-quark fraction comes closer to the d-quarks fraction. This is due to the larger charge of the u-quark and the fact that the quark density is proportional to the absolute value of the charge times the magnetic field intensity.

Finally, it is also important to point out that for low B values at zero temperature all three scenarios presented in top panel of Fig. 7.5 show that the μ_B^{crit}, where the chiral phase transition takes place, decreases with increasing B [123], indicating an easier transition to the partially chiral restored phase. However, at large B values this tendency disappears and μ_B^{crit} increases with B, in accordance with [78].

7.2 The IMC effect on CEP

Now, we want to analyze how the $G_s(eB)$ parametrization proposed in Section 6.2 affects the QCD phase diagram pattern. The $G_s(eB)$ [Eq. (6.4)] was parametrized to reproduce LQCD results at $\mu = 0$. The sign problem limits LQCD calculations to zero chemical potential, and, therefore, we do not know the impact that a finite baryonic chemical potential might have on the IMC mechanism.

In the following, we compare the following two scenarios for symmetric matter ($\mu_u = \mu_d = \mu_s$):

Case I: we take the usual $G_s = G_s^0$ and no IMC effects are included (discussed in Section 7.1.2);

Case II: we use $G_s(eB)$ [Eq. (6.4)] allowing IMC effects on the QCD phase diagram.

The effect of the IMC on the CEP's location (Case II) is presented in Fig. 7.6 (red points) in the $T - \mu_B$ plane (left panel) and in the $T - \rho_B/\rho_0$ plane (middle panel), for different intensities of the magnetic field, and in the $T - eB$ plane (right panel). For comparison we include in the same figure the CEP location without IMC effects, Case I (black curve).

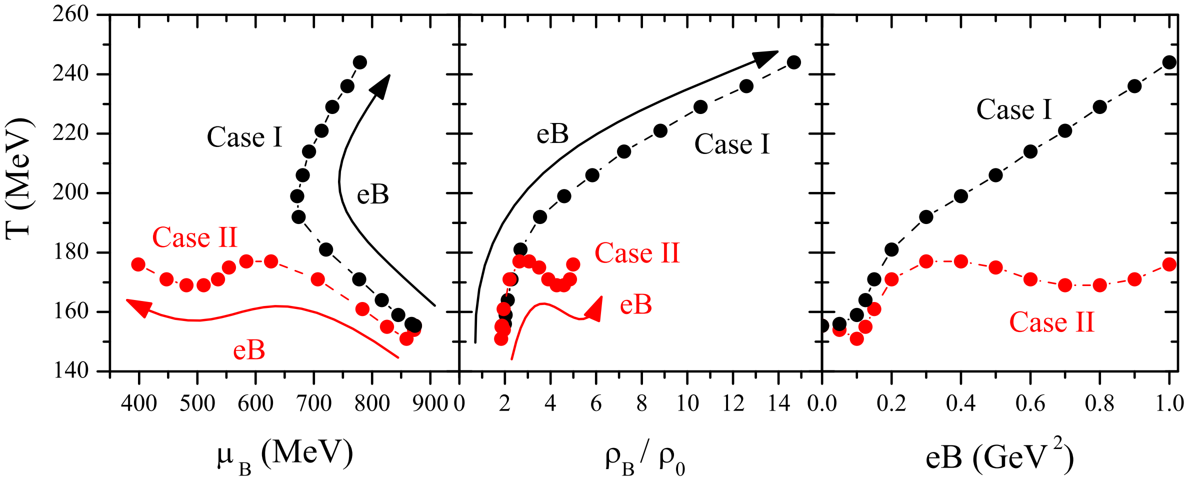

Figure 7.6: Location of the CEP in T^{CEP} versus μ_B^{CEP} (left panel) and T^{CEP} versus ρ_B^{CEP} (right panel) diagrams, for different intensities of the magnetic field without IMC effects $G_s = G_s^0$ (red curve) and with IMC effects $G_s = G_s(eB)$ (black curve).

We clearly observe a different behavior between these two scenarios: at $B = 0$ both CEPs coincide but, already for small values of B, the CEP occurs at lower temperatures in Case II, keeping, however, a similar behavior to Case I until $eB \sim 0.3$ GeV^2. The larger differences start for stronger magnetic fields: in Case II the position of the CEP oscillates between $T^{\text{CEP}} \approx 169$ and $T^{\text{CEP}} \approx 177$ MeV while the chemical potential takes increasingly smaller values; in Case I both values of T and μ_B for the CEP increase (see black curve, left panel of Fig. 7.6). In the middle panel of Fig. 7.6 the position of the CEP in the $T - \rho_B/\rho_0$ plane is presented. Comparing Cases

I and II, it is found that the IMC effect on the CEP results on its shift to smaller temperatures and densities especially for higher values of the magnetic field.

The reason of these behaviors lies in the fact that the weakening of the coupling $G_s(eB)$ will make the restoration of chiral symmetry easier. Increasing the magnetic field is not sufficient to counteract this effect as can be seen in Fig. 7.7 where we plot the quark masses (M_u-black line; M_d-red line; M_s-blue line) as function of μ_B for the respective $T^{\rm CEP}$ at $eB = 0.1$ and $eB = 0.5$ GeV^2.

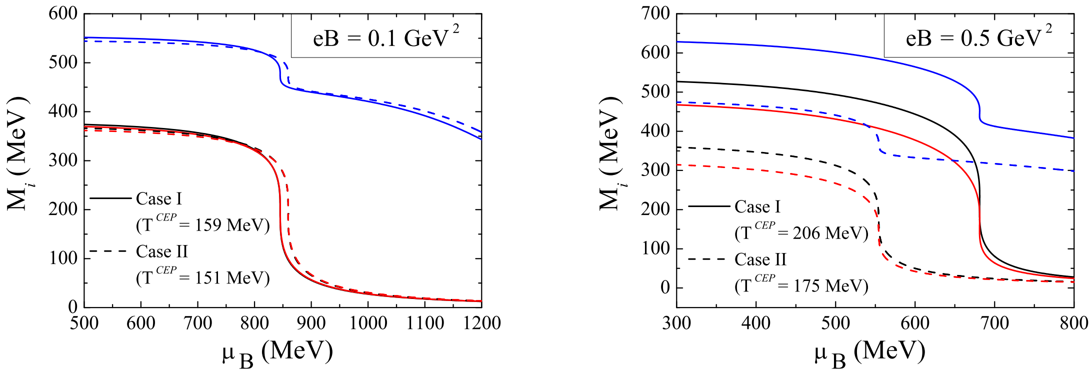

Figure 7.7: Masses of the quarks as function of μ_B at the respective $T^{\rm CEP}$ for two intensities of the magnetic field: $eB = 0.1$ GeV^2 (left panel) and : $eB = 0.5$ GeV^2 (right panel).

At $eB = 0.1$ GeV^2 (left panel) the G_s is barely affected by the magnetic field when IMC effects are included, and the values of the quark masses are very close to each other for both cases: in Case II the CEP occurs at smaller temperature and at near, slightly higher, chemical potential. When $eB = 0.5$ GeV^2 (right panel) the quark masses in Case I have increased with respect to the $B = 0$ case (due to the MC effect), being the restoration of chiral symmetry more difficult to achieve. However, when $G_s = G_s(eB)$, Case II, the masses of the quarks are smaller than their $B = 0$ value (due to IMC effect) leading to a faster restoration of chiral symmetry at small temperatures and chemical potentials.

Eventually, with the increase of B the CEP would move toward $\mu_B = 0$ and the deconfinement and chiral phase transitions would always be of first-order. There are indications that a first-order deconfinement phase transition should appear in the high magnetic field limit, and thus the existence of a Critical-End-Point in the $T - B$ diagram [148, 213].

7.3 Conclusions

In this Chapter we have studied the QCD phase diagram for several quark matter scenarios. Being the CEP a point in the QCD phase diagram which existence can define the pattern of chiral phase transition, i.e., the point where the chiral phase transition changes from a crossover to first-order, we gave special emphasis to its location.

We have started by showing that the PNJL model, when compared with the NJL model, predicts a CEP at higher temperatures and lower baryonic chemical potential for all quark matter scenarios. Then, using the PNJL model, the role played by the isospin asymmetry in the CEP's location was explored. As the isospin asymmetry increases, the CEP shifts to lower temperatures and higher baryon chemical potentials, disappearing from the phase diagram for $\mu_d/\mu_u > 1.45$.

Later, an external magnetic field was introduced in the PNJL model and the CEP's location for symmetric quark matter is calculated. We have obtained a very similar pattern as previously obtained for the NJL model [78]: as the magnetic field strength increases up to $eB \sim 0.4$ GeV^2, the CEP occurs at lower μ_B and higher T, and then for $eB > 0.4$ GeV^2 both the T and μ_B of the CEP became increasing functions of eB. Also as in previous NJL/PNJL studies [82, 84, 86], a cascade of first-order phase transitions was found, resulting in the existence of multiple CEPs at finite but lower temperatures.

Finally, in the last section, the impact of the IMC effect on the CEP's location was analyzed. Using the $G_s(eB)$ parametrization proposed in Section 6.2, which reproduces the IMC effect at zero chemical potential, the impact on the CEP's behavior was explored. It turns out that the weakening of the scalar coupling with eB drives the CEP to lower chemical potentials (and lower baryon densities) keeping its temperature in small variation range. For higher magnetic fields, the CEP moves to even lower chemical potentials and, eventually, disappears from the phase diagram, turning the crossover at $\mu_B = 0$ into a first-order chiral phase transition.

Chapter 8

Final Remarks

We have started this work by studying the effect of an external magnetic field on three-flavor quark matter, using both the PNJL and the EPNJL models. As in most effective models, the quark condensates undergo the Magnetic Catalysis (MC) effect at any temperature. As a result, the pseudocritical temperature of the chiral transition increases with the magnetic field strength. The Polyakov loop is also affected by the magnetic field presence: for a given temperature it increases with B; therefore, the pseudocritical temperature of the deconfinement transition also increases with B, even though it suffers a much weaker effect than the chiral pseudocritical transition temperature.

The chiral and the deconfinement pseudocritical transition temperatures behave differently with the magnetic field in both models: due to the entanglement interaction, which induces a strong correlation between the quarks and the Polyakov loop, the magnetic field has a stronger impact on the pseudocritical temperature of the deconfinement transition in the EPNJL model than in the PNJL model. Also the gap between the pseudocritical temperatures of the chiral and the deconfinement transitions is smaller in the EPNJL model. We have concluded that the possible coincidence of the chiral and the deconfinement pseudocritical transition temperatures, a feature of the entanglement interaction at zero magnetic field, depends on the chosen parametrization for the entanglement interaction at finite B. Furthermore, some parametrizations lead to the appearance of first-order phase transitions for the deconfinement and the chiral transitions at high B, while others maintain the crossover nature for any B strength (at least up to $eB = 1$ GeV^2).

Looking at the thermodynamics of both models, we have shown that both transitions are easier to identify in the thermodynamic observables of the PNJL model than in the EPNJL model, mainly due to the closeness of the pseudocritical transition temperatures in the EPNJL model. The influence of the light quark sector on the thermodynamical observables is predominant over the strange quark because the restoration of the chiral symmetry has already happened in the light quark sector. Concerning the strange quark, due to its much higher current mass value, the pseudocritical temperature of its chiral transition turned out to be almost insensitive to the presence of the magnetic field, when compared with the chiral pseudocritical temperatures of the light quarks. Furthermore, its large current mass also makes the strange quark less sensitive to the 't Hooft term, as opposed to the strong influence it has on the light quarks.

The results of both the EPNJL and the PNJL models were compared with the LQCD results [57, 58, 60]. Even though the models reproduce qualitatively well the MC effect seen in LQCD at zero temperature, they do not predict the Inverse Magnetic Catalysis (IMC) effect at temperatures near the transition temperature region. Since these models predict the MC effect at any temperature, the pseudocritical temperature of the chiral transitions increases with B, contrarily to LQCD results. Nevertheless, both models predict a crossover transition nature that persists up to 1 GeV^2, in agreement with LQCD.

We have then proposed two mechanisms that reproduce IMC. Using the EPNJL model we introduce through the Polyakov potential parameter T_0, which controls the onset temperature of deconfinement in pure gauge theory, a magnetic field dependence. The magnetic field dependence $T_0(eB)$ was motivated by the LQCD results [58] in which the magnetic field was seen to suppress small and favor large values of the Polyakov loop. Because the Polyakov potential is fixed in pure gauge theory, we have used its only free parameter T_0 to introduce in the model the backreaction of the magnetized quarks on the gauge fields. Using this mechanism the IMC effect was reproduced, but above a critical magnetic field strength a first-order phase transition was obtained, in disagreement with LQCD. Furthermore, the IMC effect was only obtained using the EPNJL model. The entanglement interaction, through the magnetic field dependent $T_0(eB)$, is responsible for a weakening of the four-quark scalar interaction coupling with B, which turned out to be the key ingredient for reproducing the IMC mechanism.

Later, based on the dependence of the QCD coupling α_s on the magnetic field [214], all the qualitative results of LQCD were reproduced by introducing a magnetic field dependence directly on the scalar interaction coupling of the NJL/PNJL models. The decreasing of $G_s(eB)$ with the magnetic field is essential, within effective quark models, to mimic the expected running of the coupling with the magnetic field strength. With this mechanism, both pseudocritical temperatures of the deconfinement and of the chiral transitions decrease with the magnetic field strength. The MC effect on the light quark condensates is obtained for low and high temperatures and the IMC effect appears near the transition temperature region. Concerning the strange quark we saw that, in spite of its large current mass, it also feels the IMC effect. In fact, the pseudocritical transition temperature of the strange quark is the one that decreases the most, contrarily to what happens with a constant coupling. We also investigated the influence of the IMC on several thermodynamical quantities, such as the sound velocity and the specific heat.

Finally, we have investigated the whole phase diagram in the presence of a magnetic field for several quark matter scenarios of isospin and strangeness. We gave special relevance to the location of the CEP. It was shown that isospin asymmetry shifts the CEP to larger baryon chemical potentials and smaller temperatures. At large asymmetries the CEP disappears. However, a strong enough magnetic field drives the system into a first-order phase transition again, leading to the appearance of the CEP. When the IMC effect is introduced at zero chemical potential in the model (as seen in LQCD), the location of the CEP is moved to lower baryon chemical potential values if the magnetic field strength increases, while the temperature almost does not change. This behavior contrasts with the results obtained with constant couplings, where it was shown that above a certain magnetic field both T^{CEP} and μ_B^{CEP} increase. Also the baryonic density at the CEP is affected: including the IMC effects, it increases only 1/3 of the expected if IMC effects were not considered, making the CEP much more accessible in the laboratory.

This work was fruitful in new and interesting results. With these results we hope to have contributed to clarify some relevant and timely physical topics that are attracting the attention of the physics community. On the other hand, there are issues that remain challenges to future researches. Among the possible perspectives of work, we highlight that an important bridge between theory and experiments can be provided by the study of the light scalar and pseudoscalar meson spectrum properties. The dependence of the meson masses on the temperature and magnetic field allows to study the effective restoration of chiral symmetry. Due to the crossover nature of the transition to the QGP, in the temperature region between $(1-2)T_c$, quark and gluon quasi-particles and pre-hadronic bound states can coexist [223, 224]. Therefore, the mesons can provide a good probe of the Quark-Gluon Plasma (QGP) properties and are important observables of HIC experiments. As future work, we would like to investigate how the meson properties at finite temperature are influenced by external magnetic fields. Concerning compact stars, it remains to be investigated how the formation and evolution of a protoneutron star would be affected by the presence of a strong magnetic field, in particular if quark degrees of freedom are present in an early stage of the star. In hadronic neutron stars magnetic fields above $\sim 10^{18}$ Gauss (~ 0.02 GeV^2) are not expected because the star would be gravitationally unstable, however, quark stars are self-bound and stronger magnetic fields could exist inside a stable star.

Appendix A

SU(N) group

Let us denote by τ_a the N^2-1 hermitian traceless matrices of the $SU(N)$ algebra. The $\frac{1}{2}\tau_a$ are the generators of the $SU(N)$ group, normalized as

$$\mathrm{tr}\tau_a\tau_b = 2\delta_{ab} \qquad (a,b)=1,2,...,N^2-1. \tag{A.1}$$

The τ_a are the Pauli matrices (see [176]) for $N=2$, and the Gell-Mann matrices for $N=3$,

$$\begin{aligned}
&\lambda_0=\sqrt{\tfrac{2}{3}}\begin{pmatrix}1&0&0\\0&1&0\\0&0&1\end{pmatrix}; \quad \lambda_1=\begin{pmatrix}0&1&0\\1&0&0\\0&0&0\end{pmatrix}; \quad \lambda_2=\begin{pmatrix}0&-i&0\\i&0&0\\0&0&0\end{pmatrix};\\
&\lambda_3=\begin{pmatrix}1&0&0\\0&-1&0\\0&0&0\end{pmatrix}; \quad \lambda_4=\begin{pmatrix}0&0&1\\0&0&0\\1&0&0\end{pmatrix}; \quad \lambda_5=\begin{pmatrix}0&0&-i\\0&0&0\\i&0&0\end{pmatrix}; \quad .\\
&\lambda_6=\begin{pmatrix}0&0&0\\0&0&1\\0&1&0\end{pmatrix}; \quad \lambda_7=\begin{pmatrix}0&0&0\\0&0&-i\\0&i&0\end{pmatrix}; \quad \lambda_8=\sqrt{\tfrac{1}{3}}\begin{pmatrix}1&0&0\\0&1&0\\0&0&-2\end{pmatrix}.
\end{aligned} \tag{A.2}$$

The matrices τ_a and $i\tau_a$ satisfy

$$\tau_a\tau_b=\frac{2}{N}\delta_{ab}+(d_{abc}+if_{abc})\tau_c, \tag{A.3}$$

and have the following commutation and anti-commutation relations

$$\begin{aligned}
&[\tau_a,\tau_b]=\tau_a\tau_b-\tau_b\tau_a=2if_{abc}\tau_c \qquad && \{\tau_a,\tau_b\}=\tau_a\tau_b+\tau_b\tau_a=\tfrac{4}{N}\delta_{ab}+2d_{abc}\tau_c\\
&\mathrm{tr}\,[\tau_a,\tau_b]\,\tau_c=4if_{abc} && \mathrm{tr}\{\tau_a,\tau_b\}\tau_c=4d_{abc},
\end{aligned} \tag{A.4}$$

where the f_{abc} and d_{abc} are the symmetric and antisymmetric group structure constants. For $N = 2$, $f_{abc} = \epsilon_{abc}$ and $d_{abc} = 0$. For $N = 3$, the nonvanishing terms are given in Table A.1.

Any $N \times N$ matrix can be written using τ_a matrices:

$$K = a_0 + a_a \tau_a \qquad a_0 = \frac{1}{N}\mathrm{tr}K \qquad a_a = \frac{1}{2}\mathrm{tr}\tau_a K \tag{A.5}$$

For $SU(2)$ and $SU(3)$ the $\det K$ is given by:

$$\begin{aligned} \det K &= a_0^2 - a_a^2 && (N = 2) \\ \det K &= a_0^3 - a_0 a_a^2 + \tfrac{2}{3} d_{abc} a_a a_b a_c && (N = 3) \end{aligned} \quad . \tag{A.6}$$

abc	f_{abc}	abc	f_{abc}	abc	f_{abc}
123	1	118	$1/\sqrt{3}$	355	$1/2$
147	$1/2$	146	$1/2$	366	$-1/2$
156	$-1/2$	157	$1/2$	377	$-1/2$
246	$1/2$	228	$1/\sqrt{3}$	448	$-1/(2\sqrt{3})$
257	$1/2$	247	$-1/2$	558	$-1/(2\sqrt{3})$
345	$1/2$	256	$1/2$	668	$-1/(2\sqrt{3})$
367	$-1/2$	338	$1/\sqrt{3}$	778	$-1/(2\sqrt{3})$
458	$\sqrt{3}/2$	344	$1/2$	888	$-1/\sqrt{3}$
678	$\sqrt{3}/2$				

Table A.1: $SU(3)$ group structure constants.

Appendix B

Bosonization

One can write the partition function of a boson field as

$$\int \mathcal{D}\phi \exp\left[-\frac{1}{2}\int_0^\beta d\tau \int d^3x \phi D(\tau,\mathbf{x})\phi\right] = (\det D(\tau,\mathbf{x}))^{1/2},$$

using the formula

$$\int_{-\infty}^{+\infty} dx_1 ... dx_2 \exp\left[-\frac{1}{2}\int_0^\beta d\tau \int d^3x \phi D(\tau,\mathbf{x})\phi\right] = (\det D(\tau,\mathbf{x}))^{1/2}.$$

Doing a scalar shift on the bosonic field

$$q_i \to \phi_i \pm 2G(\bar{q}\mathcal{O}_i q),$$

where $\bar{q}\mathcal{O}_i q$ is a scalar Dirac bilinear, and G is a constant. Using $D = \mathbf{1}/2G$, we have

$$\exp\left[-\int_0^\beta d\tau \int d^3x G(\bar{q}\mathcal{O}_i q)^2\right] \int \mathcal{D}\phi_i \exp\left[\int_0^\beta d\tau \int d^3x \left(-\frac{\phi_i^2}{4G} \mp \phi_i(\bar{q}\mathcal{O}_i q)\right)\right] = \det\left(\frac{\mathbf{1}}{2G}\right)^{1/2},$$

and thus we can write

$$\exp\left[\int_0^\beta d\tau \int d^3x G(\bar{q}\mathcal{O}_i q)^2\right] = \mathcal{N}' \int \mathcal{D}\phi_i \exp\left[\int_0^\beta d\tau \int d^3x \left(-\frac{\phi_i^2}{4G} \pm \phi_i \bar{q}\mathcal{O}_i q\right)\right].$$

The $\mathcal{N}'$ is a thermodynamical irrelevant factor. The four-fermion interaction is transformed into a two-fermion interaction coupled to a boson field via Yukawa coupling. Notice there is no approximation in the above transformation. Applying the Hubbard-Stratonovich transformation to the $\mathcal{L}_4$ term of the $\mathcal{L}_{\mathrm{NJL}}$ [Eq. (3.1)], we obtain

$$\begin{aligned}
&\exp\left\{\int_0^\beta d\tau \int d^3x \frac{G_s^0}{2}\sum_{a=0}^{8}\left[(\bar{q}\lambda^a q)^2 + (\bar{q}i\gamma_5\lambda^a q)^2\right]\right\} \\
&= \int \mathcal{D}\phi_1^a \mathcal{D}\phi_2^b \exp\left[\int_0^\beta d\tau \int d^3x \left(-\frac{1}{2G_s^0}\left((\phi_i^a)^2 + (\phi_i^b)^2\right) + \phi_i^a(\bar{q}\gamma_a q) + \phi_j^b(\bar{q}i\gamma_5\gamma_a q)\right)\right],
\end{aligned}$$

where we have defined $\mathcal{O}_i = 1$, and $\mathcal{O}_j = i\gamma_5$. The bosonization consists in the analytical integration of the quadratic fermion terms from the Euclidean action, obtaining an effective Euclidean action that only depends on the introduced bosonic degrees of freedom. Applying this procedure to the $\mathcal{L}_0 + \mathcal{L}_4$ term of the $\mathcal{L}_{\text{NJL}}$ [Eq. (3.1)], noting that

$$\frac{G_s^0}{2}\sum_a(\bar{q}\lambda^a q) = G_s^0 \sum_{i=u,d,s} (\bar{q}_i q_i)^2\,,$$

and $\langle \bar{q} i\gamma_5 q\rangle$ vanishes in a homogeneous ground state, we will end up with only three non-vanishing bosonic fields: ϕ_1^u, ϕ_1^d, and ϕ_1^s. Now, to move forward, we need to introduce the MFA approximation: replace the auxiliary bosonic fields by their classical fields

$$\left.\frac{\delta S_E}{\delta \phi_i^a}\right|_{\phi_1^a=\bar{\phi}_1^a} = 0,$$

and neglect fluctuations around their classical fields thermal expectation values. Calculating the thermal expectation value of the classical bosonic fields we get for $\langle\phi_1^u\rangle$, $\langle\phi_1^d\rangle$, and $\langle\phi_1^s\rangle$, the quark condensates $\langle\bar{q}_u q_u\rangle$, $\langle\bar{q}_d q_d\rangle$, and $\langle\bar{q}_s q_s\rangle$, respectively, given by Eq. (3.35) that satisfy the gap equations [Eqs (3.12)], without the 't Hooft term.

To bosonize the $SU(3)$ NJL model of Eq. (3.1) we need to rewrite the Lagrangian in a more appropriate form, converting the six-quark interaction $\mathcal{L}_6$ into a four-quark interaction term. The details can be found in [216].

List of Figures

List of Tables

Bibliography

[1] D. J. Gross and F. Wilczek, *Ultraviolet Behavior of Nonabelian Gauge Theories*, Phys.Rev.Lett. **30** (1973) 1343–1346.

[2] Z. Fodor, *Selected results in lattice quantum chromodynamics*, PTEP **2012** (2012) 01A108.

[3] S. Sharma, *QCD Thermodynamics on the Lattice*, Adv.High Energy Phys. **2013** (2013) 452978, `arXiv:1403.2102 [hep-lat]`.

[4] C. D. Roberts, *Strong QCD and Dyson-Schwinger Equations*, `arXiv:1203.5341 [nucl-th]`.

[5] O. Biebel, *Experimental tests of the strong interaction and its energy dependence in electron positron annihilation*, Phys. Rept. **340** (2001) 165–289.

[6] S. Kluth, *Tests of Quantum Chromo Dynamics at e+ e- Colliders*, Rept. Prog. Phys. **69** (2006) 1771–1846, `arXiv:hep-ex/0603011 [hep-ex]`.

[7] H. Satz, *Extreme states of matter in strong interaction physics. An introduction*, Lect.Notes Phys. **841** (2012) 1.

[8] K. Rajagopal and F. Wilczek, *The Condensed matter physics of QCD*, `arXiv:hep-ph/0011333 [hep-ph]`.

[9] M. G. Alford, A. Schmitt, K. Rajagopal, and T. Schäfer, *Color superconductivity in dense quark matter*, Rev.Mod.Phys. **80** (2008) 1455–1515, `arXiv:0709.4635 [hep-ph]`.

[10] *The Frontiers of Nuclear Science, A Long Range Plan*, `arXiv:0809.3137 [nucl-ex]`.

[11] K. Fukushima and T. Hatsuda, *The phase diagram of dense QCD*, Rept.Prog.Phys. **74** (2011) 014001, `arXiv:1005.4814 [hep-ph]`.

[12] NA49 Collaboration, S. V. Afanasiev et al., *Energy dependence of pion and kaon production in central Pb + Pb collisions*, Phys. Rev. **C66** (2002) 054902, `arXiv:nucl-ex/0205002 [nucl-ex]`.

[13] H. Song, S. A. Bass, U. Heinz, T. Hirano, and C. Shen, *200 A GeV Au+Au collisions serve a nearly perfect quark-gluon liquid*, Phys.Rev.Lett. **106** (2011) 192301, `arXiv:1011.2783 [nucl-th]`.

[14] U. Heinz, P. Sorensen, A. Deshpande, C. Gagliardi, F. Karsch, et al., *Exploring the properties of the phases of QCD matter - research opportunities and priorities for the next decade*, `arXiv:1501.06477 [nucl-th]`.

[15] NICA Collaboration, A. Sissakian and A. Sorin, *The nuclotron-based ion collider facility (NICA) at JINR: New prospects for heavy ion collisions and spin physics*, J.Phys. **G36** (2009) 064069.

[16] NICA, MPD Collaboration, V. Kekelidze, A. Kovalenko, I. Meshkov, A. Sorin, and G. Trubnikov, *NICA at JINR: New prospects for exploration of quark-gluon matter*, Phys.Atom.Nucl. **75** (2012) 542–545.

[17] STAR Collaboration, B. Abelev et al., *Identified particle production, azimuthal anisotropy, and interferometry measurements in Au+Au collisions at s(NN)**(1/2) = 9.2- GeV*, Phys.Rev. **C81** (2010) 024911, `arXiv:0909.4131 [nucl-ex]`.

[18] STAR Collaboration, L. Adamczyk et al., *Beam energy dependence of moments of the net-charge multiplicity distributions in Au+Au collisions at RHIC*, Phys.Rev.Lett. **113** (2014) 092301, `arXiv:1402.1558 [nucl-ex]`.

[19] STAR Collaboration, L. Adamczyk et al., *Energy Dependence of Moments of Net-proton Multiplicity Distributions at RHIC*, Phys.Rev.Lett. **112** no. 3, (2014) 032302, `arXiv:1309.5681 [nucl-ex]`.

[20] NA49, NA61/SHINE Collaboration, M. Gazdzicki, *NA49/NA61: results and plans on beam energy and system size scan at the CERN SPS*, J.Phys. **G38** (2011) 124024, `arXiv:1107.2345 [nucl-ex]`.

[21] Y. Akiba, A. Angerami, H. Caines, A. Frawley, U. Heinz, et al., *The Hot QCD White Paper: Exploring the Phases of QCD at RHIC and the LHC*, `arXiv:1502.02730 [nucl-ex]`.

[22] S. Borsanyi, G. Endrodi, Z. Fodor, A. Jakovac, S. D. Katz, et al., *The QCD equation of state with dynamical quarks*, JHEP **1011** (2010) 077, `arXiv:1007.2580 [hep-lat]`.

[23] S. Borsanyi, Z. Fodor, C. Hoelbling, S. D. Katz, S. Krieg, et al., *Full result for the QCD equation of state with 2+1 flavors*, Phys.Lett. **B730** (2014) 99–104, `arXiv:1309.5258 [hep-lat]`.

[24] HotQCD Collaboration, A. Bazavov et al., *Equation of state in (2+1)-flavor QCD*, Phys.Rev. **D90** no. 9, (2014) 094503, `arXiv:1407.6387 [hep-lat]`.

[25] Y. Aoki, S. Borsanyi, S. Durr, Z. Fodor, S. D. Katz, et al., *The QCD transition temperature: results with physical masses in the continuum limit II.*, JHEP **0906** (2009) 088, `arXiv:0903.4155 [hep-lat]`.

[26] Wuppertal-Budapest Collaboration, S. Borsanyi et al., *Is there still any T_c mystery in lattice QCD? Results with physical masses in the continuum limit III*, JHEP **1009** (2010) 073, `arXiv:1005.3508 [hep-lat]`.

[27] S. Borsanyi, *Thermodynamics of the QCD transition from lattice*, Nucl.Phys. **A904-905** (2013) 270c–277c, `arXiv:1210.6901 [hep-lat]`.

[28] K. Fukushima and C. Sasaki, *The phase diagram of nuclear and quark matter at high baryon density*, Prog.Part.Nucl.Phys. **72** (2013) 99–154, `arXiv:1301.6377 [hep-ph]`.

[29] H. Ueda, T. Z. Nakano, A. Ohnishi, M. Ruggieri, and K. Sumiyoshi, *QCD phase diagram at finite baryon and isospin chemical potentials in Polyakov loop extended quark meson model with vector interaction*, Phys.Rev. **D88** no. 7, (2013) 074006, `arXiv:1304.4331 [nucl-th]`.

[30] F. Wilczek, *Application of the renormalization group to a second order QCD phase transition*, Int.J.Mod.Phys. **A7** (1992) 3911–3925.

[31] K. Rajagopal and F. Wilczek, *Static and dynamic critical phenomena at a second order QCD phase transition*, Nucl.Phys. **B399** (1993) 395–425, `arXiv:hep-ph/9210253 [hep-ph]`.

[32] M. A. Stephanov, K. Rajagopal, and E. V. Shuryak, *Signatures of the tricritical point in QCD*, Phys.Rev.Lett. **81** (1998) 4816–4819, `arXiv:hep-ph/9806219 [hep-ph]`.

[33] N. Glendenning, *Compact stars: Nuclear physics, particle physics, and general relativity*,.

[34] P. Demorest, T. Pennucci, S. Ransom, M. Roberts, and J. Hessels, *Shapiro Delay Measurement of A Two Solar Mass Neutron Star*, Nature **467** (2010) 1081–1083, `arXiv:1010.5788 [astro-ph.HE]`.

[35] J. Antoniadis, P. C. Freire, N. Wex, T. M. Tauris, R. S. Lynch, et al., *A Massive Pulsar in a Compact Relativistic Binary*, Science **340** (2013) 6131, `arXiv:1304.6875 [astro-ph.HE]`.

[36] M. Baldo, G. Burgio, and H. Schulze, *Hyperon stars in the Brueckner-Bethe-Goldstone theory*, Phys.Rev. **C61** (2000) 055801, `arXiv:nucl-th/9912066 [nucl-th]`.

[37] I. Vidana, A. Polls, A. Ramos, L. Engvik, and M. Hjorth-Jensen, *Hyperon-hyperon interactions and properties of neutron star matter*, Phys.Rev. **C62** (2000) 035801, `arXiv:nucl-th/0004031 [nucl-th]`.

[38] H.-J. Schulze, A. Polls, A. Ramos, and I. Vidana, *Maximum mass of neutron stars*, Phys.Rev. **C73** (2006) 058801.

[39] I. Vidana, D. Logoteta, C. Providencia, A. Polls, and I. Bombaci, *Estimation of the effect of hyperonic three-body forces on the maximum mass of neutron stars*, Europhys.Lett. **94** (2011) 11002, `arXiv:1006.5660 [nucl-th]`.

[40] R. Cavagnoli, D. P. Menezes, and C. Providencia, *Neutron star properties and the symmetry energy*, Phys.Rev. **C84** (2011) 065810, `arXiv:1108.1733 [hep-ph]`.

[41] I. Bednarek, P. Haensel, J. Zdunik, M. Bejger, and R. Manka, *Hyperons in neutron-star cores and two-solar-mass pulsar*, Astron.Astrophys. **543** (2012) A157, `arXiv:1111.6942 [astro-ph.SR]`.

[42] P. K. Panda, D. P. Menezes, and C. Providência, *Effects of the symmetry energy on the kaon condensates in the quark-meson coupling model*, Phys.Rev. **C89** no. 4, (2014) 045803.

[43] L. Bonanno and A. Sedrakian, *Composition and stability of hybrid stars with hyperons and quark color-superconductivity*, Astron.Astrophys. **539** (2012) A16, `arXiv:1108.0559 [astro-ph.SR]`.

[44] ALICE Collaboration, D. Elia, *Strangeness production in ALICE*, J.Phys.Conf.Ser. **455** (2013) 012005.

[45] J. Rafelski and B. Muller, *Strangeness Production in the Quark - Gluon Plasma*, Phys.Rev.Lett. **48** (1982) 1066.

[46] P. Koch, B. Muller, and J. Rafelski, *Strangeness in Relativistic Heavy Ion Collisions*, Phys.Rept. **142** (1986) 167–262.

[47] S. Chatterjee, R. Godbole, and S. Gupta, *Strange freezeout*, Phys.Lett. **B727** (2013) 554–557, `arXiv:1306.2006 [nucl-th]`.

[48] K. Bugaev, D. Oliinychenko, J. Cleymans, A. Ivanytskyi, I. Mishustin, et al., *Chemical Freeze-out of Strange Particles and Possible Root of Strangeness Suppression*, Europhys.Lett. **104** (2013) 22002, `arXiv:1308.3594 [hep-ph]`.

[49] A. Bazavov, H. T. Ding, P. Hegde, O. Kaczmarek, F. Karsch, et al., *Additional Strange Hadrons from QCD Thermodynamics and Strangeness Freezeout in Heavy Ion Collisions*, Phys.Rev.Lett. **113** no. 7, (2014) 072001, `arXiv:1404.6511 [hep-lat]`.

[50] R. Bellwied, S. Borsanyi, Z. Fodor, S. D. Katz, and C. Ratti, *Is there a flavor hierarchy in the deconfinement transition of QCD?*, Phys.Rev.Lett. **111** (2013) 202302, `arXiv:1305.6297 [hep-lat]`.

[51] R. C. Duncan and C. Thompson, *Formation of very strongly magnetized neutron stars - implications for gamma-ray bursts*, Astrophys.J. **392** (1992) L9.

[52] K. Fukushima, D. E. Kharzeev, and H. J. Warringa, *The Chiral Magnetic Effect*, Phys.Rev. **D78** (2008) 074033, `arXiv:0808.3382 [hep-ph]`.

[53] D. E. Kharzeev and H. J. Warringa, *Chiral Magnetic conductivity*, Phys.Rev. **D80** (2009) 034028, `arXiv:0907.5007 [hep-ph]`.

[54] V. Skokov, A. Y. Illarionov, and V. Toneev, *Estimate of the magnetic field strength in heavy-ion collisions*, Int.J.Mod.Phys. **A24** (2009) 5925–5932, `arXiv:0907.1396 [nucl-th]`.

[55] T. Vachaspati, *Magnetic fields from cosmological phase transitions*, Phys.Lett. **B265** (1991) 258–261.

[56] K. Enqvist and P. Olesen, *On primordial magnetic fields of electroweak origin*, Phys.Lett. **B319** (1993) 178–185, `arXiv:hep-ph/9308270 [hep-ph]`.

[57] G. Bali, F. Bruckmann, G. Endrodi, Z. Fodor, S. Katz, et al., *The QCD phase diagram for external magnetic fields*, JHEP **1202** (2012) 044, `arXiv:1111.4956 [hep-lat]`.

[58] F. Bruckmann, G. Endrodi, and T. G. Kovacs, *Inverse magnetic catalysis and the Polyakov loop*, JHEP **1304** (2013) 112, `arXiv:1303.3972 [hep-lat]`.

[59] G. Bali, F. Bruckmann, G. Endrödi, S. Katz, and A. Schäfer, *The QCD equation of state in background magnetic fields*, JHEP **1408** (2014) 177, `arXiv:1406.0269 [hep-lat]`.

[60] G. Bali, F. Bruckmann, G. Endrodi, Z. Fodor, S. Katz, et al., *QCD quark condensate in external magnetic fields*, Phys.Rev. **D86** (2012) 071502, `arXiv:1206.4205 [hep-lat]`.

[61] E. M. Ilgenfritz, M. Muller-Preussker, B. Petersson, and A. Schreiber, *Magnetic catalysis (and inverse catalysis) at finite temperature in two-color lattice QCD*, Phys.Rev. **D89** no. 5, (2014) 054512, `arXiv:1310.7876 [hep-lat]`.

[62] M. D'Elia, S. Mukherjee, and F. Sanfilippo, *QCD Phase Transition in a Strong Magnetic Background*, Phys.Rev. **D82** (2010) 051501, `arXiv:1005.5365 [hep-lat]`.

[63] V. Bornyakov, P. Buividovich, N. Cundy, O. Kochetkov, and A. Schäfer, *Deconfinement transition in two-flavor lattice QCD with dynamical overlap fermions in an external magnetic field*, Phys.Rev. **D90** no. 3, (2014) 034501, `arXiv:1312.5628 [hep-lat]`.

[64] J. O. Andersen, W. R. Naylor, and A. Tranberg, *Chiral and deconfinement transitions in a magnetic background using the functional renormalization group with the Polyakov loop*, JHEP **1404** (2014) 187, `arXiv:1311.2093 [hep-ph]`.

[65] H. Liu, L. Yu, and M. Huang, *Charged and neutral vector ρ mesons in a magnetic field*, Phys.Rev. **D91** no. 1, (2015) 014017, `arXiv:1408.1318 [hep-ph]`.

[66] S. Fayazbakhsh and N. Sadooghi, *Anomalous magnetic moment of hot quarks, inverse magnetic catalysis, and reentrance of the chiral symmetry broken phase*, Phys.Rev. **D90** no. 10, (2014) 105030, `arXiv:1408.5457 [hep-ph]`.

[67] A. A. Andrianov, D. Espriu, and X. Planells, *Chemical potentials and parity breaking: the Nambu-Jona-Lasinio model*, Eur.Phys.J. **C74** no. 2, (2014) 2776, `arXiv:1310.4416 [hep-ph]`.

[68] D. Ebert and K. Klimenko, *Quark droplets stability induced by external magnetic field*, Nucl.Phys. **A728** (2003) 203–225, `arXiv:hep-ph/0305149 [hep-ph]`.

[69] S. Ghosh, S. Mandal, and S. Chakrabarty, *Chiral properties of QCD vacuum in magnetars- A Nambu-Jona-Lasinio model with semi-classical approximation*, Phys.Rev. **C75** (2007) 015805, `arXiv:astro-ph/0507127 [astro-ph]`.

[70] D. Menezes, M. Benghi Pinto, S. Avancini, A. Perez Martinez, and C. Providencia, *Quark matter under strong magnetic fields in the Nambu-Jona-Lasinio Model*, Phys.Rev. **C79** (2009) 035807, `arXiv:0811.3361 [nucl-th]`.

[71] D. Menezes, M. Benghi Pinto, S. Avancini, and C. Providencia, *Quark matter under strong magnetic fields in the su(3) Nambu-Jona-Lasinio Model*, Phys.Rev. **C80** (2009) 065805, `arXiv:0907.2607 [nucl-th]`.

[72] S. Avancini, D. Menezes, and C. Providencia, *Finite temperature quark matter under strong magnetic fields*, Phys.Rev. **C83** (2011) 065805.

[73] A. F. Garcia and M. B. Pinto, *Surface tension of magnetized quark matter*, Phys.Rev. **C88** no. 2, (2013) 025207, `arXiv:1306.3090 [hep-ph]`.

[74] R. Farias, K. Gomes, G. Krein, and M. Pinto, *Importance of asymptotic freedom for the pseudocritical temperature in magnetized quark matter*, Phys.Rev. **C90** no. 2, (2014) 025203, `arXiv:1404.3931 [hep-ph]`.

[75] D. Ebert, K. Klimenko, M. Vdovichenko, and A. Vshivtsev, *Magnetic oscillations in dense cold quark matter with four fermion interactions*, Phys.Rev. **D61** (2000) 025005, `arXiv:hep-ph/9905253 [hep-ph]`.

[76] J. K. Boomsma and D. Boer, *The Influence of strong magnetic fields and instantons on the phase structure of the two-flavor NJL model*, Phys.Rev. **D81** (2010) 074005, `arXiv:0911.2164 [hep-ph]`.

[77] B. Chatterjee, H. Mishra, and A. Mishra, *Vacuum structure and chiral symmetry breaking in strong magnetic fields for hot and dense quark matter*, Phys.Rev. **D84** (2011) 014016, `arXiv:1101.0498 [hep-ph]`.

[78] S. S. Avancini, D. P. Menezes, M. B. Pinto, and C. Providencia, *The QCD Critical End Point Under Strong Magnetic Fields*, Phys.Rev. **D85** (2012) 091901, `arXiv:1202.5641 [hep-ph]`.

[79] S. Fayazbakhsh, S. Sadeghian, and N. Sadooghi, *Properties of neutral mesons in a hot and magnetized quark matter*, Phys.Rev. **D86** (2012) 085042, `arXiv:1206.6051 [hep-ph]`.

[80] G. N. Ferrari, A. F. Garcia, and M. B. Pinto, *Chiral Transition Within Effective Quark Models Under Magnetic Fields*, Phys.Rev. **D86** (2012) 096005, `arXiv:1207.3714 [hep-ph]`.

[81] J. Chao, P. Chu, and M. Huang, *Inverse magnetic catalysis induced by sphalerons*, Phys.Rev. **D88** (2013) 054009, `arXiv:1305.1100 [hep-ph]`.

[82] R. Z. Denke and M. B. Pinto, *Influence of a repulsive vector coupling in magnetized quark matter*, Phys.Rev. **D88** no. 5, (2013) 056008, `arXiv:1306.6246 [hep-ph]`.

[83] S. Fayazbakhsh and N. Sadooghi, *Weak decay constant of neutral pions in a hot and magnetized quark matter*, Phys.Rev. **D88** no. 6, (2013) 065030, `arXiv:1306.2098 [hep-ph]`.

[84] P. G. Allen and N. N. Scoccola, *Quark matter under strong magnetic fields in SU(2) NJL-type models: parameter dependence of the cold dense matter phase diagram*, Phys.Rev. **D88** (2013) 094005, `arXiv:1309.2258 [hep-ph]`.

[85] E. J. Ferrer, V. de la Incera, I. Portillo, and M. Quiroz, *New look at the QCD ground state in a magnetic field*, Phys.Rev. **D89** no. 8, (2014) 085034, `arXiv:1311.3400 [nucl-th]`.

[86] A. Grunfeld, D. Menezes, M. Pinto, and N. Scoccola, *Phase structure of cold magnetized quark matter within the SU(3) NJL model*, Phys.Rev. **D90** no. 4, (2014) 044024, `arXiv:1402.4731 [hep-ph]`.

[87] G. Cao, L. He, and P. Zhuang, *Collective modes and Kosterlitz-Thouless transition in a magnetic field in the planar Nambu-Jona-Lasino model*, Phys.Rev. **D90** no. 5, (2014) 056005, `arXiv:1408.5364 [hep-ph]`.

[88] L. Yu, H. Liu, and M. Huang, *Spontaneous generation of local CP violation and inverse magnetic catalysis*, Phys.Rev. **D90** no. 7, (2014) 074009, `arXiv:1404.6969 [hep-ph]`.

[89] P.-C. Chu, X. Wang, L.-W. Chen, and M. Huang, *Quark magnetar in the three-flavor Nambu–Jona-Lasinio model with vector interactions and a magnetized gluon potential*, Phys.Rev. **D91** no. 2, (2015) 023003, `arXiv:1409.6154 [nucl-th]`.

[90] B. Chatterjee, H. Mishra, and A. Mishra, *CP violation and chiral symmetry breaking in hot and dense quark matter in the presence of a magnetic field*, Phys.Rev. **D91** no. 3, (2015) 034031, `arXiv:1409.3454 [hep-ph]`.

[91] S. Shi, Y.-C. Yang, Y.-H. Xia, Z.-F. Cui, X.-J. Liu, et al., *Dynamical chiral symmetry breaking in the NJL model with a constant external magnetic field*, Phys.Rev. **D91** no. 3, (2015) 036006, `arXiv:1503.00452 [hep-ph]`.

[92] M. Chernodub, *Spontaneous electromagnetic superconductivity of vacuum in strong magnetic field: evidence from the Nambu–Jona-Lasinio model*, Phys.Rev.Lett. **106** (2011) 142003, `arXiv:1101.0117 [hep-ph]`.

[93] E. Gorbar, V. Miransky, and I. Shovkovy, *Surprises in relativistic matter in a magnetic field*, Prog.Part.Nucl.Phys. **67** (2012) 547–551, `arXiv:1111.3401 [hep-ph]`.

[94] D. P. Menezes, M. B. Pinto, L. B. Castro, P. Costa, and C. Providência, *Repulsive Vector Interaction in Three Flavor Magnetized Quark and Stellar Matter*, Phys.Rev. **C89** no. 5, (2014) 055207, `arXiv:1403.2502 [nucl-th]`.

[95] W.-j. Fu, Y.-x. Liu, and Y.-l. Wu, *Chiral Magnetic Effect and QCD Phase Transitions with Effective Models*, Int.J.Mod.Phys. **A26** (2011) 4335–4365, `arXiv:1003.4169 [hep-ph]`.

[96] K. Fukushima, M. Ruggieri, and R. Gatto, *Chiral magnetic effect in the PNJL model*, Phys.Rev. **D81** (2010) 114031, `arXiv:1003.0047 [hep-ph]`.

[97] R. Gatto and M. Ruggieri, *Dressed Polyakov loop and phase diagram of hot quark matter under magnetic field*, Phys.Rev. **D82** (2010) 054027, `arXiv:1007.0790 [hep-ph]`.

[98] R. Gatto and M. Ruggieri, *Deconfinement and Chiral Symmetry Restoration in a Strong Magnetic Background*, Phys.Rev. **D83** (2011) 034016, `arXiv:1012.1291 [hep-ph]`.

[99] K. Kashiwa, *Entanglement between chiral and deconfinement transitions under strong uniform magnetic background field*, Phys.Rev. **D83** (2011) 117901, `arXiv:1104.5167 [hep-ph]`.

[100] R. Gatto and M. Ruggieri, *Hot Quark Matter with an Axial Chemical Potential*, Phys.Rev. **D85** (2012) 054013, `arXiv:1110.4904 [hep-ph]`.

[101] W.-j. Fu, *Fluctuations and correlations of hot QCD matter in an external magnetic field*, Phys.Rev. **D88** no. 1, (2013) 014009, `arXiv:1306.5804 [hep-ph]`.

[102] J. O. Andersen and A. A. Cruz, *Two-color QCD in a strong magnetic field: The role of the Polyakov loop*, Phys.Rev. **D88** no. 2, (2013) 025016, `arXiv:1211.7293 [hep-ph]`.

[103] M. Ferreira, P. Costa, and C. Providência, *Strange quark chiral phase transition in hot 2+1-flavor magnetized quark matter*, Phys.Rev. **D90** no. 1, (2014) 016012, `arXiv:1406.3608 [hep-ph]`.

[104] M. Ferreira, P. Costa, O. Lourenço, T. Frederico, and C. Providência, *Inverse magnetic catalysis in the (2+1)-flavor Nambu-Jona-Lasinio and Polyakov-Nambu-Jona-Lasinio models*, Phys.Rev. **D89** no. 11, (2014) 116011, `arXiv:1404.5577 [hep-ph]`.

[105] M. Ferreira, P. Costa, and C. Providência, *Deconfinement, chiral symmetry restoration and thermodynamics of (2+1)-flavor hot QCD matter in an external magnetic field*, Phys.Rev. **D89** no. 3, (2014) 036006, `arXiv:1312.6733 [hep-ph]`.

[106] P. Costa, M. Ferreira, H. Hansen, D. P. Menezes, and C. Providência, *Phase transition and critical end point driven by an external magnetic field in asymmetric quark matter*, Phys.Rev. **D89** no. 5, (2014) 056013, `arXiv:1307.7894 [hep-ph]`.

[107] M. Ferreira, P. Costa, D. P. Menezes, C. Providência, and N. Scoccola, *Deconfinement and chiral restoration within the SU(3) Polyakov–Nambu–Jona-Lasinio and entangled Polyakov–Nambu–Jona-Lasinio models in an external magnetic field*, Phys.Rev. **D89** no. 1, (2014) 016002, `arXiv:1305.4751 [hep-ph]`.

[108] G. Endrödi, *QCD equation of state at nonzero magnetic fields in the Hadron Resonance Gas model*, JHEP **1304** (2013) 023, `arXiv:1301.1307 [hep-ph]`.

[109] A. J. Mizher, M. Chernodub, and E. S. Fraga, *Phase diagram of hot QCD in an external magnetic field: possible splitting of deconfinement and chiral transitions*, Phys.Rev. **D82** (2010) 105016, `arXiv:1004.2712 [hep-ph]`.

[110] A. N. Tawfik and N. Magdy, *SU(3) Polyakov linear-σ model in an external magnetic field*, Phys.Rev. **C90** no. 1, (2014) 015204, `arXiv:1406.7488 [hep-ph]`.

[111] S. Chakrabarty, *Quark matter in strong magnetic field*, Phys.Rev. **D54** (1996) 1306–1316, `arXiv:hep-ph/9603406 [hep-ph]`.

[112] E. S. Fraga and L. F. Palhares, *Deconfinement in the presence of a strong magnetic background: an exercise within the MIT bag model*, Phys.Rev. **D86** (2012) 016008, `arXiv:1201.5881 [hep-ph]`.

[113] A. Isayev, *Stability of magnetized strange quark matter in the MIT bag model with a density dependent bag pressure*, Phys.Rev. **C91** no. 1, (2015) 015208, `arXiv:1501.07772 [hep-ph]`.

[114] J. O. Andersen, W. R. Naylor, and A. Tranberg, *Inverse magnetic catalysis and regularization in the quark-meson model*, JHEP **1502** (2015) 042, `arXiv:1410.5247 [hep-ph]`.

[115] V. Skokov, *Phase diagram in an external magnetic field beyond a mean-field approximation*, Phys.Rev. **D85** (2012) 034026, `arXiv:1112.5137 [hep-ph]`.

[116] E. Fraga, B. Mintz, and J. Schaffner-Bielich, *A search for inverse magnetic catalysis in thermal quark-meson models*, Phys.Lett. **B731** (2014) 154–158, `arXiv:1311.3964 [hep-ph]`.

[117] M. Ruggieri, L. Oliva, P. Castorina, R. Gatto, and V. Greco, *Critical Endpoint and Inverse Magnetic Catalysis for Finite Temperature and Density Quark Matter in a Magnetic Background*, Phys.Lett. **B734** (2014) 255–260, `arXiv:1402.0737 [hep-ph]`.

[118] I. Shushpanov and A. V. Smilga, *Quark condensate in a magnetic field*, Phys.Lett. **B402** (1997) 351–358, `arXiv:hep-ph/9703201 [hep-ph]`.

[119] T. D. Cohen, D. A. McGady, and E. S. Werbos, *The Chiral condensate in a constant electromagnetic field*, Phys.Rev. **C76** (2007) 055201, `arXiv:0706.3208 [hep-ph]`.

[120] N. O. Agasian, *Phase structure of the QCD vacuum in a magnetic field at low temperature*, Phys.Lett. **B488** (2000) 39–45, `arXiv:hep-ph/0005300 [hep-ph]`.

[121] J. O. Andersen, *Thermal pions in a magnetic background*, Phys.Rev. **D86** (2012) 025020, `arXiv:1202.2051 [hep-ph]`.

[122] J. O. Andersen, *Chiral perturbation theory in a magnetic background - finite-temperature effects*, JHEP **1210** (2012) 005, `arXiv:1205.6978 [hep-ph]`.

[123] J. O. Andersen and A. Tranberg, *The Chiral transition in a magnetic background: Finite density effects and the functional renormalization group*, JHEP **1208** (2012) 002, `arXiv:1204.3360 [hep-ph]`.

[124] K. Kamikado and T. Kanazawa, *Chiral dynamics in a magnetic field from the functional renormalization group*, JHEP **1403** (2014) 009, `arXiv:1312.3124 [hep-ph]`.

[125] O. Bergman, G. Lifschytz, and M. Lippert, *Response of Holographic QCD to Electric and Magnetic Fields*, JHEP **0805** (2008) 007, `arXiv:0802.3720 [hep-th]`.

[126] C. V. Johnson and A. Kundu, *External Fields and Chiral Symmetry Breaking in the Sakai-Sugimoto Model*, JHEP **0812** (2008) 053, `arXiv:0803.0038 [hep-th]`.

[127] A. Rebhan, A. Schmitt, and S. A. Stricker, *Meson supercurrents and the Meissner effect in the Sakai-Sugimoto model*, JHEP **0905** (2009) 084, `arXiv:0811.3533 [hep-th]`.

[128] C. V. Johnson and A. Kundu, *Meson Spectra and Magnetic Fields in the Sakai-Sugimoto Model*, JHEP **0907** (2009) 103, `arXiv:0904.4320 [hep-th]`.

[129] F. Preis, A. Rebhan, and A. Schmitt, *Inverse magnetic catalysis in dense holographic matter*, JHEP **1103** (2011) 033, `arXiv:1012.4785 [hep-th]`.

[130] N. Callebaut, D. Dudal, and H. Verschelde, *Holographic rho mesons in an external magnetic field*, JHEP **1303** (2013) 033, `arXiv:1105.2217 [hep-th]`.

[131] A. Ballon-Bayona, K. Peeters, and M. Zamaklar, *A chiral magnetic spiral in the holographic Sakai-Sugimoto model*, JHEP **1211** (2012) 164, `arXiv:1209.1953 [hep-th]`.

[132] A. Ballon-Bayona, *Holographic deconfinement transition in the presence of a magnetic field*, JHEP **1311** (2013) 168, `arXiv:1307.6498 [hep-th]`.

[133] N. Callebaut and D. Dudal, *A magnetic instability of the non-Abelian Sakai-Sugimoto model*, JHEP **1401** (2014) 055, `arXiv:1309.5042 [hep-th]`.

[134] V. A. Miransky and I. A. Shovkovy, *Quantum field theory in a magnetic field: From quantum chromodynamics to graphene and Dirac semimetals*, Phys.Rept. **576** (2015) 1–209, `arXiv:1503.00732 [hep-ph]`.

[135] S. Klevansky and R. H. Lemmer, *Chiral symmetry restoration in the Nambu-Jona-Lasinio model with a constant electromagnetic field*, Phys.Rev. **D39** (1989) 3478–3489.

[136] H. Suganuma and T. Tatsumi, *On the Behavior of Symmetry and Phase Transitions in a Strong Electromagnetic Field*, Annals Phys. **208** (1991) 470–508.

[137] V. Gusynin, V. Miransky, and I. Shovkovy, *Catalysis of dynamical flavor symmetry breaking by a magnetic field in (2+1)-dimensions*, Phys.Rev.Lett. **73** (1994) 3499–3502, `arXiv:hep-ph/9405262 [hep-ph]`.

[138] V. Gusynin, V. Miransky, and I. Shovkovy, *Dimensional reduction and dynamical chiral symmetry breaking by a magnetic field in (3+1)-dimensions*, Phys.Lett. **B349** (1995) 477–483, `arXiv:hep-ph/9412257 [hep-ph]`.

[139] V. Gusynin, V. Miransky, and I. Shovkovy, *Dynamical flavor symmetry breaking by a magnetic field in (2+1)-dimensions*, Phys.Rev. **D52** (1995) 4718–4735, `arXiv:hep-th/9407168 [hep-th]`.

[140] L. Levkova and C. DeTar, *Quark-gluon plasma in an external magnetic field*, Phys.Rev.Lett. **112** no. 1, (2014) 012002, `arXiv:1309.1142 [hep-lat]`.

[141] C. Bonati, M. D'Elia, M. Mariti, F. Negro, and F. Sanfilippo, *Magnetic Susceptibility of Strongly Interacting Matter across the Deconfinement Transition*, Phys.Rev.Lett. **111** (2013) 182001, `arXiv:1307.8063 [hep-lat]`.

[142] E.-M. Ilgenfritz, M. Kalinowski, M. Muller-Preussker, B. Petersson, and A. Schreiber, *Two-color QCD with staggered fermions at finite temperature under the influence of a magnetic field*, Phys.Rev. **D85** (2012) 114504, `arXiv:1203.3360 [hep-lat]`.

[143] M. D'Elia and F. Negro, *Chiral Properties of Strong Interactions in a Magnetic Background*, Phys.Rev. **D83** (2011) 114028, `arXiv:1103.2080 [hep-lat]`.

[144] C. Bonati, M. D'Elia, M. Mariti, F. Negro, and F. Sanfilippo, *Magnetic susceptibility and equation of state of* $N_f = 2 + 1$ *QCD with physical quark masses*, Phys.Rev. **D89** no. 5, (2014) 054506, `arXiv:1310.8656 [hep-lat]`.

[145] C. Bonati, M. D'Elia, M. Mariti, M. Mesiti, F. Negro, et al., *Anisotropy of the quark-antiquark potential in a magnetic field*, Phys.Rev. **D89** no. 11, (2014) 114502, `arXiv:1403.6094 [hep-lat]`.

[146] G. Bali, F. Bruckmann, G. Endrodi, F. Gruber, and A. Schaefer, *Magnetic field-induced gluonic (inverse) catalysis and pressure (an)isotropy in QCD*, JHEP **1304** (2013) 130, `arXiv:1303.1328 [hep-lat]`.

[147] N. Mueller, J. A. Bonnet, and C. S. Fischer, *Dynamical quark mass generation in a strong external magnetic field*, Phys.Rev. **D89** no. 9, (2014) 094023, `arXiv:1401.1647 [hep-ph]`.

[148] G. Endrodi, *Critical Endpoint in the QCD Phase Diagram for Extremely Strong Background Magnetic Fields*, `arXiv:1504.08280 [hep-lat]`.

[149] T. Banks and A. Casher, *Chiral Symmetry Breaking in Confining Theories*, Nucl.Phys. **B169** (1980) 103.

[150] T. Kojo and N. Su, *The quark mass gap in a magnetic field*, Phys.Lett. **B720** (2013) 192–197, `arXiv:1211.7318 [hep-ph]`.

[151] T. Kojo and N. Su, *The quark mass gap in strong magnetic fields*, Nucl.Phys. **A931** (2014) 763–768, `arXiv:1407.7925 [hep-ph]`.

[152] K. Fukushima and Y. Hidaka, *Magnetic Catalysis Versus Magnetic Inhibition*, Phys.Rev.Lett. **110** no. 3, (2013) 031601, `arXiv:1209.1319 [hep-ph]`.

[153] L. Yu, J. Van Doorsselaere, and M. Huang, *Inverse Magnetic Catalysis in the three-flavor NJL model with axial-vector interaction*, Phys.Rev. **D91** no. 7, (2015) 074011, `arXiv:1411.7552 [hep-ph]`.

[154] K. A. Mamo, *Inverse magnetic catalysis in holographic models of QCD*, JHEP **1505** (2015) 121, `arXiv:1501.03262 [hep-th]`.

[155] N. Mueller and J. M. Pawlowski, *Magnetic catalysis and inverse magnetic catalysis in QCD*, `arXiv:1502.08011 [hep-ph]`.

[156] A. Ayala, J. Cobos-Martínez, M. Loewe, M. E. Tejeda-Yeomans, and R. Zamora, *Finite temperature quark-gluon vertex with a magnetic field in the Hard Thermal Loop approximation*, Phys.Rev. **D91** no. 1, (2015) 016007, `arXiv:1410.6388 [hep-ph]`.

[157] A. Ayala, M. Loewe, and R. Zamora, *Inverse magnetic catalysis in the linear sigma model with quarks*, Phys.Rev. **D91** no. 1, (2015) 016002, `arXiv:1406.7408 [hep-ph]`.

[158] A. Ayala, M. Loewe, A. J. Mizher, and R. Zamora, *Inverse magnetic catalysis for the chiral transition induced by thermo-magnetic effects on the coupling constant*, Phys.Rev. **D90** no. 3, (2014) 036001, `arXiv:1406.3885 [hep-ph]`.

[159] P. Costa, M. Ferreira, D. P. Menezes, J. Moreira, and C. Providência, *Influence of the inverse magnetic catalysis and the vector interaction in the location of the critical end point*, Phys. Rev. **D92** no. 3, (2015) 036012, `arXiv:1508.07870 [hep-ph]`.

[160] Particle Data Group Collaboration, K. Olive et al., *Review of Particle Physics*, Chin.Phys. **C38** (2014) 090001.

[161] K. Fujikawa, *Comment on Chiral and Conformal Anomalies*, Phys.Rev.Lett. **44** (1980) 1733.

[162] A. Bernstein and B. R. Holstein, *Neutral Pion Lifetime Measurements and the QCD Chiral Anomaly*, Rev.Mod.Phys. **85** (2013) 49, `arXiv:1112.4809 [hep-ph]`.

[163] J. Greensite, *An introduction to the confinement problem*, Lect.Notes Phys. **821** (2011) 1–211.

[164] H. Rothe, *Lattice gauge theories: An Introduction*, World Sci.Lect.Notes Phys. **43** (1992) 1–381.

[165] Y. Nambu and G. Jona-Lasinio, *Dynamical Model of Elementary Particles Based on an Analogy with Superconductivity. 1.*, Phys.Rev. **122** (1961) 345–358.

[166] Y. Nambu and G. Jona-Lasinio, *Dynamical Model of Elementary Particles Based on an Analogy with Superconductivity. II*, Phys.Rev. **124** (1961) 246–254.

[167] U. Vogl and W. Weise, *The Nambu and Jona Lasinio model: Its implications for hadrons and nuclei*, Prog.Part.Nucl.Phys. **27** (1991) 195–272.

[168] S. Klevansky, *The Nambu-Jona-Lasinio model of quantum chromodynamics*, Rev.Mod.Phys. **64** (1992) 649–708.

[169] T. Hatsuda and T. Kunihiro, *QCD phenomenology based on a chiral effective Lagrangian*, Phys.Rept. **247** (1994) 221–367, `arXiv:hep-ph/9401310 [hep-ph]`.

[170] M. Buballa, *NJL model analysis of quark matter at large density*, Phys.Rept. **407** (2005) 205–376, `arXiv:hep-ph/0402234 [hep-ph]`.

[171] G. 't Hooft, *Symmetry Breaking Through Bell-Jackiw Anomalies*, Phys.Rev.Lett. **37** (1976) 8–11.

[172] G. 't Hooft, *Computation of the Quantum Effects Due to a Four-Dimensional Pseudoparticle*, Phys.Rev. **D14** (1976) 3432–3450.

[173] J. Kapusta and C. Gale, *Finite-Temperature Field Theory: Principles and Applications*. Cambridge Monographs on Mathematical Physics. Cambridge University Press, 2006.

[174] A. Das, *Finite Temperature Field Theory*. World scientific lecture notes in physics. World Scientific, 1997.

[175] M. Bellac, *Thermal Field Theory*. Cambridge Monographs on Mathematical Physics. Cambridge University Press, 2000.

[176] G. Ripka, *Quarks Bound by Chiral Fields: The Quark Structure of the Vacuum and of Light Mesons and Baryons*. Oxford science publications. Clarendon Press, 1997.

[177] M. F. Lutz, S. Klimt, and W. Weise, *Meson properties at finite temperature and baryon density*, Nucl.Phys. **A542** (1992) 521–558.

[178] P. Rehberg, S. Klevansky, and J. Hufner, *Hadronization in the SU(3) Nambu-Jona-Lasinio model*, Phys.Rev. **C53** (1996) 410–429, `arXiv:hep-ph/9506436 [hep-ph]`.

[179] P. N. Meisinger and M. C. Ogilvie, *Chiral symmetry restoration and Z(N) symmetry*, Phys.Lett. **B379** (1996) 163–168, `arXiv:hep-lat/9512011 [hep-lat]`.

[180] R. D. Pisarski, *Quark gluon plasma as a condensate of SU(3) Wilson lines*, Phys.Rev. **D62** (2000) 111501, `arXiv:hep-ph/0006205 [hep-ph]`.

[181] P. N. Meisinger, T. R. Miller, and M. C. Ogilvie, *Phenomenological equations of state for the quark gluon plasma*, Phys.Rev. **D65** (2002) 034009, `arXiv:hep-ph/0108009 [hep-ph]`.

[182] K. Fukushima, *Chiral effective model with the Polyakov loop*, Phys.Lett. **B591** (2004) 277–284, `arXiv:hep-ph/0310121 [hep-ph]`.

[183] A. Mocsy, F. Sannino, and K. Tuominen, *Confinement versus chiral symmetry*, Phys.Rev.Lett. **92** (2004) 182302, `arXiv:hep-ph/0308135 [hep-ph]`.

[184] C. Ratti, M. A. Thaler, and W. Weise, *Phases of QCD: Lattice thermodynamics and a field theoretical model*, Phys.Rev. **D73** (2006) 014019, `arXiv:hep-ph/0506234 [hep-ph]`.

[185] H. Hansen, W. Alberico, A. Beraudo, A. Molinari, M. Nardi, et al., *Mesonic correlation functions at finite temperature and density in the Nambu-Jona-Lasinio model with a Polyakov loop*, Phys.Rev. **D75** (2007) 065004, `arXiv:hep-ph/0609116 [hep-ph]`.

[186] C. Ratti, M. A. Thaler, and W. Weise, *Phase diagram and thermodynamics of the PNJL model*, `arXiv:nucl-th/0604025 [nucl-th]`.

[187] S. Roessner, C. Ratti, and W. Weise, *Polyakov loop, diquarks and the two-flavour phase diagram*, Phys.Rev. **D75** (2007) 034007, `arXiv:hep-ph/0609281 [hep-ph]`.

[188] K. Fukushima, *Phase diagrams in the three-flavor Nambu-Jona-Lasinio model with the Polyakov loop*, Phys.Rev. **D77** (2008) 114028, `arXiv:0803.3318 [hep-ph]`.

[189] L. M. Haas, R. Stiele, J. Braun, J. M. Pawlowski, and J. Schaffner-Bielich, *Improved Polyakov-loop potential for effective models from functional calculations*, Phys.Rev. **D87** no. 7, (2013) 076004, `arXiv:1302.1993 [hep-ph]`.

[190] C. Ratti, S. Roessner, M. A. Thaler, and W. Weise, *Thermodynamics of the PNJL model*, Eur. Phys. J. **C49** (2007) 213–217, `arXiv:hep-ph/0609218 [hep-ph]`.

[191] P. Costa, M. Ruivo, C. de Sousa, and H. Hansen, *Phase diagram and critical properties within an effective model of QCD: the Nambu-Jona-Lasinio model coupled to the Polyakov loop*, Symmetry **2** (2010) 1338–1374, `arXiv:1007.1380 [hep-ph]`.

[192] I. A. Shovkovy, *Magnetic Catalysis: A Review*, Lect.Notes Phys. **871** (2013) 13–49, `arXiv:1207.5081 [hep-ph]`.

[193] J. O. Andersen, W. R. Naylor, and A. Tranberg, *Phase diagram of QCD in a magnetic field: A review*, `arXiv:1411.7176 [hep-ph]`.

[194] A. Roberge and N. Weiss, *Gauge Theories With Imaginary Chemical Potential and the Phases of QCD*, Nucl.Phys. **B275** (1986) 734.

[195] M. D'Elia and F. Sanfilippo, *The Order of the Roberge-Weiss endpoint (finite size transition) in QCD*, Phys.Rev. **D80** (2009) 111501, `arXiv:0909.0254 [hep-lat]`.

[196] P. de Forcrand and O. Philipsen, *Constraining the QCD phase diagram by tricritical lines at imaginary chemical potential*, Phys.Rev.Lett. **105** (2010) 152001, `arXiv:1004.3144 [hep-lat]`.

[197] Y. Sakai, T. Sasaki, H. Kouno, and M. Yahiro, *Entanglement between deconfinement transition and chiral symmetry restoration*, Phys.Rev. **D82** (2010) 076003, `arXiv:1006.3648 [hep-ph]`.

[198] Y. Sakai, T. Sasaki, H. Kouno, and M. Yahiro, *Equation of state in the PNJL model with the entanglement interaction*, J.Phys. **G39** (2012) 035004, `arXiv:1104.2394 [hep-ph]`.

[199] T. Sasaki, Y. Sakai, H. Kouno, and M. Yahiro, *Quark-mass dependence of the three-flavor QCD phase diagram at zero and imaginary chemical potential: Model prediction*, Phys.Rev. **D84** (2011) 091901, `arXiv:1105.3959 [hep-ph]`.

[200] Y. Aoki, G. Endrodi, Z. Fodor, S. Katz, and K. Szabo, *The Order of the quantum chromodynamics transition predicted by the standard model of particle physics*, Nature **443** (2006) 675–678, `arXiv:hep-lat/0611014 [hep-lat]`.

[201] P. Costa, C. de Sousa, M. Ruivo, and Y. Kalinovsky, *The QCD critical end point in the SU(3) Nambu-Jona-Lasinio model*, Phys.Lett. **B647** (2007) 431–435, `arXiv:hep-ph/0701135 [hep-ph]`.

[202] P. Costa, C. de Sousa, M. Ruivo, and H. Hansen, *The QCD critical end point in the PNJL model*, Europhys.Lett. **86** (2009) 31001, `arXiv:0801.3616 [hep-ph]`.

[203] P. Costa, M. Ruivo, and C. de Sousa, *Thermodynamics and critical behavior in the Nambu-Jona-Lasinio model of QCD*, Phys.Rev. **D77** (2008) 096001, `arXiv:0801.3417 [hep-ph]`.

[204] S.-i. Nam and C.-W. Kao, *Chiral restoration at finite T under the magnetic field with the meson-loop corrections*, Phys.Rev. **D83** (2011) 096009, `arXiv:1103.6057 [hep-ph]`.

[205] N. Callebaut and D. Dudal, *Transition temperature(s) of magnetized two-flavor holographic QCD*, Phys.Rev. **D87** no. 10, (2013) 106002, `arXiv:1303.5674 [hep-th]`.

[206] A. A. Osipov, B. Hiller, and J. da Providencia, *Multi-quark interactions with a globally stable vacuum*, Phys.Lett. **B634** (2006) 48–54, `arXiv:hep-ph/0508058 [hep-ph]`.

[207] A. Osipov, B. Hiller, J. Moreira, A. Blin, and J. da Providencia, *Lowering the critical temperature with eight-quark interactions*, Phys.Lett. **B646** (2007) 91–94, `arXiv:hep-ph/0612082 [hep-ph]`.

[208] B. Hiller, J. Moreira, A. Osipov, and A. Blin, *The Phase diagram for the Nambu-Jona-Lasinio model with 't Hooft and eight-quark interactions*, Phys.Rev. **D81** (2010) 116005, `arXiv:0812.1532 [hep-ph]`.

[209] A. Bazavov, T. Bhattacharya, M. Cheng, C. DeTar, H. Ding, et al., *The chiral and deconfinement aspects of the QCD transition*, Phys.Rev. **D85** (2012) 054503, `arXiv:1111.1710 [hep-lat]`.

[210] B.-J. Schaefer, J. M. Pawlowski, and J. Wambach, *The Phase Structure of the Polyakov–Quark-Meson Model*, Phys.Rev. **D76** (2007) 074023, `arXiv:0704.3234 [hep-ph]`.

[211] B.-J. Schaefer, M. Wagner, and J. Wambach, *Thermodynamics of (2+1)-flavor QCD: Confronting Models with Lattice Studies*, Phys.Rev. **D81** (2010) 074013, `arXiv:0910.5628 [hep-ph]`.

[212] T. K. Herbst, J. M. Pawlowski, and B.-J. Schaefer, *The phase structure of the Polyakov–quark-meson model beyond mean field*, Phys.Lett. **B696** (2011) 58–67, `arXiv:1008.0081 [hep-ph]`.

[213] T. D. Cohen and N. Yamamoto, *New critical point for QCD in a magnetic field*, Phys.Rev. **D89** no. 5, (2014) 054029, `arXiv:1310.2234 [hep-ph]`.

[214] V. Miransky and I. Shovkovy, *Magnetic catalysis and anisotropic confinement in QCD*, Phys.Rev. **D66** (2002) 045006, `arXiv:hep-ph/0205348 [hep-ph]`.

[215] B. Friman, C. Hohne, J. Knoll, S. Leupold, J. Randrup, et al., *The CBM physics book: Compressed baryonic matter in laboratory experiments*, Lect.Notes Phys. **814** (2011) pp. 980.

[216] P. Costa, M. Ruivo, C. de Sousa, and Y. Kalinovsky, *Analysis of the U(A)(1) symmetry-breaking and restoration effects on scalar-pseudoscalar spectrum*, Phys.Rev. **D71** (2005) 116002, `arXiv:hep-ph/0503258 [hep-ph]`.

[217] V. Voronyuk, V. Toneev, W. Cassing, E. Bratkovskaya, V. Konchakovski, et al., *(Electro-)Magnetic field evolution in relativistic heavy-ion collisions*, Phys.Rev. **C83** (2011) 054911, `arXiv:1103.4239 [nucl-th]`.

[218] D. E. Kharzeev, L. D. McLerran, and H. J. Warringa, *The Effects of topological charge change in heavy ion collisions: 'Event by event P and CP violation'*, Nucl.Phys. **A803** (2008) 227–253, `arXiv:0711.0950 [hep-ph]`.

[219] A. Ohnishi, H. Ueda, T. Nakano, M. Ruggieri, and K. Sumiyoshi, *Possibility of QCD critical point sweep during black hole formation*, Phys.Lett. **B704** (2011) 284–290, `arXiv:1102.3753 [nucl-th]`.

[220] H. Abuki, *Fate of chiral critical point under the strong isospin asymmetry*, Phys.Rev. **D87** no. 9, (2013) 094006, `arXiv:1304.1904 [hep-ph]`.

[221] J. O. Andersen and L. Kyllingstad, *Pion Condensation in a two-flavor NJL model: the role of charge neutrality*, J.Phys. **G37** (2009) 015003, `arXiv:hep-ph/0701033 [hep-ph]`.

[222] T. Sasaki, Y. Sakai, H. Kouno, and M. Yahiro, *QCD phase diagram at finite baryon and isospin chemical potentials*, Phys.Rev. **D82** (2010) 116004, `arXiv:1005.0910 [hep-ph]`.

[223] C. Ratti, R. Bellwied, M. Cristoforetti, and M. Barbaro, *Are there hadronic bound states above the QCD transition temperature?*, Phys. Rev. **D85** (2012) 014004, `arXiv:1109.6243 [hep-ph]`.

[224] P. Costa, M. Ruivo, C. de Sousa, H. Hansen, and W. Alberico, *Scalar-pseudoscalar meson behavior and restoration of symmetries in SU(3) PNJL model*, Phys.Rev. **D79** (2009) 116003, `arXiv:0807.2134 [hep-ph]`.